Advances in Soft Strain and Pressure Sensors

Duy Van Nguyen[1], Pingan Song[2], Farid Manshaii[3], John Bell[2], Jun Chen[3]*, Toan Dinh[1]**

[1]School of Engineering and Centre for Future Materials, University of Southern Queensland, Ipswich, Queensland 4300, Australia

[2]Centre for Future Materials, University of Southern Queensland, Ipswich, Queensland 4300, Australia

[3]Department of Bioengineering, University of California, Los Angeles, Los Angeles, CA 90095, USA

*Correspondence to: duyvan.nguyen@unisq.edu.au (D.V.N); jun.chen@ucla.edu (J.C.); toan.dinh@unisq.edu.au (T.D.)

Abstract:

Soft strain and pressure sensors represent a breakthrough in material engineering and nanotechnology, providing accurate and reliable signal detection for applications in health monitoring, sports management, human-machine interface, or soft robotics, when compared to traditional rigid sensors. However, their performance is often compromised by environmental interference and off-axis mechanical deformations, which lead to non-specific responses, as well as unstable and inaccurate measurements. These challenges can be effectively addressed by enhancing the sensors' specificity, making them responsive only to the desired stimulus while

remaining insensitive to unwanted stimuli. This review systematically examines various materials and design strategies for developing strain and pressure sensors with high specificity for target physical signals, such as tactility, pressure distribution, body motions, or artery pulse. This review highlights approaches in materials engineering that impart special properties to the sensors to suppress interference from factors such as temperature, humidity, and liquid contact. Additionally, it details structural designs that improve sensor performance under different types of off-axis mechanical deformations. This review concludes by discussing the ongoing challenges and opportunities for inspiring the future development of highly specific electromechanical sensors.

Keywords: specificity, temperature independent, liquid repellent, off-axis deformation insensitivity, nanomaterials, microstructure, strain sensors, pressure sensors, biophysical signals,

The recent development of soft wearable sensors marks a significant advancement in healthcare monitoring technologies, sports management, human-machine interaction (HMI), or soft robotics.[1-4] Through sensing skin deformations, these sensors can monitor critical human biophysical signals, such as pulse rate, respiratory rate, and body movements, which are vital for health management and sports training. Detection of external stress, joint motions, or stretching actuators allows for improved human interaction recognition and enhanced control over soft robot motions, which is beneficial for developing smart devices or machines that serve human interests. Moreover, soft or flexible sensors feature overall low Young's modulus (less than 10^8) or minimal thickness.[5-7] The softness enables the sensors to resist mechanical deformation (typically, greater than 10 m^{-1} bending curvature or greater than 1% strain on a device/system)

and conformally contact with targeted curvilinear surfaces (e.g., human skin or soft actuators), enhancing wearing comfort and signal quality.[1, 6] As a result, interested physical signals can be continuously recorded by soft patches that incorporate various sensing units, including flexible or stretchable strain and pressure sensors, commonly known as electromechanical sensors.[4, 8-11] Depending on application requirements, strain sensors can be stretched to greater than 70% for human skin or even 200% for robotics.[6, 7] Flexible pressure sensors can detect pressure ranging from low pressure (e.g., breathing or pulse pressure) to high pressure (e.g., tactile or foot pressure).[12] Innovations in material design and fabrication techniques have led to substantial progress in the development of soft strain and pressure sensors with high sensitivity and a wide working range.[13-18] Long-standing issues, such as the trade-off between sensitivity, sensing range, and non-linearity of mechanical sensors, have also been addressed through advanced materials engineering and design approaches.[19-24] However, soft strain and pressure sensors still face significant challenges related to stability and accuracy due to external factors such as temperature, humidity, and off-axis deformation, [11, 25-33] which negatively impact detection quality of interested physical signals.

Environmental factors can cause interference to detected physical signals. Soft strain and pressure sensors are typically made of active conductive materials and soft substrates.[17, 18] The materials' properties can be altered with changes in the working environment, such as temperature changes and exposure to liquids, humidity. Temperature variations have huge impact on materials' conductivity or electron retention, while exposure to different liquids or humidity can degrade the conductive materials, interfere with conductive paths, or affect structural integrity of flexible substrates.[25-29] As a consequence, for example, when these sensors are applied on human skin to monitor biophysical signals in various settings like hot or cold

weather, outdoor-indoor humidity differences, or underwater, the environmental interferences can impact sensor materials' properties, inducing fluctuations in sensor outputs. The fluctuation leads to faulty predictions and misleading information of detected physical signals - especially critical in medical applications where sensor data monitors vital organ functions.[34, 35] In harsh environments, such as those with extreme temperatures, high humidity, or corrosive substances, sensors not only exhibit unstable operation but can also suffer physical or chemical damage.[29, 36-38] This degradation can prevent sensors from maintaining the required signal accuracy, potentially causing system failures.

Off-axis deformations inflict distortion on sensed physical signals. Human skin or soft robotic actuators can experience deformations or external forces in various directions during normal operation.[39-42] Thus, when soft sensors are conformally attached onto human skin or soft actuators to detect required physical signals, they undergo stresses or strains in multiple orientations. For example, when strain sensors are attached on wrist area of a golfer to monitor the wrist movement during shooting golf balls,[43] the sensors experience complex deformation as the wrist is a multiple axis joint. As a result, a strain sensor designated to sense strain in one direction can experience undesirable strains in other directions. In soft robotics, a pressure sensor designed to sense out-of-plane compression is attached on a pneumatic actuator.[39] When activating the actuator, its inflated surface can cause interfering in-plane strains to the pressure sensor. Desired stress direction for pressure sensing is normal to surface, and preferred strain direction for strain sensors is, usually, in-plane, parallel to the sensors' length. Unwanted deformations from stress or strains in off-axis directions, on the other hand, can compromise electrical properties of active materials or adding more changes to the output signals. The consequence is physical signal errors such as noise, drift, or loss of critical information.[8, 32, 33]

The inaccurate detection of physical signals is not favorable for practical applications, such as accurate monitoring of joint motions for sports managements or precise robot controlling. Moreover, maintaining desired performance levels from the inaccurate signals is challenging when it can complicate data processing, increase the overall system burden, and elevate costs.

To address these issues and improve accuracy and stability, developing specificity in soft strain and pressure sensors has emerged as an effective solution. Specificity enables sensors to respond only to the intended stimulus, ensuring accurate measurements. For example, a strain sensor with high specificity is sensitive only to strain and remains insensitive to pressure, bending, and torsion, thereby significantly reducing undesirable errors such as noise.[33] This insensitivity to off-axis mechanical deformation can be achieved through various structural designs.[33, 39, 44] Moreover, specificity can enhance sensor stability, traditionally evaluated through cycling tests that span tens of thousands [10, 45] or even millions of sensing cycles.[46] Sensors with specificity can accurately detect the target signal without interference from environmental factors such as temperature, humidity, and liquid contact [47, 48], thus improving long-term stability. Achieving stability through specificity can involve materials engineering methods such as material combination, chemical treatments, or surface morphology modifications to minimize adverse environmental effects.[49-51]

In this review, we explore the current understanding of the specificity of soft electromechanical sensors, focusing on two widely investigated types, strain sensors and pressure sensors. Therefore, in this context, electromechanical sensors refer to either strain sensors or pressure sensors. This work focuses on strategies to suppress unwanted stimuli from two major sources: ambient environmental factors and mechanical deformations. We analyze materials engineering and structural design approaches that enable sensors to resist undesirable interference (**Figure 1**).

First, we summarize strategies for manipulating materials to achieve resistance to environmental conditions, further divided into insensitivity to temperature and humidity or liquid contact. Next, we review both materials engineering and structural design strategies applied to minimize off-axis deformations, broken down into applications for pressure sensors and strain sensors, considering the specific requirements of each type. Moreover, in each subsection on insensitivity, we highlight the effectiveness of integrating the corresponding insensitivity type into soft electromechanical sensors for relevant real-life applications. Finally, we summarize the presented information, highlight necessary improvements, and suggest directions for future research.

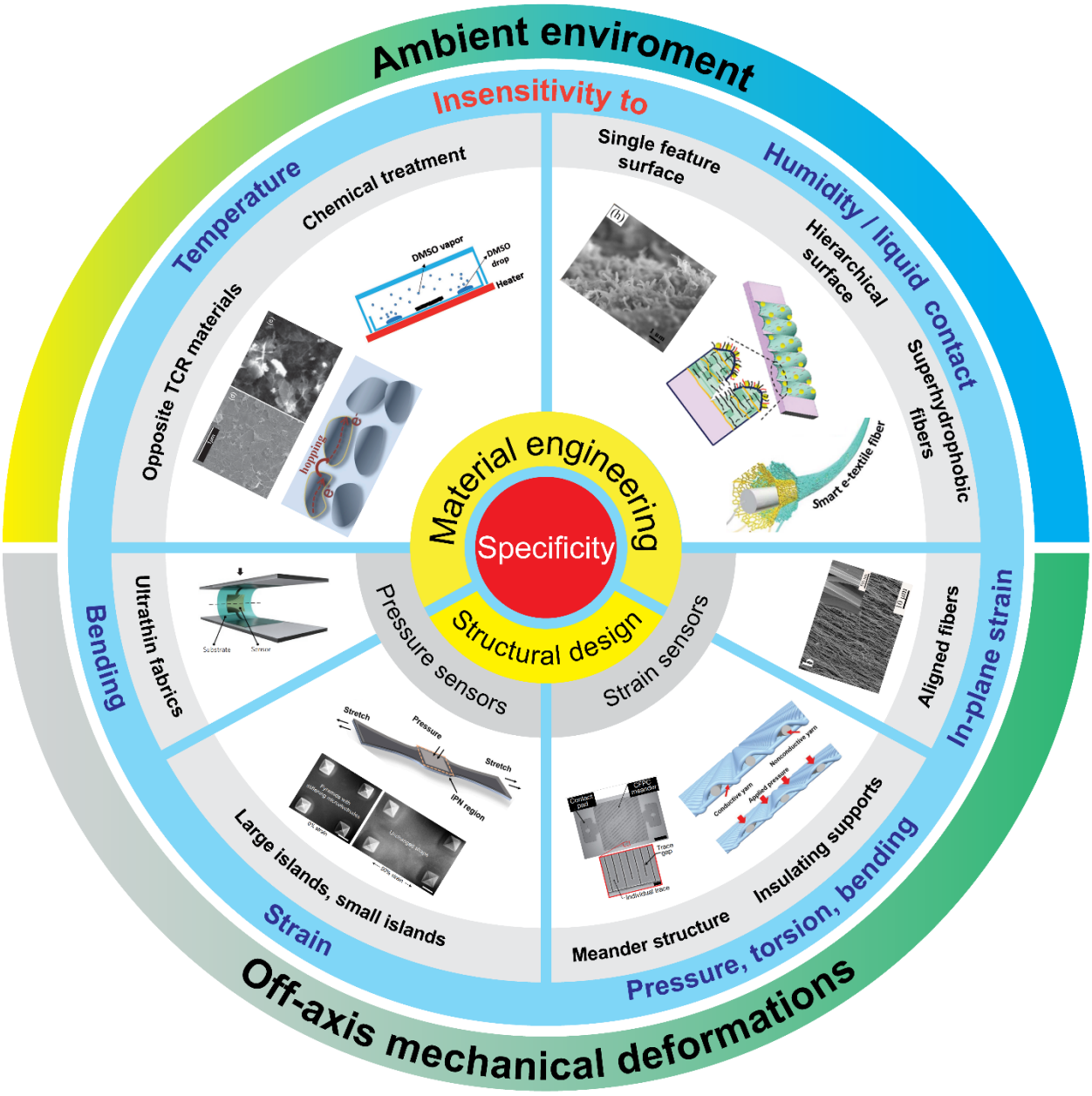

Figure 1. Summary of approaches to integrate different types of insensitivity into electromechanical sensors for achieving specificity through either materials engineering or structural designs. Temperature insensitivity is achieved using materials with opposite TCRs or by modifying electrical properties. Reprinted with permission from ref [52]. Copyright 2013 John Wiley and Sons. Reprinted with permission from ref [53]. Copyright 2023 Elsevier. Reprinted with permission from ref [54]. Copyright 2017 John Wiley and Sons. Humidity or liquid contact insensitivity can be introduced using a single-feature surface, a hierarchical surface, or superhydrophobic fibers. Reprinted with permission from ref [48]. Copyright 2021 Elsevier. Reprinted with permission from ref [55]. Copyright

2020 John Wiley and Sons. Reprinted with permission from ref [56]. Copyright 2019 Elsevier. Pressure sensors gain insensitivity to bending and strain through methods such as ultrathin fabrics, large islands, or small islands. Reprinted with permission from ref [57]. Copyright 2016 Springer Nature. Reprinted with permission from ref [58]. Copyright 2023 Elsevier. Reprinted with permission from ref [39]. Copyright 2021 John Wiley and Sons. Strain sensors exhibit insensitivity to pressure, torsion, bending, and in-plane strain via techniques like the meander structure, insulating supports, or aligned fibers. Reprinted with permission from ref [44]. Copyright 2020 Springer Nature. Reprinted with permission under a Creative Commons CC BY 4.0 License from ref [59]. Copyright 2021 John Wiley and Sons. Reprinted with permission from ref [42]. Copyright 2022 Elsevier.

Materials Engineering for Insensitivity to Unwanted Interference from Ambient Environment

Materials are the fundamental building blocks of soft electromechanical sensors. Two types of materials forming the sensors include active conductive materials, such as metallic nanomaterials, carbon nanomaterials, and flexible or stretchable insulating substrates made from porous or non-porous materials. In various wearable application settings (i.e., cold, hot, wet, dry, or corrosive), temperature changes can directly impact the electrical properties of the active conductive components or expanding the insulating substrates,[60] while humidity or liquid contact can interfere with conductive paths or destabilize the insulating matrix (i.e., swelling).[61-64] The consequence is unstable sensing performance and unreliable physical signal information. Therefore, the general choice of conductive material networks as sensing elements and flexible or stretchable insulating materials as substrates is not enough for stable sensing performance. This leads to demand for investigation on innovative methods to engineer materials for both active and substrate materials. So that the sensors based on those engineered materials can feature insensitive properties, typically insensitivity to temperature changes and to exposure humidity or liquids, which is required for long-term and accurate signal detection. The

subsections below summarize such methods to achieve insensitivity to temperature and humidity or liquid contact, which is beneficial for immediate adoption or for forming foundation for further investigation.

Materials Engineering for Electromechanical Sensors Insensitive to Temperature

When applied on human skin or soft actuators, pressure and strain sensors can operate under diverse temperature conditions, including low-temperature conditions (e.g., in cryogenic boxes, cold weather), high-temperature environments (e.g., firefighting), or temperature variation during typical day-night cycles.[38, 65-67] When the soft sensors are applied for human wearable sensing, they also suffer from temperatures variations due to heat released from human skin.[47] Under such changing temperature conditions, the properties of sensor materials, typically electrical characteristics and geometry, can change, negatively affecting sensing performance. Developing materials that are minimally affected by temperature is crucial for maintaining sensor stability. This section explores various approaches, like materials combination or chemical treatment, to develop temperature-independent flexible electromechanical sensors based on piezoresistive, capacitive, and triboelectric effects.

Temperature-Insensitive Electromechanical Sensors Based on the Piezoresistive Principle

Sensors operating on the piezoresistive effect (where electrical resistance changes due to mechanical deformations) are particularly susceptible to temperature variations. Temperature changes can alter the conductivity of active components (conductive materials) by expanding both conductive and matrix materials (as defined by the coefficient of thermal expansion [CTE]) or by modifying the conductive properties of the materials (defined by the temperature coefficient of resistance [TCR]). Thermal expansion of the matrix can widen gaps between

conductive fillers, reducing tunneling or hopping of charge carriers and increasing resistance.[25] Common active materials include metals (e.g., gold [68], silver [69]), carbon materials (e.g., graphene [G][65, 70], graphene oxide [GO] [47], carbon nanotubes [CNTs] [71, 72]), and conductive polymers (e.g., poly(3,4-ethylenedioxythiophene) polystyrene sulfonate [PEDOT:PSS] [73, 74], polypyrrole [75]). Metals typically exhibit a positive TCR (p-TCR) due to increased inelastic electron scattering and lattice spacing with temperature.[76-78] Metallic CNTs also show p-TCR, while semiconducting CNTs (individual or network) generally exhibit negative TCR (n-TCR) because of their intrinsic semiconductor properties and thermally-assisted tunneling transport.[79, 80] Graphene or reduced graphene oxide (rGO) behaves as a zero-gap semiconductor with a small n-TCR at room temperature because resistivity primarily depends on charge-carrier concentration, which increases with temperature.[66, 78, 81] Untreated PEDOSS:PSS shows semiconducting behavior with temperature-activated hopping transport and an n-TCR.[82, 83] Several engineering approaches have been proposed to achieve small or near-zero TCR for temperature insensitivity, including: (1) combining p-TCR and n-TCR conductive materials [84], (2) selecting suitable conductive nanomaterials and their supporting matrices [60, 85, 86], and (3) modifying electrical properties through chemical treatments.[73]

Combination of p-TCR and n-TCR Conductive Materials

Mixing conductive materials with p-TCR and n-TCR properties can result in a balanced temperature response. The total resistance of the system, represented by the equations below [52, 84] (**Figure 2A)**, depends on the combination of these materials:

$$R_{total} = \sum_{p-TCR} R_{p-TCR} + \sum_{n-TCR} R_{n-TCR} + \sum_{t/h} R_{t/h} \quad (1)$$

$$R_{total} = N_{p-TCR} < R_{p-TCR} > + N_{n-TCR} < R_{n-TCR} > + N_{t/h} < R_{t/h} > \quad (2)$$

$$\frac{d\, R_{total}}{d\, T} = N_{p-TCR} \frac{d < R_{p-TCR} >}{dT} + N_{n-TCR} \frac{d < R_{n-TCR} >}{dT} + N_{t/h} \frac{d < R_{t/h} >}{dT} \quad (3)$$

Here, R_{total} represents the total resistance of the system with series connections of N_{p-TCR} p-TCR material domains, N_{n-TCR} n-TCR material domains, and $N_{t/h}$ tunneling or hopping regions between material domains (i.e., p-TCR domains vs. p-TCR domains, n-TCR domains vs. n-TCR domains, and p-TCR domains vs. n-TCR domains). Each domain or region may have different resistance values—R_{p-TCR}, R_{n-TCR}, and $R_{t/h}$—with corresponding averages $< R_{p-TCR} >$, $< R_{n-TCR} >$, and $< R_{t/h} >$. Equation (3) describes the temperature dependency of each domain, where $d < R_{p-TCR} > / dT$ is positive, while $d < R_{n-TCR} > / dT$ and $d < R_{t/h} > / dT$ are negative. However, N_{p-TCR} and N_{n-TCR} are considered unchanged and are closely related to the ratio of p-TCR to n-TCR materials. $N_{t/h}$ also depends on this ratio and remains unchanged without deformation, though it can vary with different material properties such as shape, size, and distribution. Therefore, optimizing the ratio between p-TCR and n-TCR can induce a near-zero TCR in the sensing materials at the initial stage.

Thermal expansion and deformation during sensing operations can impact these parameters. In fact, the expansion caused by elevated temperatures can alter N_{p-TCR}, N_{p-TCR}, and $N_{t/h}$, disrupting the balance between material connections. This can be minimized by using polymers with low coefficients of thermal expansion (CTE).[87-89] Otherwise, the optimal ratio would compensate for the expansion. Moreover, deformation during sensing operations may also alter N_{p-TCR}, N_{p-TCR}, and $N_{t/h}$. Although some studies have demonstrated stable sensing operations

under varying temperatures [65, 84], detailed investigations on this issue are lacking, making it a subject worth exploring.

Several important factors must be considered when developing near-zero TCR using a combination of p-TCR and n-TCR materials. First, p-TCR materials typically have a higher mass percentage than n-TCR materials [49], as shown by the 45:1 ratio of CSA-doped polyaniline (PANI) (p-TCR) to multi-walled CNTs (MWCNTs) (n-TCR) [90, 91], the 50:1 ratio of Ag Nws (p-TCR) to rGO (n-TCR) [66], and the 0.0033 ratio of single-walled CNTs (SWCNTs) (n-TCR) to GNP (p-TCR) (**Table 1**) [52]. This higher mass of p-TCR in the matrix is explained by Equation (3), in which $d < R_{n-TCR} > / dT$ and $d < R_{t/h} > / dT$ are negative, while $d < R_{p-TCR} > / dT$ is positive. Second, the ratio between n-TCR and p-TCR materials was shown to be unaffected by the method of combination (e.g., the order of deposition). For example, the 0.0033 ratio between SWCNT (n-TCR) and GNP (p-TCR) remained consistent regardless of the order in which the nanomaterials were sprayed (**Figure 2B**).[52] Third, the combination of p-TCR and n-TCR often involves 2D and 1D materials (e.g., 1D CNTs with n-TCR vs. 2D graphite nanoplatelets (GNPs) with p-TCR [52], or 1D Ag Nws with p-TCR vs. 2D graphene with n-TCR [65]). This combination results in stable sensing performance due to its ability to maintain conductive paths between the materials.[57] Additionally, after achieving near-zero TCR with this combination approach, the sensors typically demonstrated stable performance at elevated temperatures, such as between 25 °C and 65 °C.[66, 84]

In contrast to sensors operating at high temperatures, this approach also enables the fabrication of sensors functioning at low or subzero temperatures. Shibin's research group presented two types of strain sensors made from Ag Nws/graphene (10:3 w/w) and AgNPs/CNTs (1.4:1 w/w) with silicone polymer substrates, achieving stable sensing performance at temperatures ranging

from -20 °C to 20 °C.[65, 92] However, extremely low temperatures (-40 °C) induced brittleness in the substrates, increasing the density of microcracks and resulting in unstable sensing performance (**Figure 2C**). Thus, further research on different substrates at low temperatures could help resolve this brittleness issue.

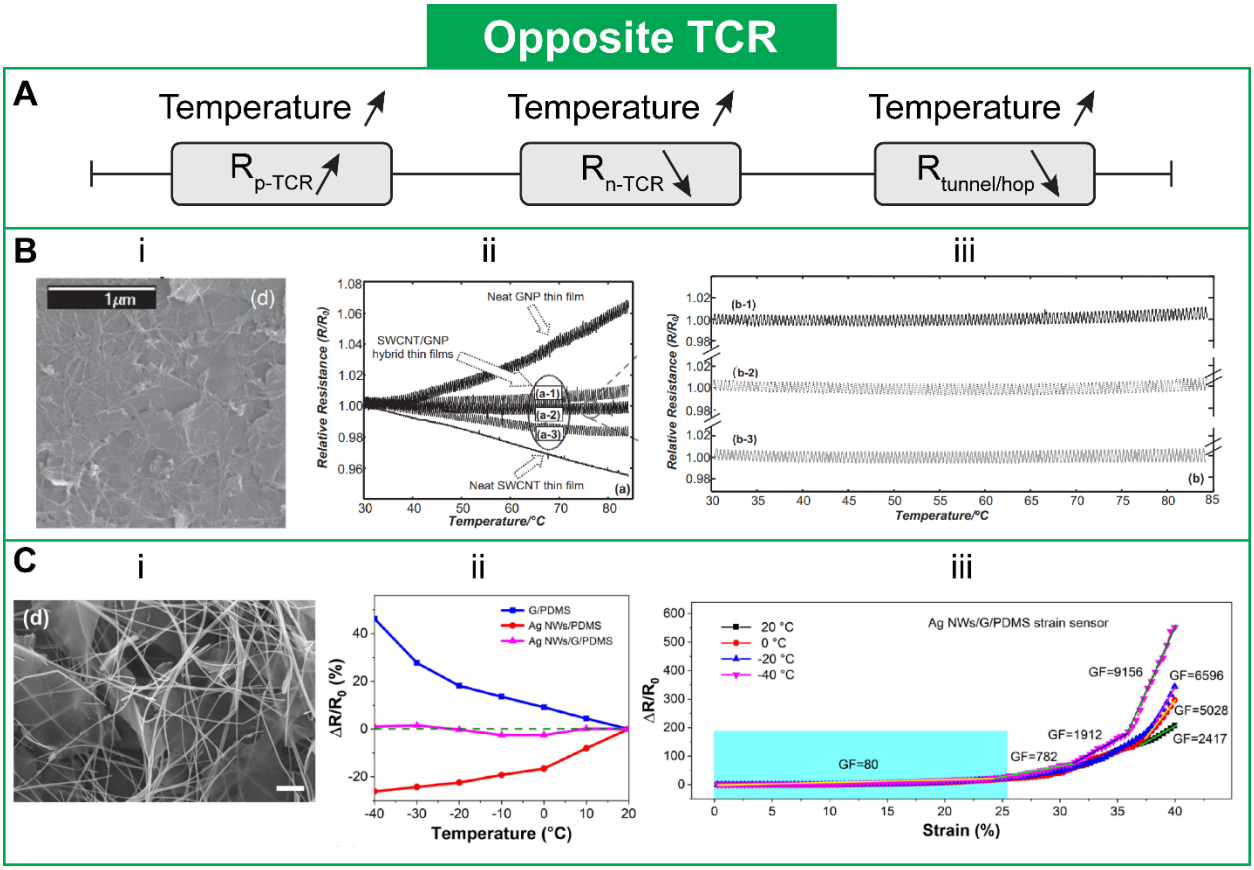

Figure 2. Combination of p-TCR and n-TCR materials for temperature-insensitive piezoresistive sensors. (A) Electrical circuit connecting three types of conductive domains: p-TCR, n-TCR, and tunneling/hopping domains.

(B-i) SEM image of SWCNT/GNP hybrid thin film. (B-ii) Comparison of relative resistance changes for various SWCNT/GNP ratios, with a 0.0033 mass ratio of SWCNT to GNP showing the most temperature stability (a-2). (B-iii) Dynamic stability of the sensor's response under increased temperature, fabricated through these three processes: (top) SWCNT deposited first, then GNP; (middle) GNP deposited first, then SWCNT; and (bottom) a mixture of SWCNT and GNP dispersion. Reprinted with permission from ref [52]. Copyright 2013 John Wiley and Sons.

(C-i) SEM images of Ag NWs/G composite. Scale bar is 1 μm. (C-ii) Small relative resistance changes of the Ag NWs/G composite compared to others at low temperatures. (C-iii) Relative resistance variation in the Ag

NWs/G/PDMS strain sensor in response to applied strain across temperatures from −40 to 20 °C. Reprinted with permission from ref [65]. Copyright 2021 American Chemical Society.

Selection of Conductive Nanomaterials and Their Supporting Matrices

Unlike the combination of two types of conductive materials with opposite TCRs, this subsection discusses the use of only one type of conductive material and its corresponding supporting matrix. This includes p-TCR materials with n-TCR-based supporting matrices, n-TCR materials with p-TCR-based supporting matrices, and conductive materials (e.g., graphene) with uniform supporting matrices.

p-TCR conductive materials can be combined with n-TCR-based supporting matrices to create sensors that are insensitive to temperature. This approach involves embedding one type of p-TCR conductive filler into the supporting matrix at the appropriate loading to achieve near-zero TCR. According to Equation (3), the n-TCR component is removed, as shown in Equation (4) (**Figure 3A**):

$$\frac{d\,R_{total}}{d\,T} = N_{p-TCR}\frac{d < R_{p-TCR} >}{dT} + N_{t/h}\frac{d < R_{t/h} >}{dT} \quad (4)$$

In this approach, the thermal expansion effect on the matrix should be minimal to avoid significant changes in the distance between adjacent material domains, keeping N_{p-TCR} and $N_{t/h}$ constant or nearly constant during sensing operations. Ceramic or low-TEC matrices can be used as substrates, but these rigid matrices may cause unstable performance under static sensing conditions with temperature variation, as discussed below.

A temperature-insensitive strain sensor was developed using GNPs, which exhibit p-TCR, and polysilazane (PSN2) as the n-TCR supporting matrix.[53] To achieve this combination, polysilazane (PSN2) was filled with GNPs and then heat-treated at different temperatures. The authors found that, after heat treatment at 500 °C, the sample with 40 wt% GNPs (GNPs40) had the most stable electrical resistance. **Figure 3B-i** shows the materials with 40% GNP content. This stability was attributed to two factors: (1) the small thermal expansion coefficient of the heat-treated samples ($\sim 10^{-6}$), and (2) the balance between intra-sheet resistance (electron scattering, representing p-TCR) and inter-sheet resistance (hopping or tunneling transport, representing n-TCR) (**Figure 3B-ii**). However, although GNPs40 exhibited stable sensing performance under dynamic strain up to 0.04%, it showed temperature dependence under static strain. This issue arose because the ceramic SiCNO matrix anchored the GNPs, making them difficult to slide. As strain increased the distance between conductive particles, the original equilibrium was disrupted. The problem was solved by heat-treating the ink at 200 °C (transforming the matrix into a polymer) after printing it onto photo paper. This method weakened the interfacial bonding and reduced the stiffness mismatch between GNPs and the polymer matrix, allowing the GNPs to slide relative to each other. This relative sliding of GNPs primarily caused changes in the cross-sectional area, *while the tunneling distance remained unchanged*. Consequently, the electrical resistance changed under strain without interference from temperature. To further explain this temperature-independent behavior, the authors proposed the smallest feature unit to help better understand the mechanism. The sensor with 50% GNPs was found to be stable over a temperature range of 30 °C to 200 °C, maintaining stable sensing performance under both dynamic strain of 0.22% and static strain of $\pm$ 0.32% (**Figure 3B-iii** and **3B-iv**). For clarity, two curing temperatures were used: 500 °C, creating a polymer-

derived ceramic SiCNO matrix, and 200 °C, creating a polymer matrix. The sample cured at 200 °C demonstrated stable sensing performance under both dynamic and static strain. In addition to this report, in the same year, the research team also investigated the temperature insensitivity of TiB_2 conductive nanopowders (p-TCR) dispersed in a polymer-derived ceramic SiCN. With varying TiB_2 content and pyrolysis temperatures, the samples maintained stable electrical resistance at temperatures up to 800 °C. A strain sensor based on these materials also showed stable performance under dynamic strain.[93]

Besides, several additional points regarding these two reports merit further investigation. First, the ceramic matrix (cured at >500 °C) was noted to have a low thermal expansion coefficient ($\sim 10^{-6}$), which contributed to sensor instability in static responses. In contrast, the polymer matrix (cured at 200 °C) was shown to be a better candidate for both static and dynamic responses. However, the thermal expansion coefficient of the polymer matrix has not been reported, leaving uncertainty about whether thermal expansion might affect its stability. Second, the conductive material loading for the polymer matrix was significantly higher - 50% or even 80% - compared to the ceramic matrix, to achieve near-zero TCR. This higher loading reduced the spacing between adjacent fillers, increasing the likelihood of tunneling or hopping, which is beneficial for electron transport. On the other hand, curing polysilazane at higher temperatures to create the ceramic matrix resulted in matrix shrinkage, reducing the filler spacing and allowing for lower filler loading. Further exploration of other polymer substrates, such as polydimethylsiloxane (PDMS), would be valuable, particularly for soft substrates intended for applications like wearable sensors on human skin.

The second approach involves using n-TCR materials with a p-TCR-based supporting matrix, balancing the resistance changes of n-TCR materials (decreasing resistance) with the thermal expansion effect (increasing resistance) as temperature changes (see Equations (5) and (6)).

$$R_{total} = N_{n-TCR} < R_{n-TCR} > + N_{t/h} < R_{t/h} > \quad (5)$$

$$\frac{d\, R_{total}}{d\, T} = \frac{d\, N_{n-TCR} < R_{n-TCR} >}{dT} + \frac{d\, N_{t/h} < R_{t/h} >}{dT} \quad (6)$$

Unlike the first method, the thermal expansion effect in this medium is moderate, so N_{n-TCR} and $N_{t/h}$ are not constant. While R_{n-TCR} and $R_{t/h}$ decrease with increasing temperature, thermal expansion can widen the distance between or even break conductive domains, leading to an increase in $N_{n-TCR} < R_{n-TCR} >$ and $N_{t/h} < R_{t/h} >$. The two mechanisms counteract each other, resulting in a near-zero TCR as the temperature increases. A simplified circuit sketch illustrating this is shown in **Figure 3C**, where the resistance from thermal expansion (represented as p-TCR) compensates for the other effects.

For example, Taesung Park *et al.* spin-coated a solution of indium tin oxide (ITO) and Au nanoparticles onto PDMS/ polyethylene terephthalate (PET) substrates with varying PDMS thicknesses.[60] ITO/Au was chosen as the sensing material for its high conductivity and optical transparency (after a ligand exchange process). This sensing layer exhibited n-TCR due to the thermally assisted electron-hopping mechanism, where electrons transport between particles with the added energy from temperature. In contrast, the PDMS/PET substrate with a 0.8 mm thickness displayed moderate thermal expansion, increasing the distance between the particles (leading to p-TCR) and thereby compensating for the n-TCR of the ITO/Au (**Figure 3D**). The bottom PET layer, with its low thermal expansion coefficient, constrained the thermal expansion

of the PDMS layer, helping control the overall thermal expansion of the sensor's top layer. A near-zero TCR was achieved in the 25 °C to 45 °C temperature range. The sensor also demonstrated high sensitivity as a strain sensor, with a gauge factor (GF) of over 7000 at just 0.4% strain, due to the wrinkles and cracks in the PDMS substrate. Finger-bending tests confirmed stable resistance changes at temperatures of 26.1 °C and 44.8 °C.

Inspired by this study, a temperature-insensitive pressure sensor was developed and investigated for stable sensing performance under varying temperatures. $Ti_3C_2T_x$ Mxene, an n-TCR material [26], was sandwiched between PET and PDMS substrates. An optimal PDMS thickness was determined, resulting in a near-zero TCR of 2.1 x 10^{-5} $°C^{-1}$.[94] The sensor design featured a small square hollow for pressure sensing, with silver nanoparticles (AgNPs) used as contact electrodes. The sensor demonstrated temperature-insensitive performance at 25 °C, 35 °C, and 45 °C (**Figure 3E**). The stability of the sensing operation can be explained as follows: first, the expansion of the PDMS compensated for the decreased resistance of the MXene layer, while simultaneously increasing the resistance of the silver film. However, the resistance of the silver film was significantly smaller than that of the initial MXene layer, so temperature changes had little impact on the overall sensor resistance. Second, mechanical deformation (pressure) only affected the contact between the silver film and the square hollow MXene layer, leaving the near-zero TCR MXene layer unaffected by applied pressure. As a result, the sensor maintained temperature insensitivity during operation.

Additionally, Shen *at. al* have both theoretically and experimentally investigated piezoresistive strain sensors based on CNTs dispersed in epoxy resin (both materials had very low thermal expansion coefficients—on the order of 10^{-6}).[72] Their results showed that 3 wt% CNT loadings achieved zero TCR, with stable resistance across temperatures ranging from ~230 K to ~370 K,

while 2 wt% CNT loadings demonstrated temperature-independent GF within the same range (**Figure 3F)**. The authors conclude that the key to achieving temperature-independent CNT/polymer strain sensors lies in the "proper dispersion of treated and selected CNTs in a well-matched polymer matrix". Important factors for achieving temperature independence include CNT loadings, the length-to-diameter ratio of CNTs, their agglomeration state, and the thermal expansion coefficient of the polymer matrix. Therefore, while achieving near-zero or zero TCR is often the primary goal, it does not necessarily guarantee temperature-independent performance, as mechanical deformations can still influence the distance between conductive domains.

The third method involves using graphene, which has a low TCR (on the order of 10^{-4} [95, 96]), combined with uniform supporting matrices to create temperature-insensitive sensors. Haicheng *et al.* attributed this temperature insensitivity to two factors.[85] First, graphene's small, negative thermal expansion coefficient (-8.0×10^{-6} K^{-1}) helps counteract the expansion of softer polymer matrices, such as PDMS. Second, the small TCR of graphene itself results in minimal temperature dependence. The authors also addressed the issue of graphene restacking or aggregation, which can affect the uniformity of the coating. They proposed using a graphene oxide interfacial layer between the graphene and the elastomer interface (hydrophobic microstructured PDMS) to promote uniform coating. The resulting pressure sensor demonstrated stable performance across a temperature range of 25 °C to 60 °C (**Figure 3G)**. This uniform coating reduces random increases in distance between aggregated conductive domains, contributing to temperature insensitivity. Additionally, two other reports integrated graphene with porous polymer structures [97, 98], where uniform graphene distribution was challenging,

especially when mixing graphene with polymers mechanically.[98] As a result, the sensing performance remained stable only within a limited temperature range ($\Delta T \leq 20\ ^{\circ}C$) (**Figure 3H**).

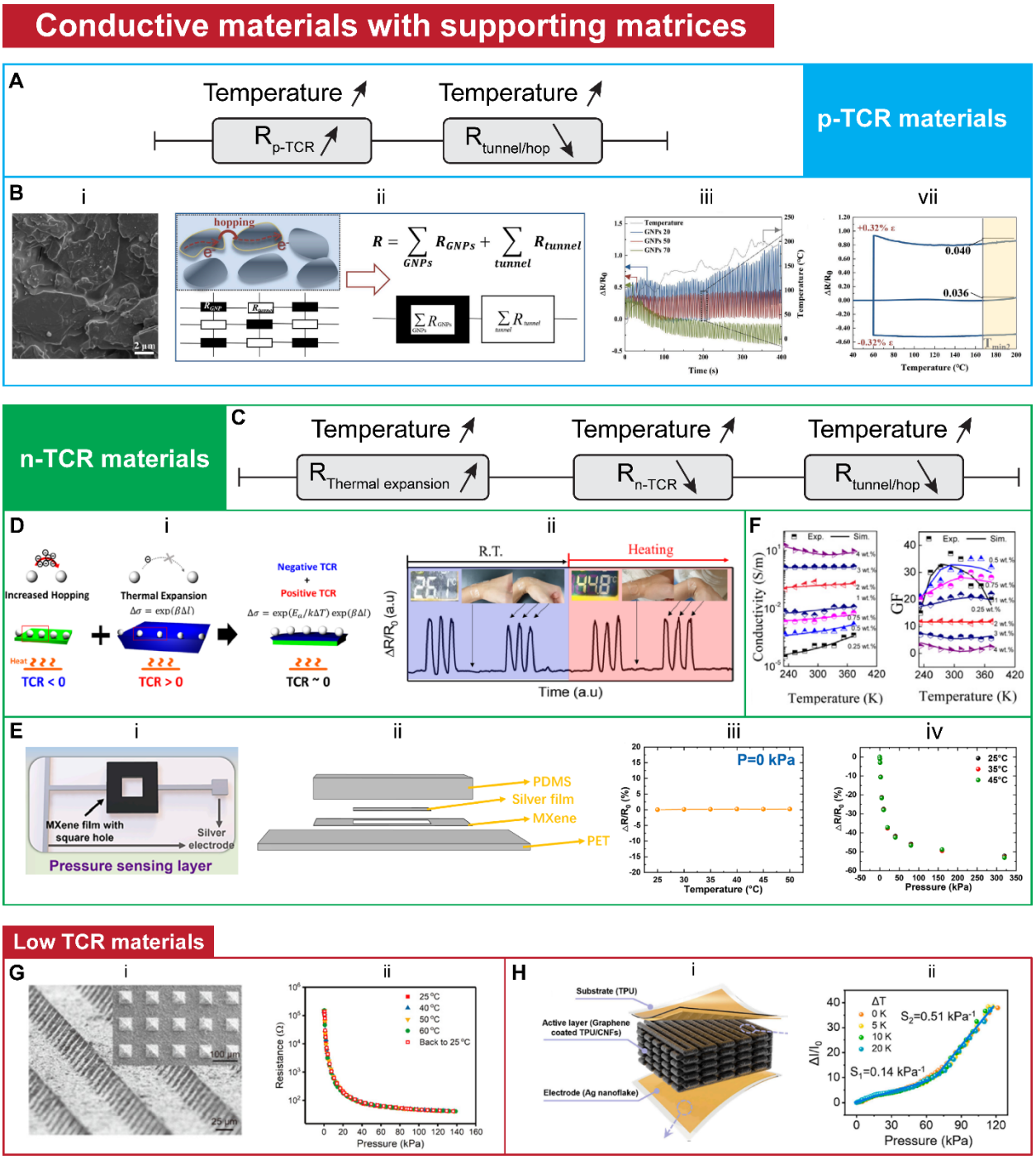

Figure 3. Utilizing single conductive materials for temperature-insensitive piezoresistive sensors.

(A) Electrical circuit connecting two types of conductive domains: p-TCR material domains and tunneling/hopping domains.
(B-i) SEM images of GNP/SiCNO films with 40% GNP content. (B-ii) Equivalent circuit of GNP conductive composites, illustrating the balance between intrinsic resistance changes and thermal-assistance tunneling resistance, achieving near-zero TCR. (B-iii) and (B-iv) Stable dynamic and static responses of the 50% GNPs sensors fabricated by drawing ink onto photo paper and heat-treating at 200 °C. Reprinted with permission from ref [53]. Copyright 2023 Elsevier.
(C) Simplified circuit showing increased resistance due to thermal expansion, compensating for decreased resistance from n-TCR domains and tunneling/hopping domains.
(D-i) Illustrations of compensation between thermal-assisted hopping and thermal expansion to achieve near-zero TCR. (D-ii) Stable electrical response under bending tests at room temperature (blue) and hot environments (red). Reprinted with permission from ref [60]. Copyright 2021 American Chemical Society
(E-i) and (E-ii) Schematic of a pressure sensor based on hollow MXene film. (E-iii) and (E-iv) Stable initial resistance and sensor performance across different temperatures. Reprinted with permission from ref [94]. Copyright 2024 Elsevier.
(F) Experimental and simulation results indicating 3 wt% CNT loading for stable conductivity (left) and 2 wt% CNT loading for stable sensitivity (right) under temperature variations. Reprinted with permission from ref [72]. Copyright 2018 Elsevier.
(G-i) SEM images showing a micropyramid array coated with a Gr/GO layer. (G-ii) Stable sensor performance under temperature changes for the graphene-coated sensor. Reprinted with permission from ref [85]. Copyright 2020 American Chemical Society.
(H-i) The overall assembly of a graphene-based sensor, composed of a hierarchical porous graphene-coated thermoplastic polyurethane/carbon nanofibers (graphene-coated TPU/CNFs). (H-ii) Stable sensor performance across different temperature gradients. Reprinted with permission from ref [97]. Copyright 2022 Elsevier.

Altering Electrical Properties Through Chemical Treatment

Semiconducting materials can be chemically treated to achieve temperature-insensitive electrical conduction. For example, untreated semiconducting polymer PEDOT:PSS typically exhibits n-TCR behavior.[82, 83] However, after treatment with dimethylsulfoxide (DMSO) vapor, the polymer's conductivity became temperature-independent while maintaining its thermoelectric properties (**Figure 4A**).[54] This treatment induced an "activated free transport" regime, occurring

at the transition between the insulator and semimetallic states of the polymer aerogel. Other polar solvents like ethylene glycol (EG) and diethylene glycol (DEG) have also been shown to stabilize PEDOT:PSS conductivity under varying temperatures.[82, 99] In addition to improving electrical properties, the mechanical strength and elasticity of PEDOT:PSS sensors can be improved by adding glycidoxypropyl trimethoxysilane (GOPS) and nanofibrillated cellulose (NFC).[54]

These early results have inspired further research into PEDOT:PSS for temperature-independent pressure sensors [50, 73, 100] and strain sensors.[74] For instance, to fabricate temperature-independent pressure sensors, PEDOT:PSS-based ink with good rheological behavior was formulated through a multi-step process: (1) adding 5 vol% DMSO to the PEDOT:PSS solution, (2) introducing a tackifier (WH-1005) to meet viscosity requirements, (3) adding FS-30 to reduce surface tension, and (4) incorporating water-based polyurethane (WPU) to enhance mechanical properties (**Figure 4B-i**). This ink was then printed conformally on surface-treated microstructured PDMS, yielding high sensitivity (134.25 kPa^{-1} in the 50 kPa range and 37.65 kPa^{-1} in the 300 kPa range) with resistance unaffected by temperatures ranging from 15 °C to 90 °C (**Figure 4B-ii).**[73] Moreover, PEDOT:PSS doped with 3 vol% DMSO was used in strain sensors, which demonstrated stable resistance changes under cyclic strain between 298 K to 320 K (**Figure 4C**). However, the sensor had a relatively low GF (~2) within a 2% bending strain range.[74]

Beyond PEDOT:PSS, polypyrrole (PPy) was also treated with phytic acid, which acted both as a dopant and a crosslinker.[75] Phytic acid, being a non-volatile dopant, ensured stable conductivity at higher temperatures. Its crosslinking effect allowed more PPy chains to interact with a single phytic acid molecule, further stabilizing PPy's conductivity. The treated PPy was used in pressure sensors with a porous foam structure, but the sensing mechanism was based on physical

contact at electrode interfaces, minimizing the impact of thermal expansion on the bulk material. The microstructured porous PPy demonstrated high sensitivity (up to 133.1 kPa^{-1}) in the low-pressure regime (< 30 Pa), with only a slight signal drift over a temperature range from -10 °C to 100 °C (**Figure 4D**)**.**

Another approach for developing temperature-insensitive electromechanical sensors is chemical reduction, particularly applied to graphene oxide (GO).[47] GO is typically reduced using ascorbic acid, a green reducing agent, to form rGO. Normally, charge hopping within and between nanosheets is temperature-dependent. However, after GO is reduced, many negative groups are eliminated, reducing deeper trap states and leading to the formation of shallow trap states that promote short-range charge-hopping. These effects decrease the number of charges hopping (**Figure 4E-i**). This reduced rGO was coated onto *Calotropis gigantea* yarns to fabricate fiber-based strain sensors (**Figure 4E-ii**). These sensors exhibited stable initial resistance and consistent resistance changes under dynamic strain (15%) at temperatures ranging from 22.8 °C to 47.3 °C (**Figure 4E-iii** and **4E-iv**). However, the sensor's sensitivity was relatively low (~3) within a 50% strain range.

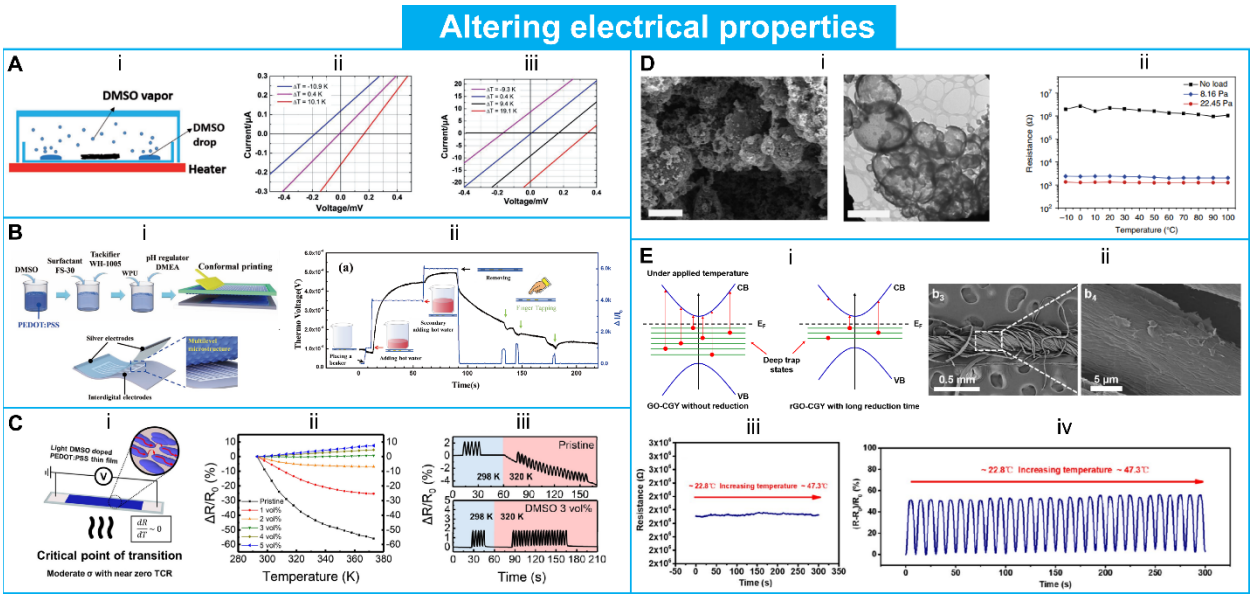

Figure 4. Modification of electrical properties for temperature-insensitive piezoresistive sensors.

(A-i) Schematic of PEDOT:PSS treated with DMSO vapor. (A-ii) and (A-iii) I-V curves at constant pressure with varying temperature, before and after 10 minutes of DMSO treatment, respectively. Reprinted with permission from ref [54]. Copyright 2017 John Wiley and Sons.

(B-i) Screen-printing PEDOT:PSS-based functional ink with additives for temperature-independent pressure sensors. (B-ii) Stable current response to pressure under temperature variation from hot water (right axis). Reprinted with permission under a Creative Commons CC BY 4.0 License from ref [73]. Copyright 2022 John Wiley and Sons.

(C-i) Schematic of PEDOT:PSS doped with DMSO to achieve near-zero TCR. (C-ii) 3 vol% DMSO-doped PEDOT:PSS yields near-zero TCR. (C-iii) Stable sensing performance of 3 vol% DMSO-doped PEDOT:PSS compared to the pristine version at two different temperatures. Reprinted with permission from ref [74]. Copyright 2023 The Royal Society of Chemistry.

(D-i) SEM of PPy thin film (scale bar: 10 mm (left)) and TEM image unveiling its interconnected hollow-sphere structure (scale bar: 1 mm (right)). (D-ii) Temperature-dependent resistance response of the porous PPy pressure sensor. Reprinted with permission from ref [75]. Copyright 2014 Springer Nature.

(E-i) Energy-band structure and thermal charge generation in GO-functionalized yarns before and after long reduction. (E-ii) Surface morphology of rGO-coated *Calotropis gigantea* yarn. (E-iii) and (E-iv) Stable initial resistance and dynamic response of sensors at 15% strain, as temperature increases from 22.8 °C to 47.3 °C. Reprinted with permission under a Creative Commons CC BY 4.0 License from [47]. Copyright 2023 Springer Nature.

Temperature-Insensitive Electromechanical Sensors Based on Capacitive and Triboelectric Effects

In addition to piezoresistive sensors, which are low-cost and widely studied, capacitive sensors (which operate based on changes in capacitance) offer low power consumption and fast dynamic response.[16, 101] On the other hand, triboelectric sensors enable self-powered systems with a wide range of material choices.[102, 103] These advantages make both types of sensors suitable candidates for human electromechanical monitoring.[34, 104] However, temperature can still influence their performance. Proper selection or development of suitable sensing materials can mitigate temperature effects. This subsection will discuss material strategies for temperature-independent capacitive and triboelectric sensors.

Capacitive Sensors Insensitive to Temperature by Curating Dielectric Materials

Temperature can affect the performance of capacitive pressure sensors by altering the sensing materials. In principle, capacitive sensors respond to pressure by altering either the geometry or the dielectric properties of the sensing materials. Capacitance represents the ability to store charge, which ideally should remain unaffected by temperature.[105-107] However, thermal effects can cause changes in both the dielectric properties and geometry of the dielectric or electrode layers, leading to fluctuations in capacitance. For example, PDMS, commonly used as a dielectric material, has a large thermal expansion coefficient (310×10^{-6} °C^{-1}), which can result in significant signal shifts between room temperature and 40 °C.[108] Additionally, the dielectric constant of materials can vary with temperature [109], affecting the sensor's performance.

To address this issue, it is necessary to choose or develop materials with stable dielectric properties and geometry under varying temperatures. Two types of dielectric materials are commonly used: ceramics and polymers.

Ceramic materials are promising for creating stable wearable capacitive sensors that can operate under temperature variations, despite their inherent stiffness. Ceramics generally have low thermal expansion coefficients (see Table 2), which minimizes changes in geometry. Furthermore, the dielectric constant of ceramics can remain stable over a wide temperature range. For example, Al_2O_3 or PNb_9O_{25} have been shown to maintain stable dielectric constants at temperatures up to 200 °C and 100 °C, respectively.[110, 111] Additionally, quasi-free charge carriers in ceramics can be "frozen" at low temperatures, preventing dipole reorientation and stabilizing the dielectric constant. Doping ceramics, such as $BaTiO_3$, with appropriate dopants can also optimize the material structure, extending the temperature range over which dielectric properties remain stable.[112] To address the stiffness of ceramics, ultrathin films (e.g., on the nanometer scale) can be fabricated.[6]

For example, Geun *et al.* presented a temperature-insensitive capacitive pressure sensor using nanolayer Al_2O_3 or SiO_2 as the dielectric layer.[109] One electrode consisted of conductive SWCNTs embedded in the surface of microstructured PDMS. The pressure sensor exhibited temperature insensitivity from 22 °C to 70 °C, with only a 3.6% change in sensitivity (**Figure 5A**). The authors stated that the thermal expansion of PDMS had a negligible effect on contact area changes, which contributed to the sensing response. It is inferred that the SWCNTs (with a thermal expansion coefficient on the order of 10^{-6}, [113, 114] much lower than that of PDMS, on the order of 10^{-4} [115]) helped mitigate PDMS's thermal expansion.

In extreme environments, such as those encountered by firefighters, capacitive sensors must also withstand high temperatures. Min *et al.* developed a capacitive pressure sensor using electrospun ceramic titanium dioxide (TiO_2) nanofibers as the dielectric layer, paired with carbon fiber cloth electrodes.[38] The sensor demonstrated stability at temperatures ranging from 30 °C to 370 °C and could even survive exposure to a butane flame, withstanding temperatures as high as ~1300 °C (**Figure 5B**).

Polymers are flexible and ideal for soft sensors, but they require stable dielectric properties and geometry to ensure consistent performance. However, the dielectric constant of polymers typically fluctuates with temperature due to unstable intermolecular forces, thermal agitation, and segmental motion induced by thermal energy.[116-118] This issue can be resolved by incorporating additives to improve the rigidity of the polymer.[119, 120] For example, Zejun *et al.* introduced fluorene-containing fluorinated polyethersulfone (PES-6AF/BHPF) copolymers that maintain a stable dielectric constant up to 180 °C, near their glass transition temperature.[121] This stability is attributed to the incorporation of BHPF, which increases polymer rigidity and raises the glass transition temperature to 260 °C. Blending two materials with different crystalline transition temperatures can also help achieve temperature-independent dielectric properties.[122] For instance, blending PVDF-based terpolymers and copolymers results in a stable dielectric constant within 80 °C, due to the redistribution of chains into two crystalline phases. These phases have distinct transition temperatures, allowing for a stable dielectric constant as their maxima overlap.[123] In addition to dielectric stability, maintaining a stable geometry is crucial. Table 2 lists the TCEs of some polymers, which range from high to low. Although there is limited information about the TCRs of these modified polymers, it is anticipated that the support of polymers with low TCRs could reduce the effect of thermal expansion when necessary.[60]

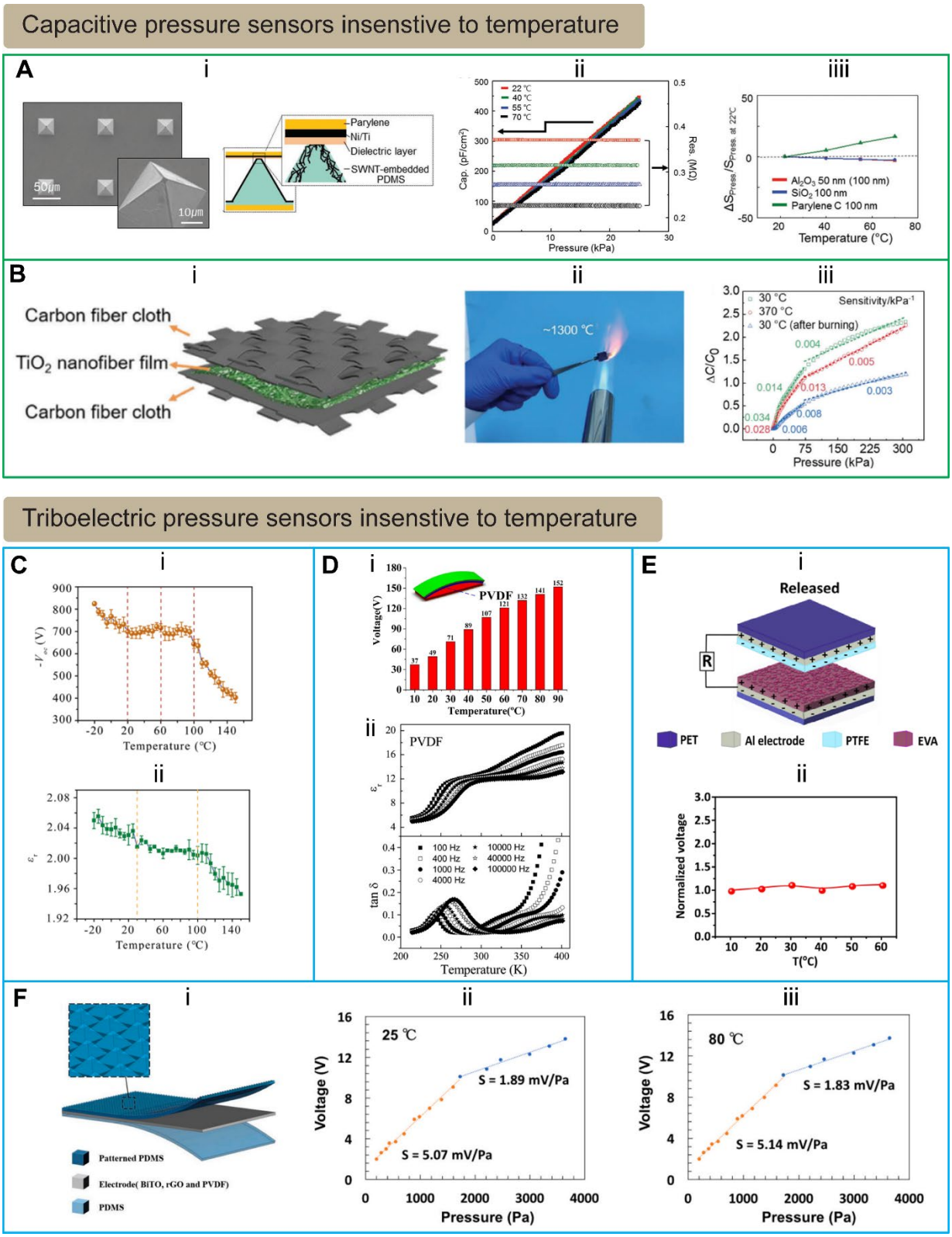

Figure 5. Factors affecting temperature-insensitivity in capacitive and triboelectric pressure sensors, along with approaches to achieve it.

(A-i) SEM image of conductive truncated pyramidal microstructures embedded with SWNT on the surface. (A-ii) Stable capacitance response of the pressure sensor using a nano-thick Al_2O_3 dielectric layer under temperature variations. (A-iii) Stable relative pressure sensitivity using these dielectric materials across varying temperatures. Reprinted with permission from ref [109]. Copyright 2018 John Wiley and Sons.
(B-i) Schematic of TiO_2 nanofiber pressure sensor designed for high-temperature resistance. (B-ii) Photograph of the sensor after being burned by a butane flame (~1300 °C). (B-iii) Sensing performance of the sensor was tested at 30 °C, 370 °C, and then back to 30 °C after exposure to the butane flame. Reprinted with permission under a Creative Commons CC BY 4.0 License from ref [38]. Copyright 2020 John Wiley and Sons.
(C-i) and (C-ii) Open-circuit voltage and dielectric constant of PTFE-based TENG (PTFE-Al pair) under temperatures ranging from -20 °C to 150 °C. Reprinted with permission from ref [124]. Copyright 2017 John Wiley and Sons.
(D-i) Increase in the output voltage of PVDF-PTFE-based TENG under temperature variation from 10 °C to 90 °C. Reprinted with permission from ref [125]. Copyright 2018 Springer Nature. (D-ii) Temperature-induced increase in the dielectric constant of PVDF thin film. Reprinted with permission from ref [122]. Copyright 2013 Elsevier.
(E-i) Schematic of a TENG based on contact between PTFE and EVA. (E-ii) Normalized voltage output of the TENG over a temperature range of 10 °C to 60 °C. Reprinted with permission from ref [126]. Copyright 2023 John Wiley and Sons.
(F-i) Schematic of a tactile e-skin based on patterned pyramidal microstructures on a PDMS surface. (F-ii) and (F-iii) Sensor performance at room temperature and 80 °C, respectively. Reprinted with permission from ref [127]. Copyright 2020 Elsevier.

Triboelectric Sensors Insensitive to Temperature by Curating Working Materials

Temperature can also negatively affect the performance of triboelectric sensors, or triboelectric nanogenerators (TENGs), which combine triboelectrification (contact electrification) and electrostatic induction. During contact electrification, static charges are generated on the surfaces of two materials with differing electron affinities, such as dielectrics and metals. A high contact area is crucial for achieving a high charge density and therefore improved signal output. The electrostatic induction effect causes charge movement through an external circuit, generating a

signal.[128] Temperature changes can cause surface charge loss and affect the charge transfer through the external circuit.

Selecting or developing contact materials with stable dielectric constants can help mitigate temperature effects in triboelectric sensors. The dielectric constant influences both the surface charge generated by triboelectrification and the short-circuit transferred charge through the external circuit.[128, 129] As a result, a temperature-dependent dielectric constant leads to an unstable output current. The dielectric constant also reflects a material's ability to store and gain electrons. As temperature increases, surface charge, open voltage, and dielectric constant typically decreases. This occurs because thermal excitation can cause surface charge to escape, reducing surface charge density.[130] Another explanation for this reduction is that higher temperatures can cause greater absorption of lower electron-affinity oxygen atoms into thin polymer layers, such as polytetrafluoroethylene (PTFE). These oxygen atoms replace fluorine in PTFE, increasing the molecular weight of the thin layer, and thus lowering the dielectric constant, as explained by the Clausius–Mossotti relation (**Figure 5C)**.[124] While temperature negatively impacts electron storage, rapid deterioration of both the open-circuit voltage of PTFE-based TENGs and the dielectric constant of PTFE has been observed at temperatures above 100 °C, though they change insignificantly at lower temperatures (**Figure 5C**). In contrast to PTFE, which shows decreases in both output performance and dielectric constant at elevated temperatures, polyvinylidene fluoride (PVDF) exhibits an increase in dielectric constant [122, 131, 132] and output voltage between 10 °C and 90 °C when in contact with PTFE (**Figure 5D**).[125] This suggests that the stability of the dielectric constant is closely related to the stability of surface charge in contact materials.

Based on this analysis, selecting or developing materials with dielectric constants that remain stable over the desired temperature range is key to ensuring consistent performance in triboelectric sensors. For example, Smitha *et al.* used PTFE and ethylene vinyl acetate (EVA) as contact materials.[126] Their TENG demonstrated stable performance from 10 °C to 60 °C, attributed to the materials' stable dielectric properties at lower temperatures. However, EVA became sticky at 60 °C, limiting contact and separation with PTFE, which subsequently impacted performance (**Figure 5E**). Additionally, the modified dielectric materials discussed in the capacitive sensors section could serve as promising candidates for temperature-insensitive triboelectric sensors.

Apart from maintaining stable dielectric constants, thermal expansion effects on contact materials must also be considered. A high CTE can alter the contact area, leading to unstable sensor performance. This is an area for future research.

Interestingly, microstructured PDMS has also been used as a triboelectric material, showing stable sensing performance across a temperature range from 25 °C to 80 °C (**Figure 5F**).[127, 133] The authors noted that the internal resistance of the TENG was significantly higher than that of the electrodes, minimizing the impact of temperature. If the electrode resistance were comparable to the internal resistance, temperature changes could lead to instability. However, the dielectric constant of PDMS decreases with increased temperature.[134, 135] It is suspected that PDMS's thermal expansion may contribute to an increase in the contact area, compensating for the loss of surface charge.

The effectiveness of the methods to achieve strain and pressure sensors insensitive to temperature has been proved through wearable applications during temperature variations. For

examples, temperature-insensitive soft strain sensors were attached on a finger, wrist, elbow, or knee to monitor joint movement under different set temperatures including subzero temperature (-20 ℃).[53, 60, 65, 74, 87, 92] The detected signals exhibited consistent dynamic and static response with the highest 2% error reported.[65, 87] Nevertheless, the stable sensing range was often limited to less than 10% or even 1% (Table 4), which could restrict the applications of the strain sensors in other fields (e.g., robotics). The primary cause of this low sensing range is the broken balance of resistance between fillers and substrates under higher strains. Adopting stretchable designs, such as triangular open mesh, can extend the strain range.[92] Temperature-independent soft pressure sensors were adhered onto the wrist to detect human pulse, showing minimal thermal drift under lamp heating to 45 ℃.[78] The pressure sensors were also arranged into array for mapping of external stimuli and were made in contact with objects under temperature variations. The stable output responses indicated the potential of temperature-insensitive soft pressure sensors for reliable human-machine interaction and robotic recognition. [94, 109, 136]

Materials Engineering for Electromechanical Sensors Insensitivity to Humidity or Liquid Contact

In practical applications, soft strain and pressure sensors can undergo various wet conditions, such as outdoor-indoor humidity differences or exposure to water in rain or underwater.[137, 138] In wearable human sensing, these sensors are also susceptible to corrosion caused by sweat during human activities.[48] Such conditions comprise the integrity of sensing materials, particularly in terms of electrical, dielectric, and geometrical properties. This degradation negatively impacts the stability of sensing operations. One effective strategy to ensure stable sensing performance is to separate important materials (e.g., active conductive materials) with humidity and liquids. While full encapsulation offers an easy solution, it limits both the permeability of the sensor and

its self-cleaning or chemical resistance capabilities. Thus, alternative approaches may be more beneficial in specific scenarios. Below, we summarize various strategies to mitigate the effects of humidity or liquid exposure, including surface morphology modifications, chemical treatments, and also encapsulation.

Humidity- or Liquid-Contact-Insensitive Electromechanical Sensors Based on the Piezoresistive Principle

Piezoresistive sensors operate by detecting changes in the electrical resistance of sensing materials when subjected to mechanical deformation. However, water molecules can influence the sensor's performance through chemical reactions or absorption, significantly altering its resistance. First, it is well known that metals corrode in the presence of water molecules due to chemical reactions.[139] In flexible devices, Ag NWs are commonly used, but their electrical stability decreases under humid conditions because water and oxygen accelerate chemical reactions, forming silver sulfide and causing film failure.[140, 141] Second, water molecule absorption can affect the conductivity of conductive materials. For example, while free-standing graphene sheets are resistant to water molecules [142], graphene's conductivity can be altered when placed on a defective substrate (such as SiO_2) due to the electrostatic dipole moments of water molecules.[143, 144] Additionally, water absorption can cause swelling in conductive polymers, such as PEDOT:PSS, which contains hydrophilic PSS. This swelling increases the distance between PEDOT chains, reducing electrical conductivity.[27] Water absorption can also cause swelling in hydrophilic matrices (e.g., PVA or cellulose), increasing the distance between conductive nanofillers and thus raising electrical resistance.[61] Another common reason is the increase in ionic conductivity caused by water molecules absorbed either on the surface of conductive materials or within a composite matrix.[61-64] Although humidity and water significantly impact

sensing performance, one effective countermeasure is to protect the active (conductive) materials with hydrophobic substances, reducing water absorption.

One approach is to fully encapsulate the sensing material in hydrophobic substances, such as polyimide (PI), PDMS, or Ecoflex.[35, 145-147] This method provides straightforward protection, but has drawbacks. For instance, while non-modified PDMS is impermeable and has low surface energy (contact angle ~116°) [148], which helps prevent liquid penetration into conductive paths, thick encapsulation layers may reduce sensing accuracy due to poor surface compliance.[6] Furthermore, desirable properties such as self-cleaning, corrosion resistance, and permeability are challenging to achieve with simple hydrophobic encapsulation.[149, 150]

Superhydrophobic surfaces, however, offer enhanced advantages. They not only provide reliable performance in wet conditions but can also improve sensor sensitivity.[151, 152] Consequently, research has focused on integrating superhydrophobic or super-liquid-repellent surfaces into sensors.[29, 55, 138, 153-157] Superhydrophobic surfaces are characterized by a high contact angle (CA) (> 150°), low contact angle hysteresis, and a low sliding angle (SA) (< 10°).[158, 159]

In theory, materials with low surface energy and high roughness exhibit these superhydrophobic properties. Low surface energy encourages water molecules to cluster together, resulting in less contact with the surface and a higher contact angle.[160] When combined with a rough surface, water droplets are suspended on surface features due to air cushions, a phenomenon known as the Cassie–Baxter state, which produces superhydrophobic properties (CA > 150°).[161] In this state, not only water but also other liquids (e.g., tea, milk, coffee) can be repelled.[56] In contrast, when liquid droplets fully contact the rough surface, the CA decreases, allowing liquids to penetrate conductive paths. This is known as the Wenzel state.[162] Therefore, fabricating

piezoresistive sensors that maintain a Cassie–Baxter state during operation minimizes liquid contact and enhances sensor durability, even in corrosive environments (acidic or basic).[163]

Various materials can be used to impart superhydrophobic properties while maintaining desirable sensing performance. Low surface-area materials include vulcanized silicone rubber (RTV) [151], common PDMS [164], and SiO_2 nanoparticles [165], which are fluorine-free. Fluorine-rich options include (heptadecafluoro-1,1,2,2-tetradecyl) trimethoxysilane (FAS) [55] and 1H,1H,2H,2H-perfuorodecanethiol (PFDT).[166] Conductive materials typically consist of carbon-based components, such as CBNPs, CNTs, graphene, or rGO.[138, 163, 164, 167] Adhesive materials, such as PDA [168] or APTES [55], may also be needed to ensure secure interactions between different components. The choice of materials will vary depending on the specific application, with fluorine-free options potentially more attractive for minimizing negative impacts on human skin.

In the following discussion, we categorize materials engineering strategies for achieving superhydrophobic surfaces into three groups: *single microstructure surfaces, hierarchical surfaces, and superhydrophobic porous structures*. The first two categories apply to non-permeable sensors, while the third focuses on permeable designs. Additionally, another approach involves using *chemical treatments* to minimize the interaction between materials and water molecules.

Single Feature Surface

A single feature surface, also known as a single microstructure surface, refers to a surface structure that contrasts with hierarchical structures discussed later. This type of surface enhances roughness, and its fabrication process is relatively simple, typically involving just two steps.

There are two main approaches to achieve this surface: (1) orderly coating and (2) post-treatment.

The first approach, orderly coating, involves creating a conductive surface with an initial roughness and then coating it with low-surface-energy polymers or nanomaterials/polymers. The roughness is typically generated by the conductive nanomaterial, resulting in a single-feature surface. This conductive surface can be fabricated by dispersing conductive materials in polymers and coating them onto substrates [29, 153], by absorbing the materials onto polymers via swelling [164], or by embedding nanomaterials at the air/water interface into polymers.[48] The second step involves covering the conductive surface through spray coating, spin coating, or dip coating with a polymer or nanomaterial/polymer suspension. This process not only increases the contact angle and lowers the sliding angle but also enhances adhesion between the conductive nanomaterials and the substrate. However, despite good adhesion, physical damage (such as abrasion) can degrade both the superhydrophobic and electrical properties of the surface.[29, 164] The hierarchical surface approach, discussed later, can help minimize the impact of abrasion.

In the case of nanomaterials like MWCNTs at the air/water interface, CNTs on the air side are fully embedded into TPE, while those on the water side are covered by injecting PDMS dispersion into the aqueous phase.[48] The final product is a thin (~20 μm), superhydrophobic surface with stable initial resistance and contact angle, even when immersed in various liquids (e.g., water, salt, acid/alkali) (**Figure 6A**). The concentration of PDMS must be low (< 4%) because higher amounts can form a thick coating layer that buries the CNTs, reducing surface roughness and negatively affecting the film's inductive sensitivity.

In addition to nanomaterials, a simple pre-strain method can produce a wrinkled surface structure that controls roughness, which is beneficial for strain sensors.[51] For example, pre-strained VBH/rGO at different strain levels is coated with PDMS/hexane using spin-coating, creating different degrees of roughness and corresponding contact angles (**Figure 6B-i** and **6B-ii**). The report examined how water droplets affected resistance, noting that droplets bounced off the superhydrophobic surface. This behavior was maintained even at strain levels up to 400%, demonstrating the surface's durability under strain. However, electrical resistance increased slightly (< 3%) with 20 μL droplets (**Figures 6B-iii** and **6B-iv**). This was due to charge transfer between water molecules and the sensor, not gravity. Additionally, the sensor demonstrated stable dynamic responses to acid, alkali, and salt exposure (**Figure 6B-v**). Nevertheless, performance was less stable in moist environments, likely due to smaller water vapor molecules (**Figure 6B-vi**). Increasing the PDMS content in the coating may offer better protection, but excessive amounts would reduce surface roughness and, consequently, compromise superhydrophobicity.

The second approach, post-treatment, involves depositing conductive materials and polymers onto substrates, followed by post-treatment without adding additional materials.[148, 154, 167] This treatment removes portions of the polymer from the surface, creating a rough, single-feature surface. For example, after spray-coating CNT/TPE/cyclohexane onto a substrate and drying, the sample is treated with ethanol for over 2 minutes to dissolve the TPE, forming a network with pit-like features. This increased roughness induces superhydrophobicity.[154]

Another example involves brushing an excess amount of CBNPs onto the surface of uncured PDMS. The sample is then cured at 100 °C for 10 minutes, allowing the CBNPs to cross-link and penetrate the PDMS, encapsulating the outer CBNPs (**Figure 6C-i**).[148] The evaporated PDMS

molecules result in a denser, rougher surface morphology than pure PDMS, enabling a contact angle greater than 150° and a sliding angle below 10°. This performance is maintained under contact with various liquid droplets and when stretched up to 200% strain (**Figure 6C-ii**). However, the superhydrophobic surface does not withstand severe abrasion. The modified material was applied to strain sensors, which exhibited a response to water impact with a change in resistance of less than 3% (**Figure 6C-iii**). The sensors responded to water ripples and ultrasonic oscillation, and their electrical resistance recovered after contact. The authors attributed this to the material's high sensitivity (GF = 101.75) and low detection limit. Superwettability and stability were further tested via tensile testing after 5 days of water immersion. However, there was little information on conductivity stability during static liquid interaction or under humid conditions, as small water molecules are still expected to have some impact. Further testing and investigation are needed to confirm the effectiveness of this approach.

It is also worth noting that in this process, CBNPs are embedded into the polymer without mixing the nanomaterials and polymers. The base polymers are swollen to a certain level of stickiness, allowing the nanomaterials to embed effectively.[164, 169] CBNPs are particularly suited for this process compared to alternative carbon nanofillers like one-dimensional CNTs or two-dimensional graphite nanosheets. Their zero-dimensional structure, with significantly smaller size, makes them easier to adhere to the polymer surface.[164, 170]

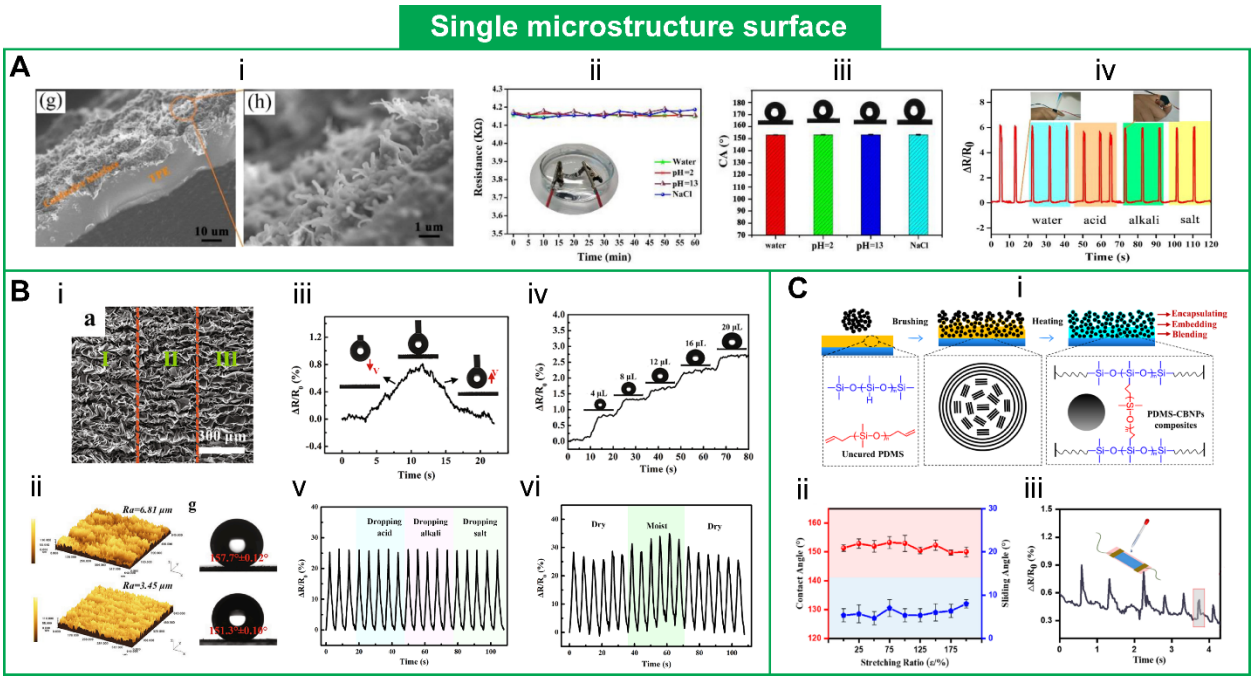

Figure 6. Single microstructure surfaces for humidity or liquid contact-insensitive piezoresistive sensors.
(A-i) Cross-sectional SEM images of a TPE/MWCNTs/PDMS film showing microstructure surface. (A-ii) and (A-iii) Conductivity stability tests in water, acidic (pH = 2), alkaline (pH = 13), and salt solutions, and contact angle measurements after immersion in various solutions for 7 days and. (A-v) Stable signal response under bending, tested with different solutions. Reprinted with permission from ref [48]. Copyright 2021 Elsevier.
(B-i) SEM morphology images of PDMS/rGO gradient wrinkle (PRGW) strain sensors with three different regions. (B-ii) LSCM profile and Ra measurements in regions I and III of the PRGW strain sensor, with corresponding water contact angles. (B-iii) and (B-iv) Impact of water droplets on electrical resistance of the PRGW. (B-v) Consistent electrical response under various liquid contacts. (B-vi) Unstable dynamic response in moist environment. Reprinted with permission from ref [51]. Copyright 2021 Elsevier.
(C-i) Schematic of the preparation of SS/PDMS-CBNP strain sensors (SS: silicone rubber sheet). (C-ii) Small changes in water contact angle and sliding angle with increased stretching ratio. (C-iii) Minimal impact of water droplets on the electrical resistance of the sensor. Reprinted with permission from ref [148]. Copyright 2024 American Chemical Society.

Hierarchical Surface

A hierarchical surface features smaller-scale structures layered atop larger ones, a design often found in nature, such as on lotus leaves. This type of surface provides several advantages: a high apparent receding contact angle (superhydrophobicity), low droplet adhesion and penetration,

and reduced droplet contact time.[161] Unlike single microstructure surfaces, which tend to have poor mechanical resistance [29, 164], hierarchical surfaces can enhance mechanical robustness without sacrificing anti-wetting or electrical performance.[151, 161, 169] As a result, significant attention has been given to fabricating hierarchical structures. Various approaches include laser irradiation of silicone surfaces [150], coatings combined with pre-strain [55, 155, 167], swell absorption on microstructures [169], and post-abrasion techniques.[151] These methods generally involve forming primary microstructures, which are then integrated with micro/nano features to create the hierarchical structure.

For example, a primary rough surface can be post-abraded to form a hierarchical structure with enhanced superhydrophobicity. A mixture of MWCNTs and RTV (vulcanized silicone rubber) was cured in a hand-folded paper box mold to generate the initial roughness of the composite. The sample was then rubbed with sandpaper to further increase roughness, raising the contact angle from over 100° to more than 150° (**Figure 7A-i** and **7A-ii**).[151] The rubbing direction had little effect on surface wettability. The superhydrophobic properties were retained under various chemical conditions (soaked in solutions with pH 1–13 for 12 hours and 90% humidity for 80 hours) and mechanical conditions (strain, bending, and abrasion). The surface's mechanical robustness was attributed to the elastic material's low surface energy and the enhanced microstructure from abrasion. This modified material was applied to strain sensors, and its electrical properties were tested under dynamic strain (0-50%) and liquid contact (water, acid, alkali, artificial sweat). The untreated sample showed significant resistance changes, whereas the treated one exhibited stable performance, as the low water adhesion allowed droplets to roll off quickly (**Figure 7A-iii** and **7A-iv**). Moreover, the hierarchical structure not only repelled liquids

but also improved strain sensitivity, attributed to the redistribution of strain on the surface (**Figure 7A-v**).

Another example of a hierarchical surface is achieved by combining multiple material coatings with pre-strain methods. First, APTES and MWCNT/graphene suspensions were sequentially spray-coated onto a pre-stretched PDMS substrate. After annealing and releasing the sample, silver nanoparticles were applied, followed by a final FAS spray coating, creating the FAMG strain sensor.[55] The nanomaterials on the wrinkled surface formed a hierarchical structure, while the low surface energy of the protective coating enabled a superhydrophobic surface. For comparison, the flat MWCNT/graphene-coated PDMS (**Figure 7B-i**) showed hydrophobic properties with contact angles between 102° and 121° when exposed to different liquids. However, under strain, the contact angle decreased (to 58° at 170% strain) due to water droplets in the *Wenzel state* penetrating the cracks, which negatively affected sensing performance (**Figure 7B-ii**). In contrast, the FAMG sensor retained superhydrophobic properties with a high contact angle (CA > 150°) and a low sliding angle (SA < 5°) under various liquid exposures, leading to more stable sensing performance (**Figure 7B-iii** to **7B-v**). The *Cassie–Baxter state* was maintained under strain, as cracks formed, increasing roughness and supporting an air layer that hindered water from contacting conductive paths (**Figure 7B-vi**). Consequently, the sensor demonstrated stable sensitivity (GF up to 2000 at 170% strain) under both static and dynamic conditions. Notably, APTES served as a bonding agent between the conductive layers, allowing slippage and terminal fracture of intermediate layers (APTES/MWCNT/G), which contributed to high sensitivity across a wide range of strains.

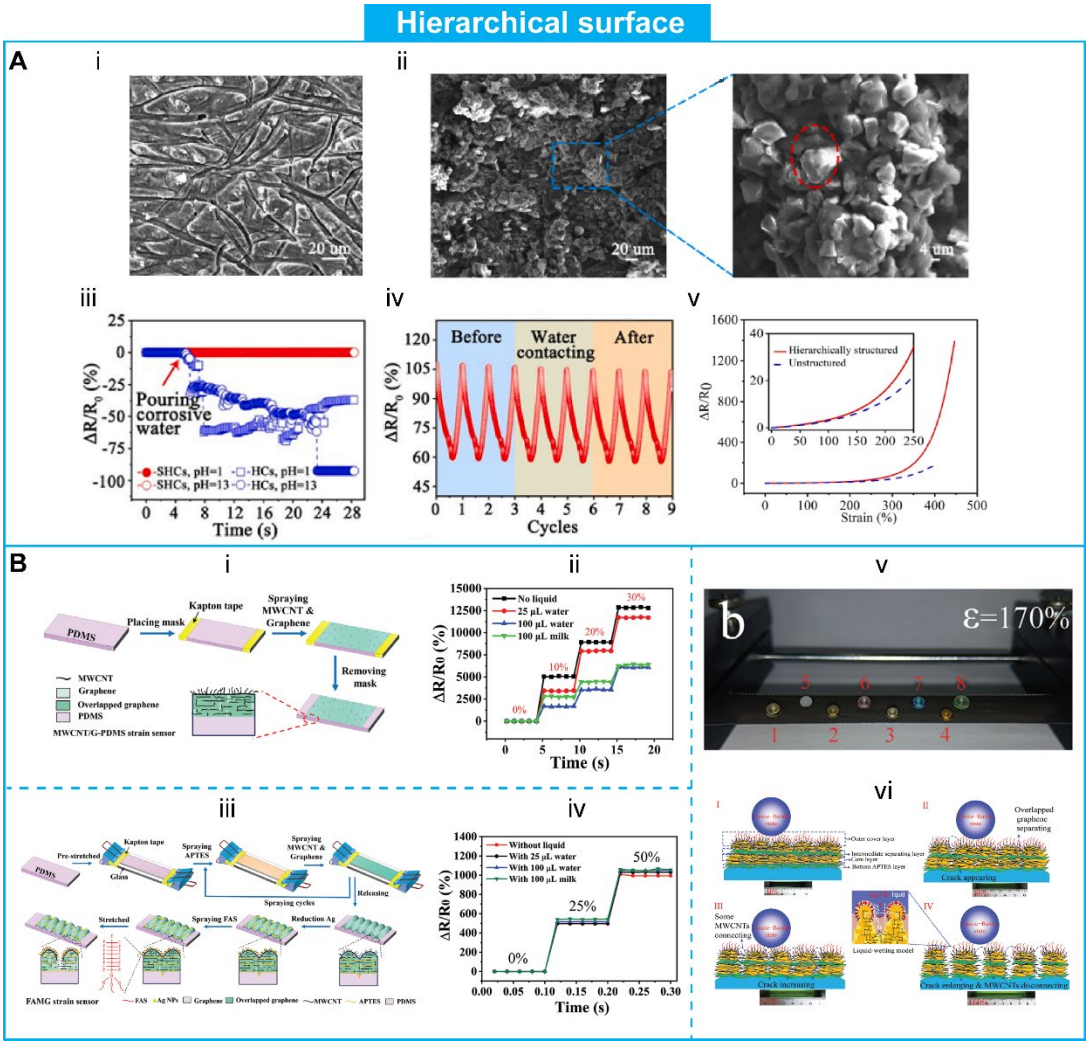

Figure 7. Hierarchical surfaces for piezoresistive sensors insensitive to humidity or liquid contact. (A-i) and (A-ii) SEM images of MWCNT/RTV sensing (MRS) material before and after the sanding (superhydrophobic) process, respectively. (A-iii) Stable resistance of superhydrophobic MRS materials under static conditions when exposed to different corrosive liquids compared to the unabraded one. (A-iv) Dynamic response of the superhydrophobic MRS sensor before, during, and after water droplets were applied. (A-v) Potential improvement in sensing performance with hierarchical structure (red solid line) compared to unstructured surfaces (blue dashed line). Reprinted with permission from ref [151]. Copyright 2021 Elsevier.

(B-i) Illustration of the fabrication of liquid-interfering MWCNT/G-PDMS strain sensor with (B-ii) unstable performance. (B-iii) Illustration of the fabrication of fluorinated micro/nanostructured hierarchical architecture F/Ag/MWCNG/G-PDMS (FAMG) strain sensor, showing (B-iv) stable performance even with liquid contact under different strain conditions. (B-v) Optical photograph of eight 100 μL liquid droplets on FAMG sensors stretched to 170% strain. (B-vi) Schematic of how liquid interference is prevented during strain sensing in the FAMG strain

sensor (I: 0% strain; II: 60% strain; III: 110% strain; IV: 160% strain). Reprinted with permission from ref [55]. Copyright 2020 John Wiley and Sons.

Superhydrophobic Porous Materials

Superhydrophobic porous materials combine permeability with liquid repellency, making them well-suited for skin-worn devices. The mechanism for achieving superhydrophobicity in these materials is similar to the previous categories. However, coating the entire porous structure without significantly affecting permeability or conductivity typically involves dip-coating techniques.[56, 149, 156, 157, 163, 165, 168, 171-177] Common porous substrates include sponges or fabrics (such as electrospun PU/TPU fibers, commercial fabrics, or papers) coated with conductive fillers (e.g., CNTs, graphene, rGO, MXene, PEDOT:PSS). These fillers not only serve as sensing materials but also enhance the roughness of the sample. Superhydrophobicity is achieved after coating the structure with low-surface-energy polymers or SiO_2 or TiO_2 nanoparticles. Adhesive materials (e.g., chitosan, methyl cellulose, PDA, or PDMS) may be applied before or after the conductive fillers to improve adhesion between the fillers and the substrate. PDMS can serve as a protective layer after curing [138, 156, 157], but other hydrophilic adhesives, like PDA or methyl cellulose, require additional coatings (typically fluoride- or non-fluoride-based) to achieve superhydrophobicity.[56, 149, 163, 168, 171, 172] Using only PDMS is effective, but incorporating an adhesive layer like PDA improves resistance to washing. For instance, Tianxue reported a superhydrophobic fabric coated with rGO and PDMS micro/nanoparticles.[138] While the fabric initially exhibited a contact angle above 150° and good permeability, 20 washing cycles reduced the contact angle and increased electrical resistance, indicating the peeling of the PDMS and rGO layers (**Figure 8A**). In contrast, using a PDA adhesive and a hydrophobic fumed silica (Hf-

SiO_2) protective layer resulted in stable electrical resistance and superhydrophobicity even after repeated washing cycles (**Figure 8B**).[56]

A more detailed coating process can be seen in the development of an e-textile based on a hierarchical "steels-concrete" composite structure from the Ling research group.[152] The base textile (PET) was coated with a CNT "steel" network and then layered with polymers "concrete" (polypyrrole-polydopamine-perfluorodecyltrlethoxysilane [PPy-PDA-PFDS]) via dip-coating to create a self-protective, reproducible e-textile (SPRET) (**Figure 8C-i**). The PFDS, containing fluorine, lowered surface energy, while the micro/nano structure enhanced roughness, making the SPRET textile superamphiphobic with contact angles above 150° for both water and oil (**Figure 8C-ii**). The mussel-inspired PDA played a key role in washing durability, improving adhesion between the conductive nanomaterials, textiles, and PFDS via chemical bonding (**Figure 8C-iii**). However, since PDA is hydrophilic, PFDS was required to make the material superhydrophobic.[166] Stacking the SPRET on Ni-coated interdigital textile electrodes resulted in a pressure sensor with breathability, ultra-sensitivity, and improved sensing compared to PET coated only with CNTs *(over 100 kPa^{-1} versus 35.7 kPa^{-1} in the 0-50 kPa range)* due to the initial lower conductivity. The sensor also demonstrated stability after three washing cycles and stable signal detection under sweaty conditions (**Figure 8C-iv**). However, the fluorine-rich PFDS raises concerns about its effect on the skin.

In contrast, oxide nanoparticles offer effective protection without the need for fluorine. Dong *et al.* introduced titanium dioxide-octadecyl isocyanate (TiO_2-ODI) nanoparticles, which are hydrophobic and fluoride-free, to coat conductive cotton fabrics (initially coated with PEDOT:PSS, polypyrrole, or MWCNTs).[173] The TiO_2-ODI nanoparticles' crystalline branched structure increased roughness, while the alkyl chains' low surface energy enhanced liquid

repellency (**Figure 8D-i**).[178] The coating process involved simply immersing the fabrics in a conductive solution and then in a TiO_2-ODI dispersion, aided by ultrasonication. The nanoscale size of the TiO_2 particles, combined with the dense TiO_2-ODI nanoparticles (with long ODI-grafted TiO_2), allowed them to easily penetrate the gaps between yarns and fibers, forming a protective layer around the cotton fibers coated with PEDOT:PSS. As a result, the TiO_2-ODI layer demonstrated hydrophobic characteristics, with contact angles ranging from 140.0° to 146.9° for deionized water, saline, milk, tea, and coffee, indicating nearly superhydrophobic performance. When applied to pressure sensors, the TiO_2-ODI layer helped maintain stable resistance (a 2.5% change) even at 95% relative humidity. The team also applied TiO_2-ODI nanoparticles to polyurethane foam substrates (coated with CNT/CB), creating a sensor resistant to temperature and humidity interference (**Figures 8D-ii** and **8D-iii)**. Adhesives such as (3-aminopropyl)triethoxysilane (KH550) and PDMS enhanced adhesion between the TiO_2-ODI, CNT, CB, and polyurethane, resulting in more stable performance and improved sensitivity (from 0.17 kPa^{-1} to 0.41 kPa^{-1}).[137]

While most methods use dip-coating or spray-coating, chemical vapor deposition (CVD) offers a one-step, solution-free alternative. S. Zohreh *et al.* used CVD to coat cotton balls and fabrics with PEDOT-Cl, followed by trichloro(1H,1H,2H,2H-perfluorooctyl)silane (TCPFS) as a protective layer against humidity and washing (**Figure 8E**).[179] This technique allows for variations in the fabric type, thickness, and number of layers, as well as control over the coating's thickness, making it possible to tune the sensor's sensitivity. However, the coated fabrics only exhibited hydrophobic properties (contact angle ~134.88°), indicating that PEDOT-Cl alone did not create enough surface roughness for superhydrophobicity.

Before proceeding to the next discussion, a practical question arises: how do you connect conductive wires to coated samples when the conductive materials are wrapped in nonconductive polymer? In the case of full encapsulation, connections are made prior to coating, but in other approaches, wires are usually attached after all coatings are applied. Thick insulating coatings or extended dopamine polymerization (for PDA) increase resistance.[164, 168] The conductivity also decreases when wires are connected to insulating layers.[163] To minimize these effects, the protective coating layer's thickness must be controlled during the dispersion step.[48] Otherwise, two small sections at the two ends of the coated samples can be cut away to expose the conductive path for wire connections.[177] Interestingly, insulating coatings can enhance sensor sensitivity (e.g., in pressure sensors) by increasing the initial resistance.[152]

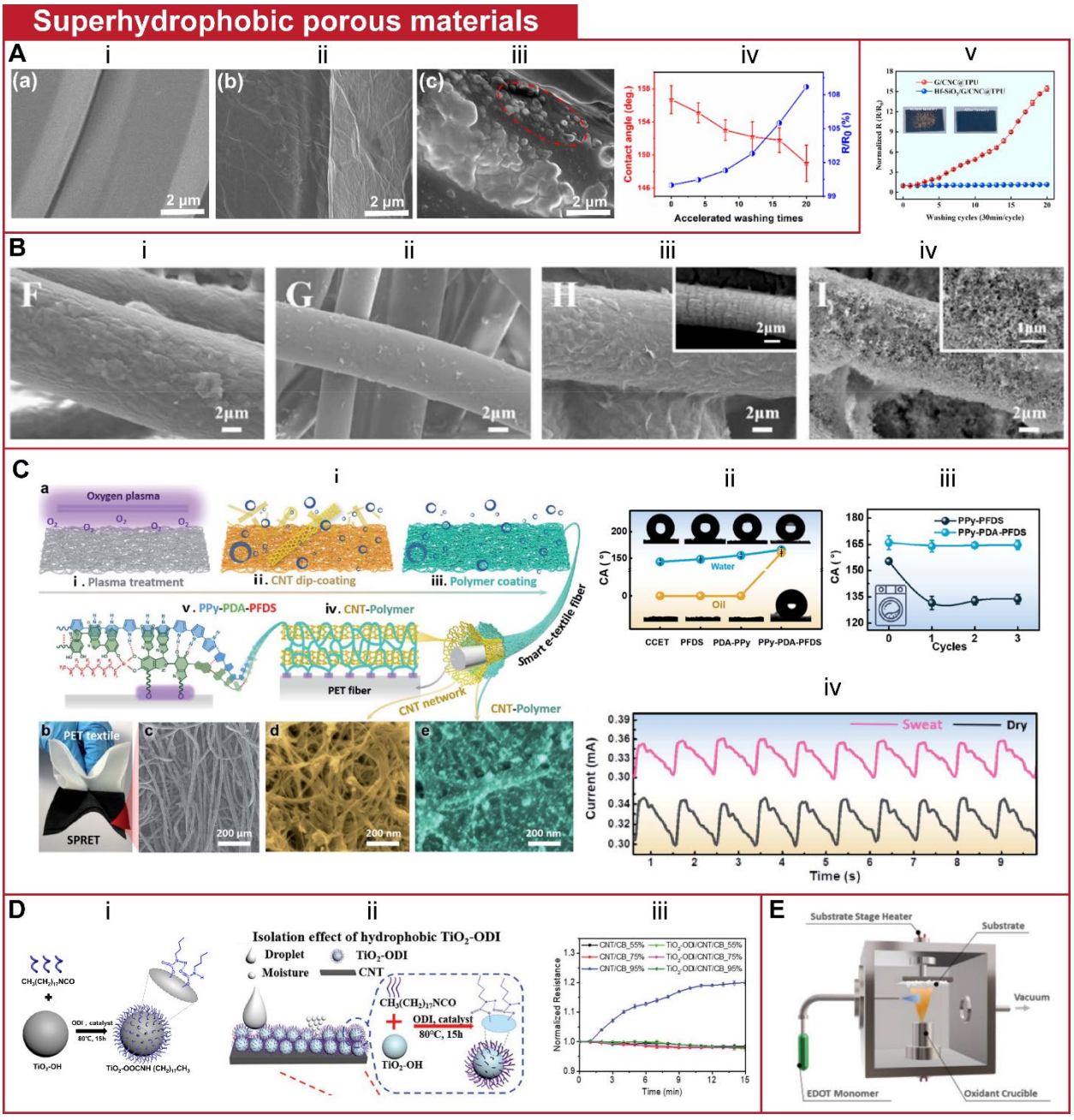

Figure 8. Superhydrophobic porous materials for humidity or liquid contact-insensitive piezoresistive sensors. (A-i) to (A-iii) SEM images of pristine fabric, GO@fabric, and PDMS-rGO@fabric, respectively. (A-iv) Contact angle measurements and resistance change after 20 cycles of accelerated washing. Reprinted with permission from ref [138]. Copyright 2022 American Chemical Society.

(B-i) to (B-iv) SEM images of original NWF, PDA@NWF, G/CNC/PDA@NWF, and Hf-SiO_2/G/CNC/PDA@NWF surfaces, respectively. (B-v) Resistance changes of the strain sensor with and without Hf-SiO_2, measured across repeated washing cycles. Reprinted with permission from ref [56]. Copyright 2019 Elsevier.

(C-i) The structure of self-protective and reproducible e-textile (SPRET). Images, from left to right, at the bottom include a photo of a PET textile and SPRET, a SEM image of SPRET, a SEM image of CNT network, and a SEM image of CNT-polymer composite. (C-ii) Superamphiphobicity of SPRET, with contact angles of about 160° for both water and oil. (C-iii) The remaining superhydrophobic surface of SPRET compared to a sample without PDA. (C-iv) Stable signals of wrist pulse in dry and sweaty conditions. Reprinted with permission from ref [152]. Copyright 2019 The Royal Society of Chemistry.
(D-i) Schematic of octadecyl chains grafted to TiO_2 nanoparticles. Reprinted with permission from ref [178] Copyright 2018 Elsevier. (D-ii) Schematic showing anti-interference properties of TiO_2-ODI protector against droplets and humidity. (D-iii) Comparison of electrical resistance changes of pressure sensors with and without TiO_2-ODI protection, where the protected sensor shows stable resistance. Reprinted with permission under a Creative Commons CC BY 4.0 License from ref [137]. Copyright 2023 John Wiley and Sons.
(E-i) Schematic of the custom-de chamber utilized for oxidative chemical vapor deposition (oCVD). Reprinted with permission from ref [179]. Copyright 2023 John Wiley and Sons.

Chemical Treatment

Apart from coating methods, the creation of chemical bonds between conductive materials helps alleviate the effect of water on conductivity. Regarding PEDOT:PPS as conductive materials, their chemical structure can be modified to withstand humidity without the need for coating. Similar to the method used to achieve temperature insensitivity, 5% DMSO was added to the PEDOT:PSS solution, followed by spin-coating and drying on a PET substrate. Minimal changes in the electrical resistance of the modified film under humid conditions (RH = 11–98%) were observed (**Figure 9A-i**). The explanation is as follows: without DMSO, when H_2O diffuses into PEDOT:PSS films, the formation of $H_3O^+PSS(SO_3)^-$ causes film swelling, which increases the distance between conductive PEDOT-rich domains, consequently reducing charge carrier mobility and conductivity. When PEDOT:PSS is doped with DMSO, the polar DMSO interacts with both positively charged PEDOT and negatively charged PSS chains, causing a charge screening effect that weakens the Coulombic interactions between the PEDOT and PSS chains.

This dissociation promotes the fusion of PEDOT-rich areas, forming larger PEDOT-rich domains that minimize the effect of swelling on the overall conductivity of the PEDOT:PSS composite film (**Figure 9A-ii**).[180]

Furthermore, Xu *et al.* demonstrated a "bottom encapsulating-top sealing" strategy to seal the Ag NWs conductive network using hydrocellulose as a bottom layer and PEDOT:PSS as a top layer (CRC film).[37] Ag NWs and PEDOT:PSS were mixed and transferred to a filter device with hydrocellulose as the filter, followed by a drying process. The Ag NWs adhered directly to the hydrocellulose due to its abundant hydroxyl groups. During the drying process, water molecules gradually detached from cellulose's hydrogen bonds, allowing the formation of a coordination complex (Ag←:O) between cellulose and Ag NWs, while also enabling hydrogen bonding with PEDOT:PSS components. As a result, the Ag NWs conductive network was sandwiched between the cellulose substrate and the PEDOT:PSS cover, enhancing both antioxidant properties and the stability of conductivity (**Figure 9B-i**). Without PEDOT:PSS, severe oxidation of Ag Nws caused the destruction of the conductive network, leading to a sharp decrease in conductivity (**Figure 9B-ii** to **9B-iv**). Two pieces of CRC film were assembled with a middle cellulose film to form a pressure sensor with a sensitivity of 23.35 kPa^{-1} (within 400 Pa). It is worth noting that the authors did not test the conductivity of PEDOT:PSS deposited solely on hydrocellulose under humid conditions. However, it is expected that the hydrogen bonding between PEDOT:PSS and cellulose could minimize the influence of humidity on PEDOT:PSS.

Additionally, the family of graphene materials can be used for water resistance. As previously mentioned, perfect free-standing graphene sheets are insensitive to water molecules.[142] A pressure sensor based on graphene-coated PDMD micropyramids exhibited stable sensing performance under humid conditions ranging from 30% to 90%.[85] Graphene oxide (GO) behaves

similarly. After the reduction process, which eliminates oxygen-related functional groups to minimize water adsorption, rGO-coated yarn showed only slight changes in resistance in environments with 39% to 71% humidity.[47]

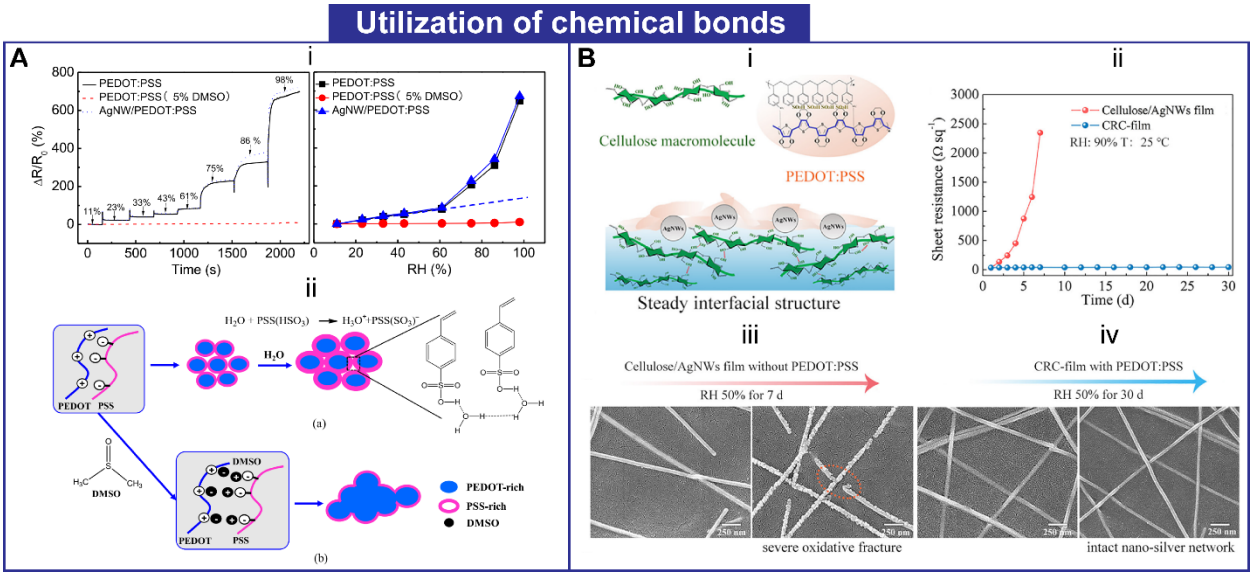

Figure 9. Chemical bonding methods for piezoresistive sensors insensitive to humidity or liquid contact. (A-i) Stable electrical resistance of PEDOT:PSS doped with DMSO under a wide range of humidity conditions. (A-ii) Illustration of DMSO's ability to dissociate PEDOT and PSS, promoting the connection between PEDOT chains to form PEDOT-rich domains. Reprinted with permission from ref [180]. Copyright 2018 Elsevier. (B-i) Schematic of chemical crosslinking within conductive regenerated cellulose-based films (CRC-film). (B-ii) Stable electrical resistance of CRC-film at 90% RH over 30 days. (B-iii) and (B-iv) SEM morphology of cellulose/Ag NW films without PEDOT:PSS after 7 days in 50% RH and CRC-film (with PEDOT:PSS) after 30 days in 50% RH, respectively. Reprinted with permission from ref [37]. Copyright 2020 Elsevier.

Humidity-Insensitive Electromechanical Sensors Based on Capacitive and Triboelectric Effects

Humidity or liquid contact can induce changes in the dielectric properties of materials used in capacitive sensors and distort the ability of triboelectric materials to store electrons. It is

necessary to summarize studies on how to protect these sensors from environmental interference to ensure stable sensing performance.

Capacitive Sensors Insensitive to Humidity by Full Encapsulation

To protect the sensing components, capacitive sensors have been fully encapsulated.[107, 181] Both parallel and planar capacitive pressure sensors typically use polymers as the dielectric layer, whose dielectric constant is affected by humidity due to the high dipole moments of water molecules (hence, capacitive techniques are often used for humidity sensors).[182] Since the conductive electrodes are usually secured on flexible substrates, using hydrophobic flexible substrates offers an effective and straightforward way to protect the sensors. For example, Haobin *et al.* utilized laser-induced graphene (LIG) electrodes by engraving flexible PI substrates.[183] They employed Ecoflex as both a spacer layer (1.4 mm thick for optimal sensing performance) and an encapsulation layer. Owing to complete encapsulation, the sensor maintained stable performance under varying humidity (RH from 53.5% to 80%) **(Figure 10A)**. Additionally, the planar capacitive pressure sensor with an all-nanofiber platform and temperature insensitivity also demonstrated stable sensing performance in humidity up to 90% RH and under water (**Figure 10B**).[107] This stability resulted from the full encapsulation provided by hydrophobic TPU nanofiber mats on the top and bottom of the sensor, with additional sealing at the edges using TPU liners.

Triboelectric Sensors Insensitive to Humidity

For sensors based on the triboelectric effect (such as TENG-based pressure sensors), humidity has a significant impact on output performance. Previous studies using various pairs of triboelectric materials (e.g., PDMS vs. aluminum, PTFE vs. conductive glass) have shown that at

high relative humidity (RH), the output performance degrades due to the formation of a thick water layer that discharges the contacted surfaces.[28, 184] In contrast, when starch-based materials (such as wheat starch or gelatin) or PVA are used, output performance improves at high RH.[185-187] This improvement is attributed to the abundant hydroxyl groups in these materials, which fix water molecules via hydrogen bonds, creating a more tribo-positive surface polarity. However, while an increase in output performance can be advantageous for applications like power generation, it is undesirable for sensors. Therefore, several strategies have been employed to minimize the effects of humidity, including encapsulation, superhydrophobic surfaces, and material selection.

The first approach involves encapsulating the working components of TENG with waterproof materials.[188, 189] For instance, Arunkumar *et al.* reported a TENG based on Ni foam and PDMS as the triboelectric material pair, which was encapsulated by PET sheets on both sides and sealed at the edges using a pouch laminator.[190] This encapsulation prevented water penetration, allowing the sensor to maintain stable output performance at high RH (up to 90%) and even after 24 hours of submersion in water, compared to unpackaged sensors. Similarly, Jae *et al*. encapsulated a multilayered TENG (M-TENG), operating in single-electrode mode, within Ecoflex.[191] The sensor demonstrated stable performance under humid conditions (**Figures 10C-i** and **10C-ii**). In addition to humidity protection, this sensor exhibited high output performance and a high sensitivity of 149 V/kPa at pressures below 14 kPa (**Figure 10C-iii**). This high performance resulted from surface modification and the optimized combination of dielectric, porous, and conductive materials. For example, the porous zirconium metal-organic framework (MOF-525) and cobalt nanoporous carbon (Co-NPC) enhanced charge trapping on the surface,

while MXene facilitated charge transfer to the charge-trapping layer and reduced charge diffusion due to its high conductivity and functional groups (**Figure 10C-iv**).

The second approach to counter humidity effects is creating a superhydrophobic contact surface to prevent the formation of a water layer. This can be achieved through physical modifications (such as a 3D structured surface) [36] or chemical modifications (by applying hydrophobic chemical groups to the surface).[192] Although these methods reduce humidity effects, some degradation in performance is still observed (**Figures 10D** and **10E**).

The third approach is material selection, which enables stable TENG sensor output despite humidity. For example, a metal-organic framework (MOF) known as HKUST-1 ($Cu_3(BTC)_2$, where BTC = 1,3,5-benzenetricarboxylate or trimesate) was investigated as a triboelectric material by mixing it with PDMS in different ratios.[193] Results indicated that 3 wt% of HKUST-1 allowed TENG to perform unaffected in humid environments (RH from 10% to 90%). The authors explained that HKUST-1's high capability to capture surface triboelectric electrons within its friction layer contributed to this stability. As RH increased, more water molecules were absorbed in the pores of HKUST-1, enhancing charge trapping. This internal electron accumulation balanced the dissipation of surface electrons on the PDMS surface, thereby stabilizing TENG output performance as RH increased (**Figure 10F**). Another example comes from Zong-Hong *et al.*, who used a mixture of glycerol and chitosan as a triboelectric material.[194] The thin, nanostructured chitosan-glycerol film acted as both a triboelectric and conductive material. The triboelectric charge density of the film decreased with increasing RH, while its conductivity increased with rising humidity. The interaction between these two mechanisms resulted in stable output performance of the chitosan-glycerol-based TENG across a humidity range from 20% to 80% (**Figure 10G**).

Capacitive pressure sensors insenstive to humidity (full encapsulation)

Parallel capacitor

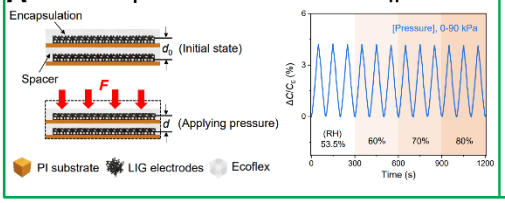

Planar capacitor

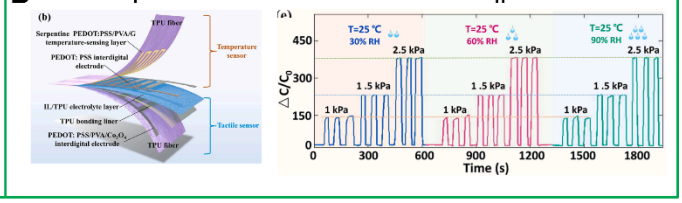

Triboelectric pressure sensors insenstive to humidity

Encapsulation

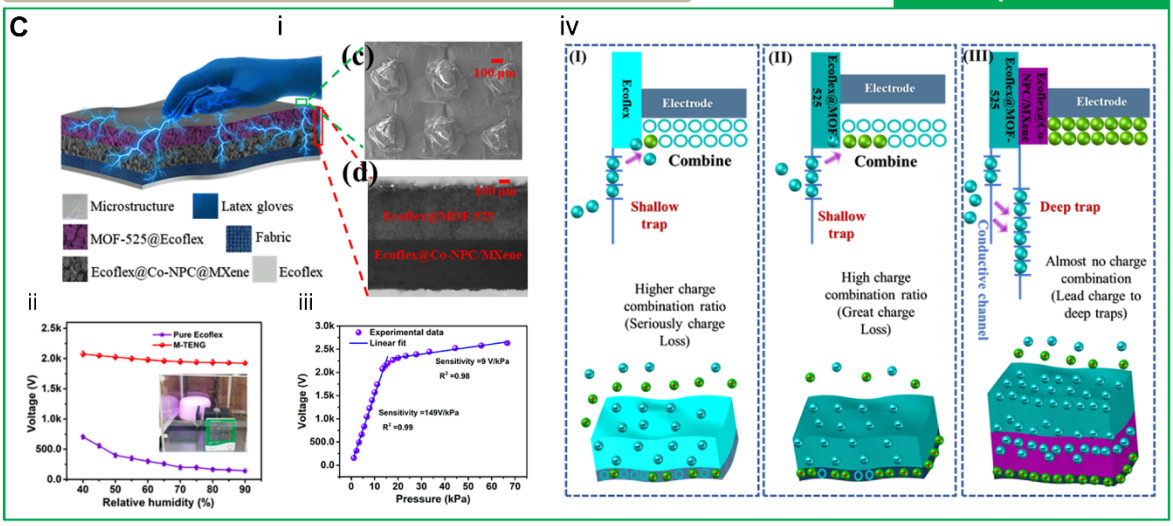

Superhydrophobic surface

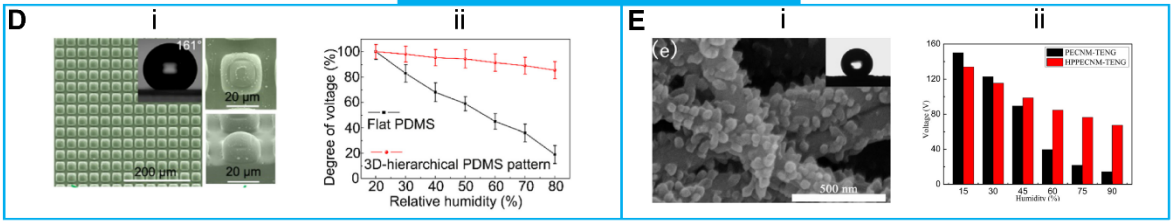

Material combination

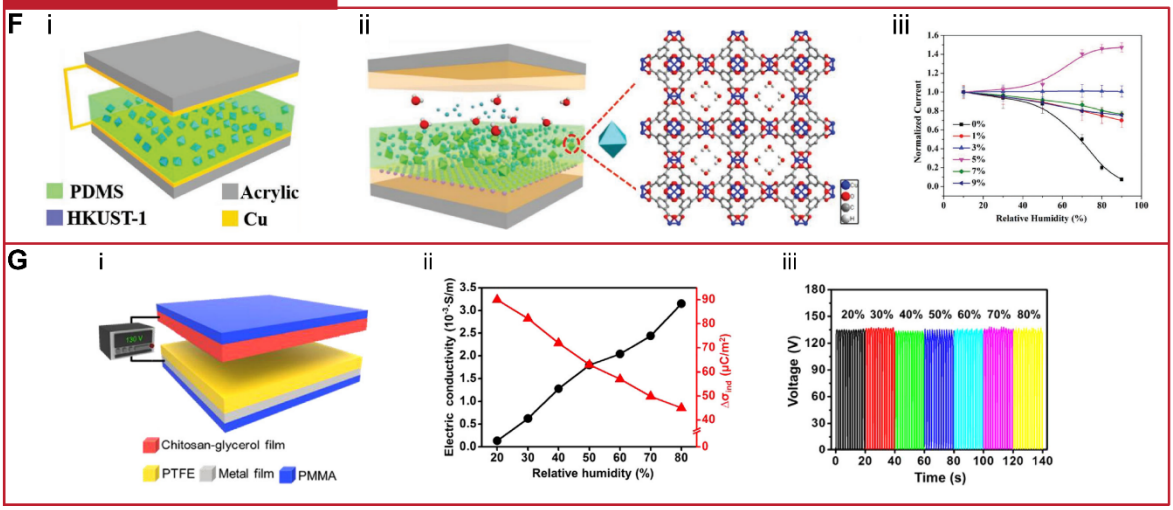

Figure 10. Methods for fabricating capacitive and triboelectric pressure sensors insensitive to humidity.
(A-i) Structural schematic of a parallel capacitive pressure sensor fully encapsulated by PI substrates and Ecoflex layers. (A-ii) Stable sensor performance in environments with 53.5% to 80% humidity. Reprinted with permission from ref [183]. Copyright 2022 American Chemical Society.
(B-i) Schematic of a fully TPU-encapsulated planar capacitive pressure sensor (bottom). (B-ii) Stable sensor performance in humidity levels from 30% to 90%. Reprinted with permission from ref [107]. Copyright 2023 Elsevier.
(C-i) Schematic of a multilayered TENG (M-TENG) (left), FE-SEM image of 3D-printed microstructures (top, right) and cross-sectional views of the M-TENG (bottom, right). (C-ii) Comparison of output voltage between pure Ecoflex and M-TENG at different relative humidity levels. (C-iii) High sensor performance of M-TENG. (C-iv) Charge trapping mechanisms in the Ecoflex layer, Ecoflex@MOF-525 layer, and double-layer TENG. Reprinted with permission from ref [191]. Copyright 2022 Elsevier.
(D-i) Image of 3D hierarchical PDMS interlayer. (D-ii) Comparison of output voltage from TENGs with flat PDMS and 3D hierarchical PDMS interlayers under humidity. Reprinted with permission from ref [36]. Copyright 2019 Elsevier.
(E-i) FE-SEM image of the surface of HMDS/PEG/PANI/EVOH composite nanofiber membranes, with inserts showing the water contact angles (141°). The HMDS reacts chemically with PEG, forming hydrophobic ends on the surface. (E-ii) The HMDS/PEG/PANI/EVOH (HPPECNMs) exhibit a smaller effect of humidity on the open-circuit voltage compared to PANI/EVOH (PECNMs) membranes without protective layers. Reprinted with permission from ref [192]. Copyright 2018 Elsevier
(F-i) Schematic of TENG based on PDMS/HKUST-1 nanocomposite film. (F-ii) Schematic of triboelectric charge transport in the PDMS/HKUST-1 nanocomposite layer when water molecules are absorbed on the PDMS surface and within the HKUST-1 nanochannels. The enlarged view shows the HKUST-1 framework along the [100] direction, revealing the pore structure covered with water molecules. (F-iii) The current output of the TENG-based PDMS/HKUST-1 nanocomposite (with 3% HKUST-1) remains unaffected by changes in relative humidity. Reprinted with permission from ref [193]. Copyright 2019 John Wiley and Sons.
(G-i) Schematic structure of a chitosan-based TENG (C-TENG). (G-ii) Triboelectric charge density and electrical conductivity of chitosan-glycerol film measured under varying humidity. (G-iii) Stable output voltage of C-TENG across a humidity range of 20% to 80%. Reprinted with permission from ref [194]. Copyright 2018 Elsevier.

The aforementioned approaches enhance the stability of flexible electromechanical sensors under varying humidity and liquid exposure, enabling reliable sensing performance in practical uses. The liquid-repellent soft strain and pressure sensors were attached on different potions on human body to monitor biophysical signals (e.g., pulse arteries, joint motion, or facial muscle). The

comparison between dry state, sweat state, corrosive liquid dropping, and underwater indicated little environmental interference to the sensing performance.[48, 152, 163, 169, 173, 179] Bacterial droplets also did not cause interference to the sensing behavior even though they always stayed on the sensor surface.[55] These demonstrations are greatly promising for human health monitoring system in terms of cleansing and stable biophysical detection. The capability to detect motions under water enables water sports management as well as drowning alarming.[138, 148] Stable detection of grip objects and accurate human-machine interaction (e.g., controlling robot hand) were also demonstrated in humid conditions and under liquids,[137, 145, 152] further proving the usefulness of insensitivity to humidity and liquid contact.

Materials Engineering and Structural Designs for Insensitivity to Off-Axis Deformations

For soft electromechanical sensors applied in biophysical signal detection,[59] soft robotics,[40] and human-machine interaction,[195] their accuracy is crucial for providing reliable signals for further processing. Since these devices conformally contact with the surface of human bodies and soft robots, the dynamic movement can induce arbitrary surface deformations, causing stress or strain to the sensors.[39, 43] Some complex moving surfaces, for example, are human hand, wrist, neck, or robot joints where multiple parts are connected.[43, 196] External forces, such as tactility or unintended compression, also contribute another stress to the devices.[197, 198] These stress or strain can be in various directions, including both desired and undesired directions. While ones from desired directions provide valuable information, those from undesired directions can introduce interference. Soft strain and pressure sensors are typically designed to measure stress or strain along specific, intended axes to capture useful signals. However, those from undesired directions

cause off-axis deformations in the sensors, leading to errors and reduced accuracy in sensor readings.

The development of electromechanical sensors that are insensitive to off-axis deformations can effectively address these accuracy issues. By minimizing sensitivity to off-axis forces or strains, error signals are reduced, allowing for more accurate detection of targeted forces or strains. Achieving off-axis insensitivity relies on two main strategies: materials engineering and structural design. Materials engineering, such as the use of electrospun fibers, can effectively mitigate interference induced by bending or off-axis strain, types of off-axis deformation.[43, 57] However, this approach is limited to certain fabrication facilities and materials. In contrast, structural design innovations offer greater flexibility that accommodates a wider range of materials (e.g., metals, nanomaterials, and thicker insulating matrices) and adaptable fabrication techniques like molding, cutting, printing.[44, 196, 199] These designs can effectively suppress interference from off-axis strain, torsion, or pressure. Nevertheless, the sensor size is usually large to accommodate the designs, which can be inefficient for multiple sensor integration. A detailed exploration of these approaches provides opportunities to combine material-specific properties with versatile design strategies, leading to compact specific sensors. This section delves into these approaches, particularly as applied to pressure and strain sensors, highlighting how each method contributes to off-axis insensitivity.

Pressure Sensors Insensitive to Off-Axis Mechanical Deformations

Pressure sensors are designed to detect force or pressure in the direction perpendicular to the sensor's surface (out-of-plane pressure). When soft pressure sensors are applied on soft tissue (e.g., soft robotics or human skin) for either tactile detection or physiological monitoring, robot

or body motions can induce dynamic tissue deformations that cause strains to the sensors.[39, 200] These perturbed strains are commonly in the form of bending or stretching, which can disrupt active conductive materials or interfere with pressure-induced signals.[40, 195, 201] The result is poorer sensing performance or inaccurate signal detection. Therefore, it is highly desirable to investigate approaches that can minimize these perturbed strains.

The key to mitigating this interference is maintaining the same or similar working area and working distance under off-axis deformations. Piezoresistive pressure sensors typically operate by increasing the contact area under pressure, but strain can also induce changes in this area. Additionally, pressure sensors often feature microstructured or textured surfaces that create gaps between active components.[104, 202] When considering the sensor as a bulk, soft material, the Poisson effect can cause the distance between two electrodes to decrease, narrowing the gap and increasing the working area. Moreover, during strain, piezoresistive pressure sensors must ensure stable electrical resistance of both the sensing components and the electrical conductance connected to external circuits. To address this, some approaches, such as wrinkle surfaces applied to the electrical conductance, have been adopted. Similarly, pressure sensors based on triboelectric effects and changes in capacitance also depend on the working area and distance between electrodes. However, as these effects are less affected by external resistance, maintaining stable electrical resistance in the conductive paths to external circuits is less critical. Based on this analysis, materials engineering, and innovative structural designs have been demonstrated to maintain stable working areas and distances under off-axis deformations. Materials engineering, such as electrospun fibers, is particularly effective in reducing the impact of bending, while structural designs, such as incorporation of stiff islands, mitigate the influence of strain.

Materials Engineering for Pressure Sensors Insensitive to Bending Deformations

To achieve insensitivity to bending, it is essential to maintain stable working areas and distances by suppressing bending-induced strains. Bending deformations exert small tensile strain on the outer surface and small compressive strain on the inner surface of pressure sensors. According to the formula for strain (ε), which is related to the distance offset from the neutral line (y) and the bending radius (R), $\varepsilon = y/2R$, the strain is directly proportional to the position of the active element relative to the neutral line. Reducing the sensor's thickness decreases this offset distance, thereby reducing the strain exerted on the sensor. As a result, reducing the overall sensor thickness (ultrathin sensors) is a widely adopted strategy.

The electrospinning method is particularly suitable for fabricating ultrathin fibrous and porous films (ranging from nanometers to several micrometers). A study by the Takao research group demonstrated a transparent, bending-insensitive pressure sensor based on electrospun nanofibers (a combination of elastomer, CNT, and graphene) with a thickness of ~2 μm. These nanofibers were sandwiched between 40-nm-thick Au electrodes coated on substrates of varying thicknesses (75 μm to 1.4 μm, made of PI and PET).[57]

In addition to the ultrathin layer, two structural features of the material helped lessen bending-induced strain. First, the fibrous structure accommodated strain by rotating and deflecting the fibers (changing alignment) instead of stretching them individually, resulting in 70% less strain compared to a continuous material (**Figure 11A-i**). Second, the stiffness of the electrodes played a role: thicker, stiffer electrodes induced shear in the fibrous sensing layer, making it more sensitive to bending, whereas thinner, more compliant electrodes followed the deformation of the

sensing layer, improving bending insensitivity (**Figure 11A-ii**). As a result, the sensor maintained stable performance at a bending radius as small as 80 μm (**Figure 11A -iii)**.

In addition to bending insensitivity, the combination of CNTs (0.017%) and graphene (1.7%) significantly improved sensitivity. Pure graphene exhibited high resistance, even under high pressure, but the addition of a small amount of CNTs provided additional conductive paths between graphene sheets, greatly enhancing conductivity under small pressures.

Beyond the fibrous CNT/graphene sensor, the research team also developed an all-nanofiber mechanoacoustic sensor using PVDF nanofibers sandwiched between Au-coated PU nanofiber electrodes. This sensor achieved a sensitivity of 10,050.6 mV Pa^{-1}, thanks to a combination of piezoelectric and triboelectric effects, with triboelectricity being the dominant factor. Although the nanofiber sheets were ~2.5 μm thick, air gaps ranging from 5 to 15 μm naturally formed due to the porous structure, increasing the overall sensor thickness. This sensor demonstrated stable output voltage down to a bending radius of 6.5 mm.[203]

Another example is a piezoresistive pressure sensor based on carbon flowers mixed with SEBS elastomer, which maintained stable performance at a bending radius of 5.5 mm (**Figure 11B-i** to **11B-iii**).[204] This was achieved by reducing the thickness of the sensing composite layer to 13 μm. The sensing mechanism was based on contact between the top electrode and the rough surface of the sensing composite, meaning that bending-induced deformations in the bulk of the composite had minimal effect. This contact mechanism also provided high sensitivity (2×10^5 kPa^{-1}) and insensitivity to thickness, enabling large-area printing fabrication.

In contrast to ultrathin sensors, Seunghwan *et al.* developed 3 mm-thick, porous pressure sensors by coating CNTs onto the surface of pores in PDMS (via dipping and squeezing the porous

PDMS in CNT dispersion).[200] These sensors demonstrated bending insensitivity down to a bending radius of 7.5 mm, with a resistance change of less than 5%. Simulation results suggested a similar explanation to that for electrospun nanofibers: the microporous configuration accommodated bending deformation by changing its overall arrangement, with minimal strain on individual micropores and PDMS bridges (local strain < 10% at a bending radius of 5 mm), resulting in stable electrical performance (**Figure 11C**).[57]

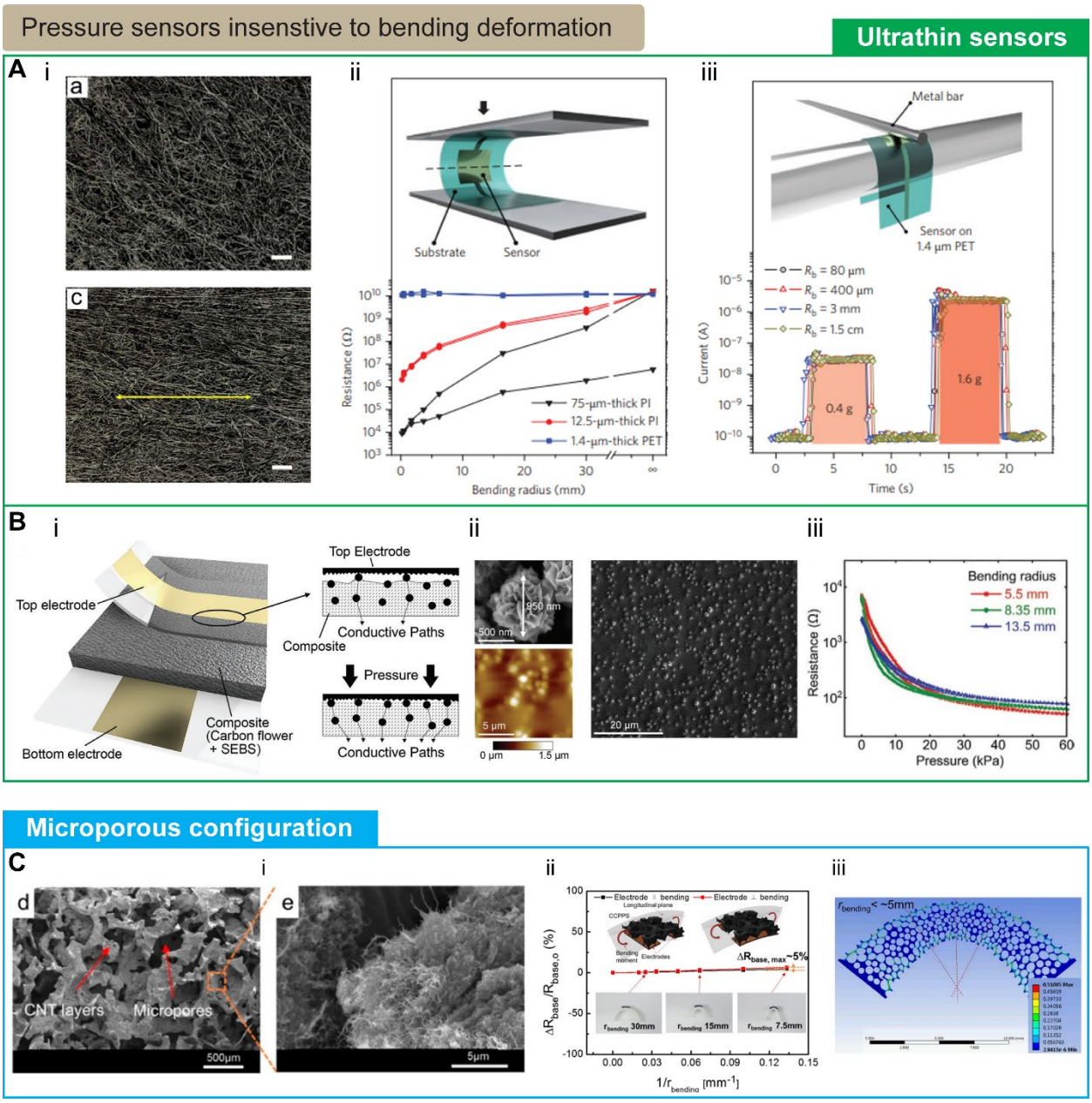

Figure 11. Methods to achieve pressure sensors insensitive to bending deformations.

(A-i) Microscope images of an electrospun fiber layer (top) and the fiber layer under 30% tensile strain (bottom). Scale bars represent 20 μm. The nanofibers realign to reduce strain caused by tensile stress. (A-ii) Resistance response of the fiber layer to different bending radii, depending on substrate thickness. A PET substrate with a thickness of 1.4 μm showed stable resistance. (A-iii) Stable pressure sensor performance on 1.4-μm-thick PET under two applied normal forces and various bending radii (down to 80 μm). Reprinted with permission from ref [57]. Copyright 2016 Springer Nature.

(B-i) Device structure of a flexible, printed pressure sensor using a composite of carbon flower and SEBS (top) and the proposed pressure sensing mechanism (bottom). (B-ii) SEM images of the carbon flower (top, left) and the

surface of the printed composite (right). An AFM image of the composite (bottom, left). (B-iii) Stable resistance response under applied pressure at different bending radii. Reprinted with permission from ref [204]. Copyright 2020 John Wiley and Sons.
(C-i) A SEM image showing the surface morphology of the CNT network-coated thin, porous PDMS sponge (CCPPS) (left) and an enlarged SEM of CNT layers coating the porous PDMS backbone (right), forming conductive networks. (C-ii) Minimal changes in base resistance of the pressure sensor at varied bending radii from 50 mm to 7.5 mm, under both parallel and perpendicular electrode arrangements. (C-iii) Simulation analysis of bending strain within the CCPPS structure, with local strain on most PDMS bridges measured to be $\lesssim$10% at bending radii of $\lesssim$ 5 mm. Reprinted with permission from ref [200]. Copyright 2019 American Chemical Society.

Structural Designs for Pressure Sensors Insensitive to Strain

Large Islands Approach

One simple and effective method to achieve strain-insensitive pressure sensors is the "large islands" approach, which involves depositing sensing components onto stiffer areas surrounded by softer regions. This mechanical mismatch between stiff and soft areas results in a much smaller strain applied to the stiff zones, allowing for stable working areas and working distances. This technique can be used with various types of pressure sensors, regardless of their operating principles.

For example, in capacitive pressure sensors, Steve *et al.* fabricated a porous pyramid PDMS dielectric layer.[105] The strain insensitivity was demonstrated by placing the sensing components (electrodes and porous pyramid dielectric) onto high elastic modulus PDMS substrates (1910 kPa), surrounded by lower elastic modulus Ecoflex (50 kPa). This mismatch in elastic modulus caused the PDMS platforms to experience only 5.2% local strain when subjected to 50% overall strain, allowing the sensors to remain insensitive to strain up to 60% (**Figure 12A**).

In triboelectric pressure sensors, Hui *et al.* used a similar "large island" strategy, creating a stiff island that also served as a sensing component.[58] They treated PDMS and a PDMS/MXene/CNT mixture with Methacylic Acid (MAA) monomer, a cross-linker (ethylene glycol dimethacrylate (EGDMA)), and Irgacure 651, followed by ultraviolet (UV) exposure in an inert atmosphere to create the stiff working area. This resulted in a local strain of less than 15% under 200% overall strain, enabling stable performance up to 120% strain (**Figure 12B**). However, at 150% strain, output performance dropped by 10%, likely due to small deformations in the sensing island and increased electrode resistance inside the sensor. While the open-circuit voltage (V_{OC}) is ideally unaffected by electrode resistance, internal impedance can be influenced by changes in electrode resistance during stretching, affecting the current. Thus, maintaining stable electrode resistance is essential in triboelectric pressure sensors, which can be addressed using pre-strain methods.[195, 205]

For piezoresistive pressure sensors, adding a stiff layer on the back can stabilize the sensing region, but the challenge lies in creating stretchable electrodes and maintaining a stable interface between the electrodes and the sensing element. Xuyang *et al.* [201] proposed a strategy using pre-stretching and microstructured engineering to develop stretchable electrodes with low resistance (4.68 Ω, increasing to 1.53 Ω at 30% strain). The pressure sensor itself had an initial resistance of 9262 Ω, which increased by only 127 Ω under minimum loaded pressure. This resulted in strain insensitivity up to 20% (**Figure 12C-i** and **12C-ii)**. However, at 30% strain, the sensor's insensitivity was compromised, likely due to increased interface resistance between the sensing element and electrodes, despite the interface's demonstrated high peel strength (**Figure 12C-iii**). Although the "large island" approach stabilizes sensing elements during strain, it may lead to high local strain or stress concentration in the surrounding soft areas, a phenomenon known as

the "island effect".[206] To mitigate this, Yihui's research group [206] introduced a buffer or ring buffer layer between the island and the substrate, achieving better linear displacement distribution and improving the stretchability by a factor of 2 (**Figure 12D**).

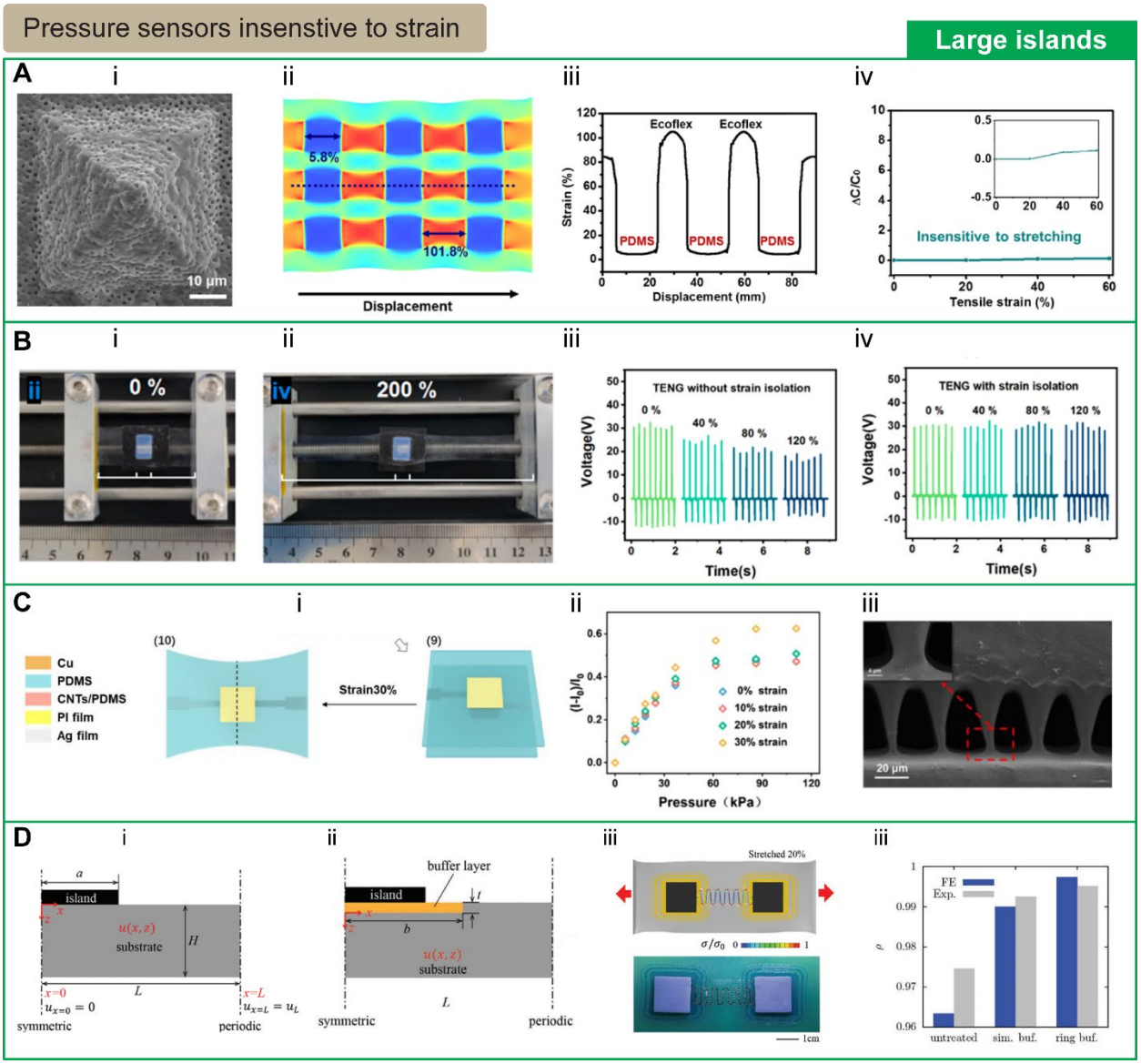

Figure 12. Pressure sensors insensitive to strain through the "large island" approach.
(A-i) Top view SEM images of a single porous pyramid used for the dielectric layer. (A-ii) and (A-iii) Finite element simulation (FEM) images showing local strain under 50% overall strain and the corresponding strain profile, respectively. (A-iv) Minimal changes in capacitance under tensile strain. Reprinted with permission from ref [105]. Copyright 2019 American Chemical Society.

(B-i) and (B-ii) Optical images of strain-isolating substrates at 0% and 200% strain, respectively. (B-iii) and (B-iv) Degraded output voltage in TENG without strain isolation, compared to stable output with strain isolation. Reprinted with permission from ref [58]. Copyright 2023 Elsevier.
(C-i) Schematic of a pressure sensor with stiff PI film at relaxed and 30% strained conditions. (C-ii) Normalized current response to pressure for the sensor under various strain conditions. (C-iii) Cross-sectional SEM image showing the interlinked interfaces between the electrode and active material. Reprinted with permission from ref [201]. Copyright 2023 Elsevier.
(D-i) and (D-ii) Schematic diagrams of a representative volume element (RVE) for a 2D periodic island-bridge model on a soft substrate, without and with a buffer layer, respectively. (D-iii) FEA results and experimental images for 2D serpentine interconnects featuring a ring buffer layer, designed to enhance stretchability. (D-iv) Correlation coefficient of the displacement distribution's linearity. Reprinted with permission from ref [206]. Copyright 2022 John Wiley and Sons.

Small Islands/Ridges Approach

The "small islands/ridges" approach offers an alternative to "large islands" by integrating smaller, stiff regions into the active components, helping to maintain stable working areas and distances. This method is particularly beneficial in applications like skin contact, where large, stiff regions may not be ideal. However, fabricating "small islands/ridges" can be more challenging than implementing "large islands".

For example, Sihong's research group developed a capacitive pressure sensor based on an electrical double layer (EDL), where capacitance changes with increasing contact area under pressure.[39] In this sensor, ionic elastomer pyramids (350 μm height) contact the top electrode. Stiff, conductive materials were introduced at the base of these ionic pyramids to maintain consistent contact area under strain, achieving only a 2% variation in capacitance under 50% strain and minimal impact on sensing performance. Additionally, soft spacers at the sensor ends

helped maintain a consistent distance between the top and bottom layers, further stabilizing performance under strain (**Figure 13A**).

In triboelectric pressure sensors, *"small ridges"* can be implemented either on the surface of soft substrates [199] or within soft matrices.[40] For instance, one design involved hard wrinkle PDMS patterns (250 μm height) on the surface of a soft PDMS substrate (**Figure 13B-i**).[199] The modulus mismatch caused the softer PDMS to absorb most of the strain, preserving the contact area with the other triboelectric layer, whereas, in the uniform modulus counterpart, strain resulted in uniform deformation, which increased the contact area (**Figure 13B-ii**). This design achieved only a 2% change in voltage under strain from 0 to 80% (**Figure 13B-iii**). Another approach embedded "small ridges" within a soft hydrogel matrix using the Liesegang patterning phenomenon and pre-strain methods.[40] These ridges (210–340 μm height) were rich in $CuCrO_4$ crystals **(Figure 13C-i)**, and when coated with a thin film of PVDF-HFP-TFE (6.5 μm), the sensor exhibited stable output voltage and sensitivity under 50% strain (**Figure 13C-ii** and **13C-iii**).

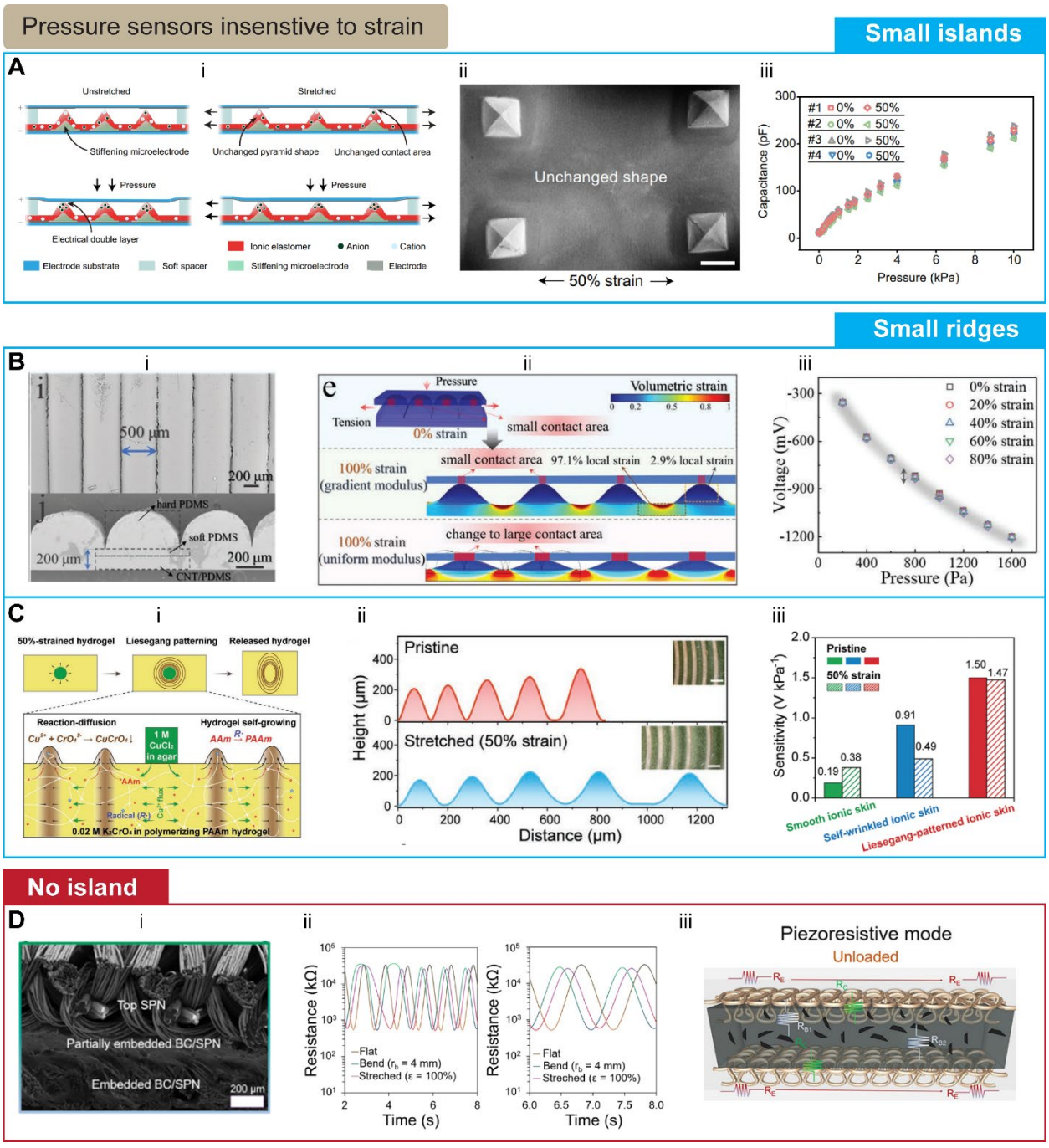

Figure 13. Pressure sensors insensitive to strain through "small islands/small ridges" and "no island" approaches. (A-i) Schematic of the pressure sensing mechanism that maintains performance under stretching. (A-ii) SEM images of micropyramid structures featuring stiffening microelectrodes on the backside at 50% strain. Scale bars: 500 μm. (A-iii) Capacitance responses to pressure from four sensors at 0% and 50% strain. Reprinted with permission from ref [39]. Copyright 2021 The American Association for the Advancement of Science.

(B-i) SEM images showing a top view of wrinkle-patterned friction layers (top) and a cross-sectional view of the underlying CNT/PDMS elastic substrate (bottom). (B-ii) Comparison of contact area changes and volumetric strain

distribution between gradient-modulus and uniform-modulus models under simultaneously applied constant pressure and 100% strains. Cross-sectional SEM images of both models (bottom) are also shown. (B-iii) Stable voltage response to increasing pressure, regardless of applied in-plane strains. Reprinted with permission from ref [199]. Copyright 2022 John Wiley and Sons.
(C-i) Schematic and mechanism of Liesegang patterning of PAAm hydrogel through reaction-diffusion and polymerization-induced self-growth. (C-ii) Height profiles of Liesegang-patterned hydrogels in pristine and stretched conditions (scale bar for inset figures: 200 μm). (C-iii) Stable sensitivity of Liesegang-patterned sensors at 50% strain, compared to other sensors. Reprinted with permission from ref [40]. Copyright 2023 John Wiley and Sons.
(D-i) FE-SEM image of a sensor composed of a silver-plated nylon (SPN) electrode layer, partially embedded in a biocarbon composite interface (BC/SPN). (D-ii) Dynamic response of the piezoresistive pressure sensor to normal pressure (~25 kPa) under flat, bending, and stretching conditions. (D-iii) Schematic of the piezoresistive BC/SPN device. Reprinted with permission under a Creative Commons CC BY 4.0 License from ref [207]. Copyright 2020 American Chemical Society.

No Island Approach

Some piezoresistive pressure sensors achieve strain insensitivity without relying on stiff islands. For instance, one design achieved stable sensitivity under 20% strain [208], and another maintained stable output performance up to 100% strain.[207] The former sensor had a patterned surface inspired by human skin, coated with AgNPs, with convex regions for contacting, allowing the contact area to remain relatively unchanged under small strains. The latter sensor embedded or partially embedded e-textiles in a biocarbon dielectric layer (**Figure 13D-i** and **13D-ii**). The authors mentioned small changes in contact area under strain, suggesting that the outer layers of non-embedded knitted fabrics (outer layers) absorbed the strain, leaving the geometry of the embedded fabrics almost unchanged under the deformation (**Figure 13D-iii**). In both cases, maintaining stable electrode conductivity or ensuring that changes in the sensing component's resistance significantly outweigh changes in electrode resistance under stretching deformations was critical for achieving strain insensitivity.

Several approaches have been developed to suppress interference from bending and strain deformations for more accurate soft pressure sensors. When being used for human biophysical signal detection, the ultrathin pressure sensors demonstrated their capability of monitoring chest vibrations induced by heartbeats and the speed of pressure propagation within an artificial blood-vessel model.[57, 203] The effectiveness of the bending insensitivity, on the other hand, was validated by using pressure-sensor matrix conformally wrapped on a balloon. The only detection of corresponding normal pressure distribution on the balloon under finger pinching meant minimal effect of bending or strain on pressure sensors at other positions.[57] Apart from human biophysical monitoring, the use of the insensitive soft pressure sensors in human-machine interfaces and soft robotics clearly realize accuracy benefit. For example, stretching the insensitive pressure sensor array to 20% had little impact on spatial distribution of pressure.[201] It is beneficial as wearable pressure sensor arrays can deform with the skin without performance degradation and perform communication with a computer.[195] Moreover, strain-insensitive pressure sensors were demonstrated promising in soft robotic hand applied for recording the arterial pulse signals.[39] The effectiveness was validated by (1) stable signals under pneumatically actuating the robotic finger that induced bending to the sensors, (2) maintaining the preset pressure under human arm movement, and (3) comparison with conventional stretchable pressure sensor.

Strain Sensors Insensitive to Off-Axis Mechanical Deformations

In wearable applications, such as human motion tracking, human-machine interaction, or soft robotics, soft strain sensors are not restricted to areas with single axial joints (e.g., figures), but are applied to more complex 3D areas with multiple strain directions.[41, 43] For example, when human hand, a very complicated organ, performs various motions, like grasping, writing, typing,

or making martial art gesture, the skin deforms in complex ways, varying in both direction and degree.[41, 42] Moreover, the actuator of soft robots can consist multiple parts that makes self-perception difficult to achieve.[209] Those parts are connected in a joint region which can experience strain in different directions under internal or external loads.[196] Thus, it is important to accurately differentiate the deformations in those complicated regions, improving detection quality of human motions and robotic self-perception. Therefore, soft strain sensors are required to provide accurate information about the direction and amplitude of tensile strains on moving surfaces.[210, 211] It is an adverse task since a strain sensor experiences strains in more than one direction, while conventional strain sensors are typically designed to detect strain along a preset direction without the ability to distinguish multi-axial motions.[42] Moreover, skin surface movement or external contact forces inevitably induce bending and compression in the strain sensors, further challenging tensile strain detection.[59] Therefore, developing strain sensors tailored to targeted tensile strain directions is important to meet the application demands. This subsection provides approaches to suppress the impact of those off-axis deformations (i.e., out-of-plane pressure, torsion, bending, or off-axis in-plane strains).

Strain sensors can be based on triboelectric effect, capacitive effect, and piezoresistive effect. During wearable sensing, off-axis deformations from the skin deformations or external forces can significantly alter either the geometry or the electrical properties of the sensors, affecting sensing performance. Geometrical changes primarily affect triboelectric or capacitive strain sensors, while changes in electrical properties impact piezoresistive strain sensors.

For triboelectric strain sensors, both desirable and undesirable deformations modify the geometry of the sensing materials, contributing to signal generation. Recently developed triboelectric strain sensors utilize knitted pairs of different fabrics or helically wound outer sheaths around core

fibers with adjustable gaps.[212, 213] However, these designs feature unavoidable geometrical gaps between materials in the out-of-plane direction, which can make the sensors highly sensitive to off-axis deformations, particularly pressure. In contrast, triboelectric sensors made from two different shell fibers, twined around a core fiber and interwoven with each other, form another design approach.[214] Since strain-induced geometrical gaps appear between the two twined fibers only in the stretching direction (not out-of-plane), pressure is expected to have minimal impact on sensing performance. However, the effects of off-axis deformations in this design have not yet been thoroughly characterized and warrant further investigation.

Capacitive strain sensors come in two types, each responding differently to undesirable deformations. The first type is based on parallel capacitance, which is highly sensitive to pressure because it alters the geometry - specifically, the distance between electrodes.[215, 216] The second type uses in-plane capacitance, where electrodes are arranged in an interdigitating pattern. Strain changes the in-plane distance between these electrodes, leading to changes in capacitance.[217, 218] Since the capacitance is primarily affected by in-plane deformation, pressure is unlikely to impact sensing performance significantly, though other off-axis deformations may still have an effect, which remains untested.

For piezoresistive strain sensors, any deformation that disrupts the initial conductive paths (through cracks, reduced contact areas, or increased filler distances) alters the electrical properties. Completely eliminating responses to undesirable deformations is challenging. However, sensor design and material configuration can be optimized to minimize the impact of off-axis deformations. These approaches can be classified into two categories: (1) minimizing the effects of other in-plane directions, and (2) minimizing the influence of pressure, torsion, or

bending. Both materials engineering and structural design techniques have been employed to achieve these goals.

Materials Engineering and Structural Designs for Piezoresistive Strain Sensors Insensitive to Other In-Plane Directions

Isotropic electrical properties in piezoresistive strain sensors can lead to unreliable resistance changes when the sensors are stretched in multiple directions. To improve reliability, sensing materials and structures should be configured to exhibit anisotropic electrical properties, ensuring that the sensor displays the highest response to deformation along a specific direction while showing minimal or negligible responses to deformations from other directions.

Materials Engineering for Intrinsic Anisotropic Properties

In this context, sensing materials are often aligned in one orientation. For simplicity, stretching in the alignment direction will be referred to as "parallel," while stretching perpendicular to the alignment will be called "perpendicular." One widely used material is CNTs, whose alignment has been extensively studied and achieved using various methods.[219] One of the earliest methods involved drawing CNTs from CNT forests, which produces highly aligned CNTs in the drawing direction due to Van der Waals forces (**Figure 14A-i** and **14A-ii**).[220, 221] This method results in a significantly higher change in electrical resistance when stretched in the parallel direction compared to the perpendicular direction.[222, 223] For example, the change in resistance can be as high as 300% in the parallel direction, compared to just 5% in the perpendicular direction at 250% strain (**Figure 14A-iii**). Another type of material used is aligned nanofibers, which can be fabricated via electrospinning followed by post-treatment through heating.[42, 43] For instance, highly aligned carbon nanofibers (ACNF) were created by electrospinning a polyacrylonitrile

(PAN) dispersion.[43] The collector used two spaced electrodes set at an inclined angle of 15° (**Figure 14B-i** to **14B-iii**). Optimal parameters included 10 wt% PAN, 8 hours of electrospinning time, stabilization at 230 °C, and carbonization at 1000 °C. This material exhibited a large difference in GF within 30% strain, showing a GF of 180 in the parallel direction compared to just 0.3 in the perpendicular direction (**Figure 14B-iv**). In general, these materials are suitable for multi-directional sensing and are often demonstrated through a cross-plied assembly.

The mechanism behind this aligned anisotropic electrical behavior can be explained by three types of electrical resistance within the materials: intrinsic fiber resistance (R_{int}), contact resistance between fibers (R_C), and crack resistance when fibers become disconnected (R_{crack}). When stretched in the parallel direction, both R_C and R_{crack} change, with R_{crack} dominating at high strain levels, leading to a significant increase in resistance (**Figure 14C-i**). In contrast, stretching in the perpendicular direction transfers stress to interconnected fibers through their entanglement points, creating torque that rotates the fibers instead of distancing or breaking them. This results in a smaller change in resistance, primarily due to a reduction in the contact area between adjacent fibers (**Figure 14C-ii)**.[43, 222] Images showing the dislocation of aligned nanofibers under 30% strain in both directions are provided in **Figure 14C-iii** and **14C-iv**.[43]

Introducing a wrinkled or corrugated surface structure can also induce anisotropic electrical behavior in sensing materials. For example, a corrugated Ag NW percolation network was produced using a pre-strain method. When stretched perpendicular to the wrinkle length, the surface unwrinkles and flattens rather than breaking or damaging the conductive materials, leaving conductive paths unchanged and inducing minimal change in resistance. However, stretching parallel to the wrinkle length increases the distance between conductive nanowires, leading to a rise in resistance. This sensor exhibited a moderate GF of 20 within 35% strain in

this parallel direction.[41] Similarly, carbonized wrinkled cellulose paper demonstrated anisotropic electrical properties [224], which was made from aligned cellulose fibers with wrinkles introduced perpendicular to the fiber length. Stretching perpendicular to the alignment (parallel to the wrinkle length) increased resistance (GF of about 10 and 4 within 6% strain) (**Figures 14D-i** and **14D-ii**). This differed from the aligned CNTs or aligned electrospun nanofibers mentioned above [42, 43, 222, 223], where stretching perpendicular to the alignment insignificantly increased resistance. The difference arose due to significant deconstruction and the appearance of cracks in the carbon fiber matrix, which damaged the conductive pathways. Consequently, there appeared to be weak bonding and fewer interconnections between the cellulose fibers. This may be because the cellulose paper was composed of aligned micro-ribbons (**Figure 14D-iii**), whereas the CNTs and nanofibers were aligned nanotubes and nanofibers, which have a greater likelihood of forming entanglement points.

In addition to flexible nanomaterials, hard semiconductors like silicon (Si) and silicon carbide (SiC) also exhibit anisotropic electrical properties due to their crystal structures.[225] For example, p-type cubic SiC has the highest GF of 30.3 in the <110> direction, while other directions show lower GFs.[226] Conversely, n-type cubic SiC has a GF of -31.8 in the <100> direction, with lower GFs in other directions [227]. Although SiC materials offer electrical anisotropy, chemical inertness, and high-temperature resistance, their application in wearable sensors is limited by their rigidity. Therefore, further strategies are needed to make these materials more flexible or even stretchable.

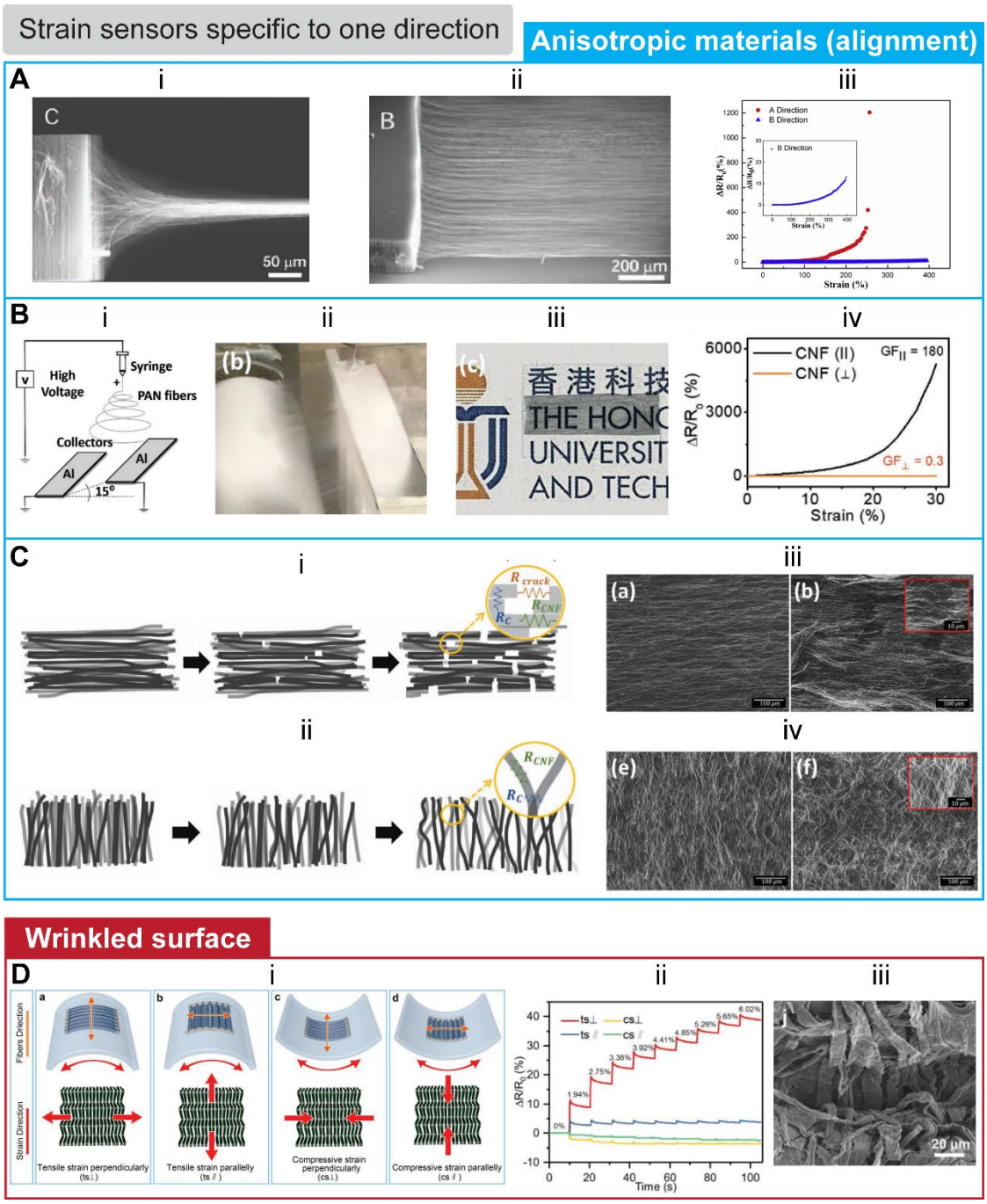

Figure 14. Piezoresistive strain sensors specific to one direction using anisotropic materials.

(A-i) and (A-ii) SEM images showing aligned CNT sheets drawn from a CNT forest, at 90° and 35° angles relative to the forest plane, respectively. Reprinted with permission from ref [220]. Copyright 2005 The American Association for the Advancement of Science. (A-iii) Relative resistance changes in aligned CNT sheets when being stretched in A direction and B direction. A direction is parallel to the CNT alignment, while B direction is perpendicular to the alignment. Reprinted with permission from ref [222]. Copyright 2018 Elsevier.

(B-i) Schematic of electrospun anisotropic carbon nanofiber (ACNF) films. (B-ii) Photograph of a suspended, aligned PAN nanofiber film across two inclined collectors. (B-iii) Photograph of the obtained ACNF/PDMS composite. (B-iv) Changes in relative resistance vs. strain in single-layer ACNF strain sensors, with CNFs aligned parallel and perpendicular to the stretching direction.
(C-i) Schematic of the sensing mechanism for sensors with fibers aligned parallel to the stretching direction. (C-ii) Schematic of the sensing mechanism for sensors with fibers perpendicular to the stretching direction. (C-iii) SEM images of ACNF strain sensors with fiber alignment parallel or perpendicular to the stretching direction at 0% (left) and 30% (right) strain. Reprinted with permission from ref [43]. Copyright 2019 John Wiley and Sons.
(D-i) Schematic illustrating four different bending modes of a carbonized crepe paper (CCP) strain sensor, including outward bending perpendicular to fibers direction (ts⊥), outward bending parallel to fibers direction (ts∥), inward bending perpendicular to fibers direction, and inward bending parallel to fibers direction (cs∥) (from left to right). (D-ii) Relative resistance changes of CCP sensors under strain in different directions, with the highest response for strain perpendicular to the alignment. (D-iii) Enlarged SEM image of CCP in its original state. Reprinted with permission from ref [224]. Copyright 2018 John Wiley and Sons.

Structural Design for Anisotropic Properties

Isotropic materials can be engineered to exhibit greater electrical responses in one direction compared to others. Fabrics, for example, are commonly made by weaving yarns together, where the yarns can be oriented in warp and weft directions. This allows for easier stretching in one direction and resistance in the others, creating a direction-specific property.[59] Beyond fabrics, anisotropic properties can be achieved by designing suitable sensing structures, such as (1) meander or serpentine structures [196, 210], (2) micro/nano-scale cracks with controlled orientations [211, 228, 229], and (3) mechanical mismatch.[230, 231]

Meander or serpentine structures, with or without initial contact between parallel tracks, can produce anisotropic electrical responses. Structures without initial contact show significant stress concentration in regions parallel to the stretching direction, resulting in anisotropic electrical behavior (**Figure 15A**).[210] In contrast, structures with initial contact between parallel tracks

exhibit a higher change in resistance when stretched perpendicular to the tracks, due to a reduction in contact area **(Figure 15B-i** to **15B-iv)**. The change in resistance along the parallel tracks depends primarily on the piezoresistive effect and can be low if the material has a low piezoresistive coefficient (**Figure 15B-v** and **15B-vi**). However, this design typically has a low sensing range (< 5% strain) but a high GF above 1000.[196]

Isotropic materials, such as metals, can also be scaled down to micro or nanometer widths to achieve anisotropic electrical responses.[211] For nanometer-scale widths, stretching along the length induces cracks perpendicular to the stretching direction, increasing resistance. When stretched perpendicularly, few cracks form, resulting in a smaller change in resistance. This creates a large difference in electrical responses between the two directions. However, for micrometer-scale widths, stretching in either direction can cause cracks, reducing the discrepancy in electrical response (**Figure 15C-i** to **15C-iv**). The larger width of micrometer-scale materials leaves more conductive paths intact, leading to lower sensitivity compared to nanometer-scale widths (**Figure 15C-v** to **15C-vii**). The sensing range of this crack-based mechanism is also low (< 5% strain), with GFs around 24 and 65.

The mechanical mismatch between soft and stiff substrates can cause larger stress concentrations in one direction, leading to anisotropic electrical responses. For example, a stiffness-variant stretchable substrate was fabricated by embedding a rectangular soft polymer within a hard substrate.[230] Simulations showed much higher stress in the stretching direction, resulting in significant differences in electrical responses between the two directions. Another example involved rigid islands (PET substrate) placed under two large electrode pads, with a sensing element bridging the electrodes (**Figure 15D-i** and **15D-ii**).[231] Both the electrodes and the sensing element were made from the same CNT/CB/PDMS composite, ensuring mechanical

difference only caused by the rigid PET substrates. This mechanical mismatch resulted in strain concentration, where only the sensing element responded to deformation along its length, yielding a GF of ~ 8 within 35% strain. In the perpendicular direction, however, the rigid regions restricted deformation, causing little change in resistance. The sensor's performance and simulations are shown in **Figure 15D.** After optimizing the design, including using a 3-sensor array in a triangular configuration and machine learning techniques, the array achieved high accuracy in detecting both the direction and intensity of applied strain.

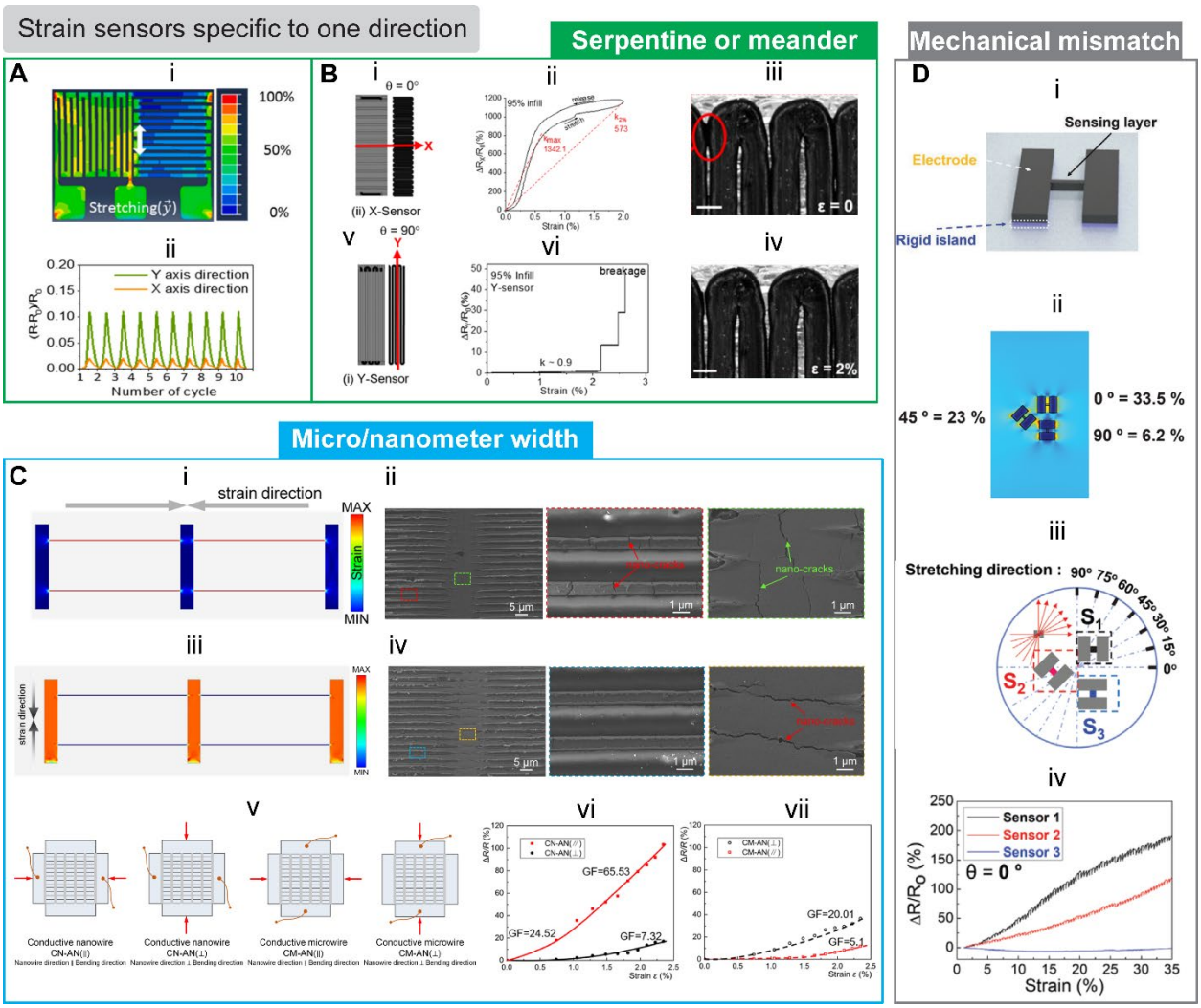

Figure 15. Structural designs to achieve piezoresistive strain sensors specific to one direction.

(A-i) Finite element analysis (FEA) results of a meander-structured sensor during stretching along the Y direction (vertical direction). (A-ii) Responses of the sensor in the X and Y directions at 5% strain applied along the Y direction. Reprinted with permission from ref [210]. Copyright 2022 Elsevier.
(B-i) and (B-v) Schematics of two types of serpentine-structured sensors: an X-sensor with contacted tracks and a Y-sensor with long parallel tracks, respectively. The stretching direction of the two sensors is parallel to the Y axis. (B-ii) and (B-vi) Sensing performance of the X-sensor and Y-sensor, showing the Y-sensor with almost no response to strain. (B-iii) and (B-iv) Microscopic images of an X-sensor at its original state and at 2% strain, showing reduced effective contact area. Scales bar is 400 μm. Reprinted with permission from ref [196]. Copyright 2020 American Chemical Society.
(C-i) and (C-iii) Finite element method (FEM) simulation results showing strain distribution within hierarchical aligned micro-/nanowire (HAMN) networks (top view) under strain either parallel or perpendicular to the nanowire array, respectively. (C-ii) and (C-iv) show SEM images of the nanocrack distribution in the hierarchical aligned network (left), with enlarged images highlighting the distribution in the nanowires (middle), and microwires (right). When stretched in the direction perpendicular to the nanowires, almost no cracks appeared in the nanowires. (C-v) provides a schematic illustration of different strain modes, showing the stretching direction either along or perpendicular to the conductive path. (C-vi) and (C-vii) display the corresponding sensing responses of the sensors under different strain modes, demonstrating anisotropic electrical behavior. Reprinted with permission from ref [211]. Copyright 2022 American Chemical Society.
(D-i) Schematic of a unit strain sensor with strain-insensitive electrode regions and a strain-sensitive channel region. (D-ii) FEA simulation showing local strain at 30% strain (parallel to the two electrodes at the right bottom). (D-iii) Defined stretching directions for the sensor matrix. (D-iv) Relative resistance change versus strain in the range of 0% to 35% for a three-strain sensor array in the defined 0° direction. Reprinted with permission from ref [231]. Copyright 2023 John Wiley and Sons.

Materials Engineering and Structural Designs for Piezoresistive Strain Sensors Insensitive to Pressure, Bending, and Torsion

In terms of material configuration, a porous structure can be utilized to develop strain sensors that are insensitive to pressure [232], even though pressure can generally create conductive paths.[233] One example involves mixing MWCNTs with PDMS and evaporating the water to form a porous structure, a method distinct from other template-based porous strategies. Images of the samples show a small fraction of MWCNTs protruding from the pore walls, while most are embedded

within the PDMS (**Figure 16A-i** to **16A-iii**). Tests with varying MWCNT concentrations (36 vol% to 57 vol%) revealed that the 57 vol% solution, with higher porosity, exhibited less change in the formation of the MWCNT network. This means that pressure primarily caused the pores to close, with minimal effect on the connections between MWCNTs. As a result, the porous strain sensor displayed almost no response to pressure (**Figure 16A-iv**).[232]

On the structural design front, various approaches have been proposed to mitigate the effects of pressure, bending, and torsion on sensors. Some designs incorporate supports to resist unwanted forces, such as normal forces [197, 234], while others shape the sensing elements to minimize stress concentrations under such forces.[44, 198]

One approach involves using protruding tips as supports to reduce the impact of pressure. When sensing nanomaterials are coated on a substrate with minimal thickness [235], uniform pressure exerts little impact on strain-sensing performance because there is no local stress or deformation in the sensing materials. However, localized pressure can still cause deformations in specific areas, interfering with strain sensing.[197, 236] This issue can be addressed by adding micro-protruding tips to the surface, which resist pressure and also provide a self-attachable property to the sensors.[197]

Incorporating non-conductive materials as supports between the top and bottom conductive fibers in fiber-based strain sensors can also reduce the electrical response to pressure. These sensors operate based on deformation-induced contact between conductive fibers, and different types of deformations - strain, pressure, or flexion - can alter the contact area.[234] By introducing non-conductive supports between the fibers, excessive contact due to pressure is minimized, resulting in a very low-pressure response (~0.006 kPa^{-1} at 100 kPa) (**Figure 16B-i).**[59] This design

also limits the response to bending, with the change in electrical resistance remaining below 16% even at 75% bending (**Figure 16B-ii** to **16B-iv**).

Another approach is to use serpentine or meander structures, which can mitigate the effects of bending, torsion, and pressure.

The serpentine structure is particularly effective at reducing stress concentrations, making it a popular choice for fabricating stretchable electrodes.[237, 238] For example, a highly elastic strain sensor made from multiple conductive materials and Ecoflex polymer was created using laser-cut serpentine structures (**Figure 16C-i**).[198] This sensor exhibited stable performance at bending radii from 0 to 8 mm, with only slight fluctuations in twisting tests up to 180^{o} of torsion. Additionally, there were no significant electrical fluctuations under normal pressures ranging from 0 to 60 kPa, demonstrating the effectiveness of the serpentine structure (**Figure 16C-ii** to **16C-iv**). However, the sensor's sensitivity was low, with three regions showing GF of < 2 for the wide regions and 8.67 for the narrow middle region. This low sensitivity may result from the stress-relieving effects of the serpentine structure.

Similarly, meander structures can make strain sensors insensitive to pressure, bending, and torsion. These structures maximize the electrical response in a specific direction as mentioned earlier while also minimizing responses to off-axis deformations, including pressure, bending, and torsion (**Figure 16D**).[33, 210]

A meander structure with initial contact using low piezoresistive materials enhances both sensitivity and insensitivity to pressure, bending, and torsion.[44] In this design, uniaxially aligned carbon fibers, pre-impregnated with an epoxy resin, were laser cut into meander shapes, and then sandwiched between pre-strained TPU films. Upon release, the meanders formed initial contacts,

reducing electrical resistance (**Figure 16E-i**). Under tensile strain, the contact area of the meanders decreased, and when this area reached zero, saturation occurred with minimal changes in resistance. This design resulted in an ultrahigh GF of ~9400 and high linearity, but the sensing range was limited (< 5%) (**Figure 16E-ii**). Additionally, the stiff, low piezoresistive materials and the meander structure made the sensor highly resistant to off-axis deformations, including bending, torsion, and pressure. For example, the sensor showed less than a 3% change in initial resistance under applied pressures up to 100 kPa and demonstrated robustness and damage resistance, withstanding punctures from a scalpel, hammer strikes, high loads (> 500 kPa), and even a 1500 kg car driving over it (**Figure 16E-iii** and **16E-iv**).

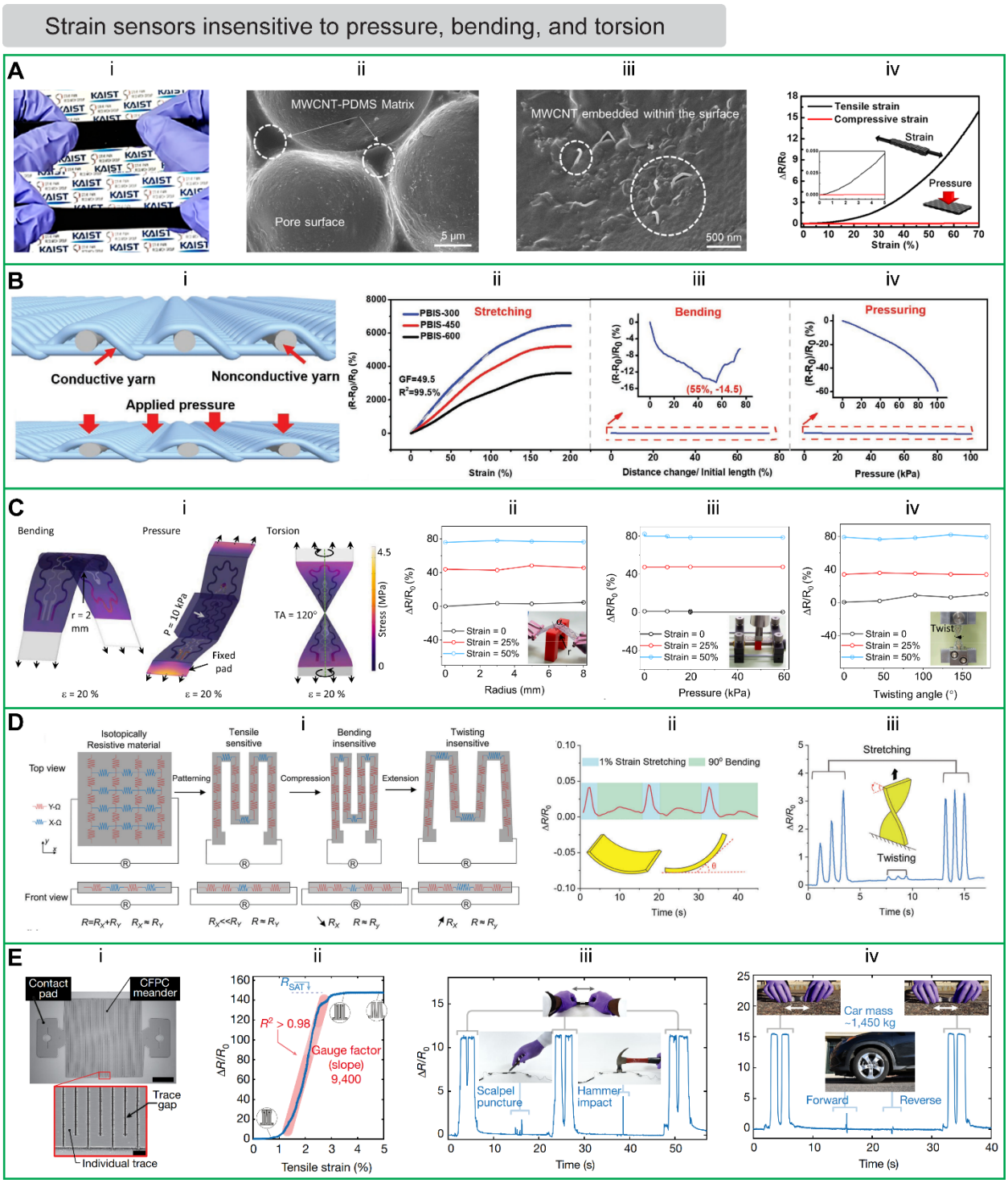

Figure 16. Strategies for piezoresistive strain sensors insensitive to pressure, bending, and torsion.

(A-i) Optical photograph of a stretchable pressure-insensitive strain (SPIS) sensor demonstrating its stretchability. (A-ii) and (A-iii) SEM images showing small amounts of MWCNTs protruding from the pore walls, while most of the MWCNTs remain embedded within the PDMS. (A-iv) The porous sensor's response to strain without

interference from applied pressure. Reprinted with permission from ref [232]. Copyright 2018 American Chemical Society

(B-i) Cross-sectional view of a pressure- and bending-insensitive strain (PBIS) sensor at its original state (top) and under applied pressure (bottom), showing insensitivity to compression due to the separation of two conductive yarn layers by non-conductive yarns. (B-ii), (B-iii), and (B-iv) Sensing performance of PBIS sensors at different densities, with minimal response to bending and pressure. Reprinted with permission under a Creative Commons CC BY 4.0 License from ref [59]. Copyright 2021 John Wiley and Sons.

(C-i) Simulated off-axis deformation induced by torsion, pressure, and bending at 50% tensile strain for a strain sensor using a serpentine structure, showing low local stress. (C-ii), (C-iii), and (C-iv) Pressure, torsion, and bending-insensitive sensing performance of the serpentine sensor. Reprinted with permission from ref [198]. Copyright 2022 Elsevier.

(D-i) Meander design optimized for maximum electrical response in a specific direction (Y) and minimal response to off-axis deformations. (D-ii) and (D-iii) Significantly lower electrical responses to bending and twisting compared to stretching. Reprinted with permission under a Creative Commons CC BY 4.0 License from ref [33]. Copyright 2023 John Wiley and Sons.

(E-i) SEM image of a carbon fiber polymer composite (CFPC) meander (scale bar: 2 mm). The inset shows a magnified view of a region near the meander edge (scale bar: 200 μm). (E-ii) Sensor performance showing a high GF of 9400 and linearity $R^2 > 0.98$). (E-iii) and (E-iv) Demonstration of sensor resilience to extreme conditions such as punctures from a scalpel, hammer strikes, and being driven over by a car. Reprinted with permission from ref [44]. Copyright 2020 Springer Nature.

Different strategies enable integration of insensitivity to off-axis deformations into soft strain sensors. The strategies' effectiveness has been validated through applications demonstrated in biophysical detection, human-machine interaction, and soft robotics. For instance, the strain sensors insensitive to pressure and bending was attached on the knee joint, showing stable, different signal responses during walking and running.[59] Featuring insensitivity to twisting, torsion, and pressure, wearable strain sensors could detect physical signals from wrist joint bending, back bowing, elbow bending, or eye blinking with high signal-to-noise ratio or low noise interference.[33, 198] In addition, two strain sensors insensitive to off-axis in-plane directions were usually assembled into cross-plied structure to sense strains in multiple directions. The cross-plied sensors were attached on hand, wrist, neck, or shoulder, clearly showing different patterns corresponding to various motions, such as ventral or rotational movement of neck, flexions or ulnar deviations of wrist, and martial art gesture of hand.[42, 43] Sports management, such as improving golf shooting performance, was also demonstrated by attaching the cross-

plied sensors on wrist to monitor golf grip.[43] For human-machine interaction, these sensors could be utilized to control a 2-degree-of-freedom robot or guide an object to the required position.[41, 42, 224] In soft robotic application, a cross-plied sensor was demonstrated to have capability to differentiate the movement of a four-arm actuator.[196]

Other Specific Biophysical Sensors

In addition to the electromechanical sensors used for monitoring biomechanical signals, such as joint movement, wrist pulse, and respiratory movement by transducing mechanical deformation into electrical signals, electrophysiological sensors also warrant discussion. These sensors have specific sensing capabilities, meaning they can detect only one type of electrophysiological signal. For example, electrodes placed on the biceps can detect EMG signals, while those positioned on the chest can detect ECG signals. Similarly, EEG signals can be detected by sensors placed around the head, and EOG signals by sensors near the eyes. In this way, specificity can often be achieved simply by placing the sensors in the correct locations. However, various internal and external factors can interfere with the sensors' performance. Internal factors include interference between different electrophysiological signals; for instance, weaker EEG signals (in the microvolt range) can be masked by stronger EMG signals. External factors mostly arise from the detachment or displacement of the electrode sensors from the tissues, which affects the bioelectric-tissue interface and degrades signal acquisition. Additionally, mechanical deformation of the tissue (such as the skin) can alter the electrodes' electrical properties, further reducing sensing performance. These external disruptions are commonly referred to as motion artifacts.

Minimizing these interferences is crucial for accurate electrophysiological signal detection. While strategies to mitigate interference between different signals typically rely on circuit design

and algorithms, separating internal factors solely through material and design approaches is challenging. On the other hand, interference from motion artifacts can be reduced by securing the bioelectric-tissue interface and maintaining stable electrical properties during tissue deformation. This can be achieved through both materials engineering and structural designs. For instance, making the sensing electrodes thin ensures close contact with the tissues (minimizing gaps), while designing the electrodes to be soft and stretchable with strain-insensitive electrical properties allows them to function effectively under tissue deformation. More detailed methods for mitigating these issues can be found in previous reviews.[239-241] Beyond mechanical considerations, the ambient environment can also impact electrical properties, influencing sensing performance. Therefore, electrode sensors can be engineered to be insensitive to temperature, humidity, and liquids, as discussed earlier, to enhance their stability and ensure reliable signal acquisition.

Conclusions and Outlook

In conclusion, we have summarized various approaches for achieving specialized sensors for more stable and accurate detection of physical signals, applied in health monitoring, sports management, human-machine interaction, and soft robotics. The specific properties of electromechanical sensors are often achieved by making them insensitive to temperature, humidity/liquid contact, and off-axis deformations. Both materials engineering and structural design approaches have been explored to achieve these properties. For instance, environmental effects can be mitigated through materials engineering, such as using near-zero TCR sensing materials for temperature insensitivity and superhydrophobic surface modifications to repel moisture. Different sensor designs have been developed to reduce the impact of off-axis

mechanical deformations, including the use of stiff islands for strain-insensitive pressure sensors and serpentine or meander structures to lower local stress, making strain sensors less sensitive to pressure, bending, and torsion. Additionally, making materials fibrous or porous helps mitigate unwanted effects from bending or strain by transforming the strain into local rotations that distribute stress more evenly. Despite these advancements, several challenges and limitations remain in achieving sensor insensitivity and specificity through material and structural design (**Figure 17**):

1. Electromechanical sensors face limitations in stable performance under harsh conditions (e.g., temperatures below 0 °C or exceeding several hundred degrees Celsius). Current near-zero TCR methods enable stability mostly below 100 °C, suitable for normal conditions (see Tables 3 and 4). Further optimization of material ratios is needed to reduce TCR for higher-temperature applications. Additionally, the focus should extend to insulating matrices that remain stretchable and stable at low temperatures, which often make substrates brittle.

2. These sensors typically operate within a limited strain range, often below 10% or even 1% (Table 4). This is due to the difficulty in maintaining a balance of resistance between fillers and substrates under higher strains. Substrates like epoxy, PI, and ceramics offer temperature stability due to their low CTE, but they are not ideal for stretchability. Future work should focus on developing stretchable substrates with low CTE or utilizing stretchable designs, such as serpentine patterns, to extend the sensing range.

3. While superhydrophobic surfaces can repel liquids, further research is needed to ensure stable performance in humid environments, where smaller molecules could penetrate and interfere with conductive sensing materials.

4. Ultrathin sensors or those incorporating stiff islands are effective but often complicate the fabrication process. Further research into anisotropic materials that are sensitive only to compression in one direction, along with simpler designs that reduce the need for integrated stiff materials, could improve the ease of manufacturing such sensors.

5. Torsion can affect the performance of pressure sensors, yet it is rarely addressed. Further studies should investigate this type of deformation, with suggestions to use structures like serpentine patterns to reduce stress concentrations and mitigate torsional effects.

6. For strain sensors, using low local stress structures like serpentine or meander designs can improve insensitivity to pressure, torsion, and bending, but this comes with a trade-off between sensitivity and sensing range (Table 4). High sensitivity requires initial contact, limiting the sensing range, while lower sensitivity extends the range due to reduced local stress. Optimizing these designs to balance stress concentration could improve sensitivity without sacrificing range.

7. Strain sensors with directional specificity generally have a low sensing range (below 40%) (Table 4), due to the anisotropic properties of materials, where high stress or disconnections occur in the parallel (working) direction. More stable material connections in the working direction could improve this trade-off between specificity and sensing range.

8. Creating strain sensors that respond exclusively to one stretching direction remains a challenge. Current research typically compares the sensitivity between parallel and perpendicular directions, but sensors still exhibit some response in the intermediate directions between the two. Future material exploration is needed to develop truly unidirectional sensors.

9. Despite various approaches to achieve sensor insensitivity, fully specific sensors remain elusive. This gap is due to a lack of attention to combining different approaches. Future research should aim to develop sensors that combine insensitivity to temperature, humidity, and mechanical deformations. For example, a fully specific strain sensor could be fabricated by coating stretchable substrates with two opposing TCR materials, applying low surface energy materials for humidity insensitivity, and using serpentine or meander designs to reduce off-axis deformation sensitivity.

This review provides valuable insights into the development and commercialization of electromechanical sensors for health monitoring systems. By summarizing and categorizing various material and structural design strategies to minimize undesirable interferences, it offers a systematic understanding that facilitates the development of highly specific sensors. The research gaps identified in this review can guide future efforts in creating sensors that accurately monitor human body signals, an important advancement for personalized health management systems. These systems, incorporating sensors, AI-based disease prediction, and wireless transmission technologies, hold the potential to revolutionize healthcare by enabling more accurate, stable, and reliable health monitoring.

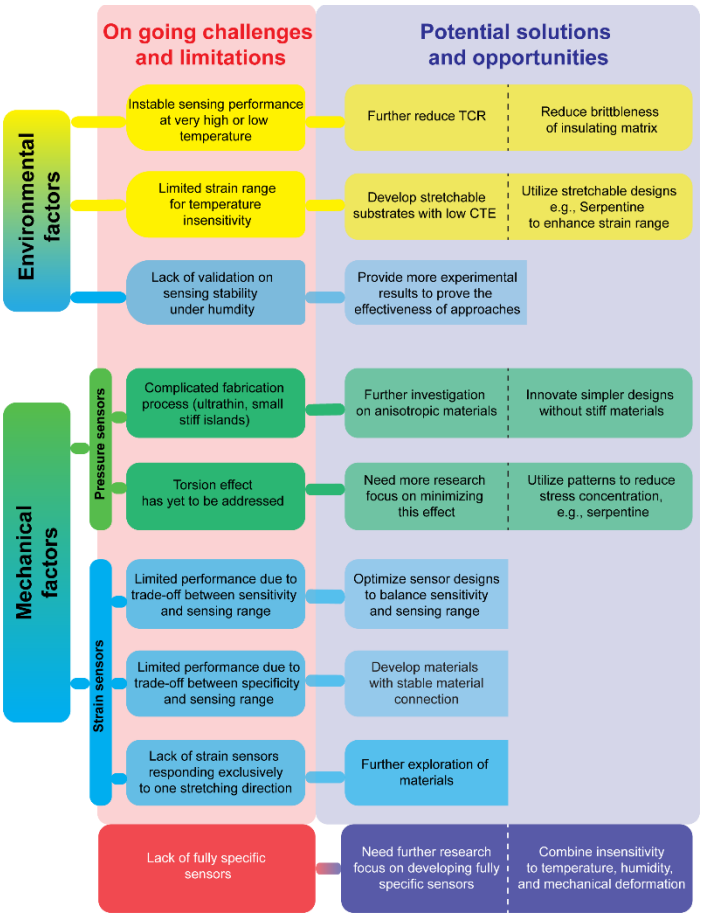

Figure 17. Summarization of ongoing challenges, limitations, opportunities, and the corresponding potential solutions for enhancing sensor specificity.

AUTHOR INFORMATION

Corresponding Author

Duy Van Nguyen. Email: duyvan.nguyen@unisq.edu.au

Jun Chen. Email: jun.chen@ucla.edu

Toan Dinh. Email: toan.dinh@unisq.edu.au

Author Contributions

The manuscript was written through contributions of all authors. All authors have given approval to the final version of the manuscript.

Funding Sources

Queensland Department of Environment, Science and Innovation (Q2032010)

Notes

The authors declare no competing financial interest.

ACKNOWLEDGMENT

This research received support from the Australian Government Research Training Program (RTP) Scholarship. T. Dinh acknowledges the support from State of Queensland: Queensland Department of Environment, Science and Innovation (Q2032010).

VOCABULARY

Electromechanical sensors: Sensors that convert mechanical deformations, such as pressure or strain, into electrical signals, like changes in resistance, voltage, or capacitance.

n(or p)-TCR supporting matrices: Insulating substrates that, when combined with conductive materials having a positive temperature coefficient of resistance (p-TCR) or negative temperature coefficient of resistance (n-TCR), can induce near-zero TCR conductive composites.

Superhydrophobicity: A phenomenon where a surface exhibits extreme water repellency. Water droplets on these surfaces maintain a nearly spherical shape, leading to minimal adhesion and allowing the droplets to easily roll off, even at very small tilt angles.

Off-axis deformations: Deformations in unintended directions imposed on electromechanical sensors during operation.

Mechanical mismatch: A mechanical condition between two materials with different mechanical properties, such as Young's modulus. When these materials are subjected to mechanical forces, their differing responses to stress or strain can lead to local stress concentrations.

REFERENCES

1. Luo, Y. F.; Abidian, M. R.; Ahn, J. H.; Akinwande, D.; Andrews, A. M.; Antonietti, M.; Bao, Z. N.; Berggren, M.; Berkey, C. A.; Bettinger, C. J.; Chen, J.; Chen, P.; Cheng, W. L.; Cheng, X.; Choi, S. J.; Chortos, A.; Dagdeviren, C.; Dauskardt, R. H.; Di, C. A.; Dickey, M. D., et al., Technology Roadmap for Flexible Sensors. *Acs Nano.* **2023,** *17*, 5211-5295.

2. Dai, N.; Lei, I. M.; Li, Z. Y.; Li, Y.; Fang, P.; Zhong, J. W., Recent advances in wearable electromechanical sensors-Moving towards machine learning-assisted wearable sensing systems. *Nano Energy.* **2023,** *105,* 108041.

3. Hegde, C.; Su, J. T.; Tan, J. M. R.; He, K.; Chen, X. D.; Magdassi, S., Sensing in Soft Robotics. *Acs Nano.* **2023,** *17*, 15277-15307.

4. Bai, Y.; Yin, L.; Hou, C.; Zhou, Y.; Zhang, F.; Xu, Z.; Li, K.; Huang, Y., Response regulation for epidermal fabric strain sensors via mechanical strategy. *Adv Funct Mater.* **2023,** *33*, 2214119.

5. Gong, S.; Yap, L. W.; Zhu, B. W.; Cheng, W. L., Multiscale Soft-Hard Interface Design for Flexible Hybrid Electronics. *Adv Mater.* **2020,** *32,* 1902278.

6. Liu, S. Y.; Rao, Y. F.; Jang, H.; Tan, P.; Lu, N. S., Strategies for body-conformable electronics. *Matter-Us.* **2022,** *5*, 1104-1136.

7. Zhu, G. D.; Hou, Y.; Xia, N.; Wang, X.; Zhang, C.; Zheng, J. Z.; Jin, D. D.; Zhang, L., Fully Recyclable, Healable, Soft, and Stretchable Dynamic Polymers for Magnetic Soft Robots. *Adv Funct Mater.* **2023,** *33,* 2300888.

8. Gong, S.; Zhang, X.; Nguyen, X. A.; Shi, Q.; Lin, F.; Chauhan, S.; Ge, Z.; Cheng, W., Hierarchically resistive skins as specific and multimetric on-throat wearable biosensors. *Nat Nanotechnol.* **2023,** *18*, 889-897.

9. Hu, X.; Wu, M.; Che, L.; Huang, J.; Li, H.; Liu, Z.; Li, M.; Ye, D.; Yang, Z.; Wang, X.; Xie, Z.; Liu, J., Nanoengineering Ultrathin Flexible Pressure Sensor with Superior Sensitivity and Perfect Conformability. *Small.* **2023**, 2208015.

10. Boutry, C. M.; Kaizawa, Y.; Schroeder, B. C.; Chortos, A.; Legrand, A.; Wang, Z.; Chang, J.; Fox, P.; Bao, Z. N., A stretchable and biodegradable strain and pressure sensor for orthopaedic application. *Nat Electron.* **2018,** *1*, 314-321.

11. Lee, S.; Franklin, S.; Hassani, F. A.; Yokota, T.; Nayeem, M. O. G.; Wang, Y.; Leib, R.; Cheng, G.; Franklin, D. W.; Someya, T., Nanomesh pressure sensor for monitoring finger manipulation without sensory interference. *Science.* **2020,** *370*, 966-970.

12. Lee, Y.; Park, J.; Cho, S.; Shin, Y. E.; Lee, H.; Kim, J.; Myoung, J.; Cho, S.; Kang, S.; Baig, C.; Ko, H., Flexible Ferroelectric Sensors with Ultrahigh Pressure Sensitivity and Linear Response over Exceptionally Broad Pressure Range. *Acs Nano.* **2018,** *12*, 4045-4054.

13. Meng, K. Y.; Xiao, X.; Wei, W. X.; Chen, G. R.; Nashalian, A.; Shen, S.; Chen, J., Wearable Pressure Sensors for Pulse Wave Monitoring. *Adv Mater.* **2022,** *34,* 2109357.

14. Gao, Y.; Xiao, T.; Li, Q.; Chen, Y.; Qiu, X. L.; Liu, J. W.; Bian, Y. Q.; Xuan, F. Z., Flexible microstructured pressure sensors: design, fabrication and applications. *Nanotechnology.* **2022,** *33,* 322002.

15. Duan, L. Y.; D'hooge, D. R.; Cardon, L., Recent progress on flexible and stretchable piezoresistive strain sensors: From design to application. *Prog Mater Sci.* **2020,** *114,* 100617.

16. Qin, J.; Yin, L. J.; Hao, Y. N.; Zhong, S. L.; Zhang, D. L.; Bi, K.; Zhang, Y. X.; Zhao, Y.; Dang, Z. M., Flexible and Stretchable Capacitive Sensors with Different Microstructures. *Adv Mater.* **2021,** *33,* 2008267.

17. Dinh, T.; Nguyen, T.; Phan, H. P.; Nguyen, T. K.; Dau, V.; Nguyen, N. T.; Dao, D. V., Advances in Rational Design and Materials of High-Performance Stretchable Electromechanical Sensors. *Small.* **2020,** *16,* 1905707.

18. Dinh, T.; Nguyen, T.; Phan, H. P.; Nguyen, N. T.; Dao, D. V.; Bell, J., Stretchable respiration sensors: Advanced designs and multifunctional platforms for wearable physiological monitoring. *Biosens Bioelectron.* **2020,** *166,* 112460.

19. Yang, R.; Dutta, A.; Li, B.; Tiwari, N.; Zhang, W.; Niu, Z.; Gao, Y.; Erdely, D.; Xin, X.; Li, T.; Cheng, H., Iontronic pressure sensor with high sensitivity over ultra-broad linear range enabled by laser-induced gradient micro-pyramids. *Nat Commun.* **2023,** *14*, 2907.

20. Hu, T.; Sheng, B., A Highly Sensitive Strain Sensor with Wide Linear Sensing Range Prepared on a Hybrid-Structured CNT/Ecoflex Film via Local Regulation of Strain Distribution. *Acs Appl Mater Inter.* **2024,** *16*, 21061-21072.

21. Pyo, S.; Lee, J.; Kim, W.; Jo, E.; Kim, J., Multi-layered, hierarchical fabric-based tactile sensors with high sensitivity and linearity in ultrawide pressure range. *Adv Funct Mater.* **2019,** *29*, 1902484.

22. Bai, N.; Wang, L.; Wang, Q.; Deng, J.; Wang, Y.; Lu, P.; Huang, J.; Li, G.; Zhang, Y.; Yang, J.; Xie, K.; Zhao, X.; Guo, C. F., Graded intrafillable architecture-based iontronic pressure sensor with ultra-broad-range high sensitivity. *Nat Commun.* **2020,** *11*, 209.

23. Xue, F.; Peng, Q.; Ding, R.; Li, P.; Zhao, X.; Zheng, H.; Xu, L.; Tang, Z.; Zhang, X.; He, X., Ultra-sensitive, highly linear, and hysteresis-free strain sensors enabled by gradient stiffness sliding strategy. *Npj Flex Electron.* **2024,** *8*, 14.

24. Zheng, Y.; Jin, Q.; Chen, W.; Sun, Y.; Wang, Z., High sensitivity and wide sensing range of stretchable sensors with conductive microsphere array structures. *J Mater Chem C.* **2019,** *7*, 8423-8431.

25. Chu, K.; Lee, S. C.; Lee, S.; Kim, D.; Moon, C.; Park, S. H., Smart conducting polymer composites having zero temperature coefficient of resistance. *Nanoscale.* **2015,** *7*, 471-478.

26. Luo, J. C.; Gao, S. J.; Luo, H.; Wang, L.; Huang, X. W.; Guo, Z.; Lai, X. J.; Lin, L. W.; Li, R. K. Y.; Gao, J. F., Superhydrophobic and breathable smart MXene-based textile for multifunctional wearable sensing electronics. *Chem Eng J.* **2021,** *406,* 126898.

27. Sarabia-Riquelme, R.; Schimpf, W. C.; Kuhn, D. L.; Weisenberger, M. C., Influence of relative humidity on the structure, swelling and electrical conductivity of PEDOT: PSS fibers. *Synthetic Metals.* **2023,** *297*, 117399.

28. Nguyen, V.; Yang, R., Effect of humidity and pressure on the triboelectric nanogenerator. *Nano Energy.* **2013,** *2*, 604-608.

29. Chen, X. X.; Yin, Z. Z.; Deng, Y. T.; Li, Z. H.; Xue, M. S.; Chen, Y. H.; Xie, Y.; Liu, W. Q.; He, P.; Luo, Y. D.; Hong, Z.; Xie, C., Harsh environment-tolerant and robust superhydrophobic graphene-based composite membrane for wearable strain sensor. *Sensor Actuat a-Phys.* **2023,** *362,* 114630.

30. Xie, F. J.; Lu, F.; Tian, Y.; Zhang, X.; Wang, Y. Q.; Zheng, L. Q.; Gao, X. P., Thermochromic-based bimodal sensor for strain-insensitive temperature sensing and synchronous strain sensing. *Chem Eng J.* **2023,** *471,* 144504.

31. Zhang, Y.; Liu, S.; Miao, Y.; Yang, H.; Chen, X.; Xiao, X.; Jiang, Z.; Chen, X.; Nie, B.; Liu, J., Highly stretchable and sensitive pressure sensor array based on icicle-shaped liquid metal film electrodes. *Acs Appl Mater Inter.* **2020,** *12*, 27961-27970.

32. Bai, Z.; Wang, X.; Huang, M.; Li, J.; Sun, S.; Zou, X.; Xie, L.; Wang, X.; Xue, P.; Feng, Y.; Huo, P.; Yue, O.; Liu, X., Robust integration of "top-down" strategy and triple-structure design for nature-skin derived e-skin with superior elasticity and ascendency strain and vibration sensitivity. *Nano Energy.* **2024,** *120*, 109142.

33. Huang, J.; Chen, A.; Han, S.; Wu, Q.; Zhu, J.; Zhang, J.; Chen, Y.; Liu, J.; Guan, L., Tough and Robust Mechanically Interlocked Gel–Elastomer Hybrid Electrode for Soft Strain Gauge. *Adv Sci.* **2023,** *10*, 2301116.

34. Fang, Y. S.; Zou, Y. J.; Xu, J.; Chen, G. R.; Zhou, Y. H.; Deng, W. L.; Zhao, X.; Roustaei, M.; Hsiai, T. K.; Chen, J., Ambulatory Cardiovascular Monitoring Via a Machine-Learning-Assisted Textile Triboelectric Sensor. *Adv Mater.* **2021,** *33,* 2104178.

35. Wang, Y.; Zhang, C.; Meng, X.; Zhang, Q.; Li, H.; Chen, F.; Yang, Q.; Zhang, W.; Zheng, Y.; Chen, S., Quantitative and Real-Time Evaluation of Pressure on Brain Spatula with Wireless and Compact Sensing System. *Adv Funct Mater.* **2023,** *33*, 2210596.

36. Zhou, Q.; Lee, K.; Kim, K. N.; Park, J. G.; Pan, J.; Bae, J.; Baik, J. M.; Kim, T., High humidity-and contamination-resistant triboelectric nanogenerator with superhydrophobic interface. *Nano Energy.* **2019,** *57*, 903-910.

37. Wang, X.; Zhou, J.; Zhu, Y.; Cheng, W.; Zhao, D.; Xu, G.; Yu, H., Assembly of silver nanowires and PEDOT: PSS with hydrocellulose toward highly flexible, transparent and conductivity-stable conductors. *Chem Eng J.* **2020,** *392*, 123644.

38. Fu, M.; Zhang, J. M.; Jin, Y. M.; Zhao, Y.; Huang, S. Y.; Guo, C. F., A Highly Sensitive, Reliable, and High-Temperature-Resistant Flexible Pressure Sensor Based on Ceramic Nanofibers. *Adv Sci.* **2020,** *7,* 2000258.

39. Su, Q.; Zou, Q.; Li, Y.; Chen, Y. Z.; Teng, S. Y.; Kelleher, J. T.; Nith, R.; Cheng, P.; Li, N.; Liu, W.; Dai, S. L.; Liu, Y. D.; Mazursky, A.; Xu, J.; Jin, L. H.; Lopes, P.; Wang, S. H., A stretchable and strain-unperturbed pressure sensor for motion interference-free tactile monitoring on skins. *Sci Adv.* **2021,** *7,* eabi4563.

40. Qiao, H. Y.; Sun, S. T.; Wu, P. Y., Non-equilibrium-Growing Aesthetic Ionic Skin for Fingertip-Like Strain-Undisturbed Tactile Sensation and Texture Recognition. *Adv Mater.* **2023,** *35,* 2300593.

41. Kim, K. K.; Hong, S.; Cho, H. M.; Lee, J.; Suh, Y. D.; Ham, J.; Ko, S. H., Highly Sensitive and Stretchable Multidimensional Strain Sensor with Prestrained Anisotropic Metal Nanowire Percolation Networks. *Nano Lett.* **2015,** *15*, 5240-5247.

42. Yang, G.; Tang, X. C.; Zhao, G. D.; Li, Y. F.; Ma, C. Q.; Zhuang, X. P.; Yan, J., Highly sensitive, direction-aware, and transparent strain sensor based on oriented electrospun nanofibers for wearable electronic applications. *Chem Eng J.* **2022,** *435,* 135004.

43. Lee, J. H.; Kim, J.; Liu, D.; Guo, F. M.; Shen, X.; Zheng, Q. B.; Jeon, S.; Kim, J. K., Highly Aligned, Anisotropic Carbon Nanofiber Films for Multidirectional Strain Sensors with Exceptional Selectivity. *Adv Funct Mater.* **2019,** *29,* 1901623.

44. Araromi, O. A.; Graule, M. A.; Dorsey, K. L.; Castellanos, S.; Foster, J. R.; Hsu, W.-H.; Passy, A. E.; Vlassak, J. J.; Weaver, J. C.; Walsh, C. J.; Wood, R. J., Ultra-sensitive and resilient compliant strain gauges for soft machines. *Nature.* **2020,** *587*, 219-224.

45. Liang, B. H.; Lin, Z. Q.; Chen, W. J.; He, Z. F.; Zhong, J.; Zhu, H.; Tang, Z. K.; Gui, X. C., Ultra-stretchable and highly sensitive strain sensor based on gradient structure carbon nanotubes. *Nanoscale.* **2018,** *10*, 13599-13606.

46. Xie, Y. X.; Wu, X. H.; Huang, X. B.; Liang, Q. H.; Deng, S. P.; Wu, Z. J.; Yao, Y. P.; Lu, L. S., A Deep Learning-Enabled Skin-Inspired Pressure Sensor for Complicated Recognition Tasks with Ultralong Life. *Research.* **2023,** *6,* 0157.

47. Zhang, J. Z.; Liu, J.; Zhao, Z. Y.; Sun, W. W.; Zhao, G. J.; Liu, J. G.; Xu, J. C.; Li, Y. L.; Liu, Z. K.; Li, Y.; Li, G., Fiber-Based Sensitivity-Tunable Strain Sensors with Insensitive Response to Wearable Microclimate Changes. *Adv Fiber Mater.* **2023,** *5*, 1378-1391.

48. Ding, Y.-R.; Xue, C.-H.; Fan, Q.-Q.; Zhao, L.-L.; Tian, Q.-Q.; Guo, X.-J.; Zhang, J.; Jia, S.-T.; An, Q.-F., Fabrication of superhydrophobic conductive film at air/water interface for flexible and wearable sensors. *Chem Eng J.* **2021,** *404*, 126489.

49. He, W.; Li, G.; Zhang, S.; Wei, Y.; Wang, J.; Li, Q.; Zhang, X., Polypyrrole/silver coaxial nanowire aero-sponges for temperature-independent stress sensing and stress-triggered joule heating. *Acs Nano.* **2015,** *9*, 4244-4251.

50. Li, M. F.; Chen, J. X.; Zhong, W. B.; Luo, M. Y.; Wang, W.; Qing, X.; Lu, Y.; Liu, Q. Z.; Liu, K.; Wang, Y. D.; Wang, D., Large-Area, Wearable, Self-Powered Pressure-Temperature Sensor Based on 3D Thermoelectric Spacer Fabric. *Acs Sensors.* **2020,** *5*, 2545-2554.

51. Chu, Z. M.; Jiao, W. C.; Li, J.; Guo, H. Y.; Zheng, Y. T.; Wang, R. G.; He, X. D., A novel wrinkle-gradient strain sensor with anti-water interference and high sensing performance. *Chem Eng J.* **2021,** *421,* 129873.

52. Luo, S. D.; Liu, T., SWCNT/Graphite Nanoplatelet Hybrid Thin Films for Self-Temperature- Compensated, Highly Sensitive, and Extensible Piezoresistive Sensors. *Adv Mater.* **2013,** *25*, 5650-5657.

53. Wu, C.; Lin, F.; Pan, X. C.; Zeng, Y. J.; Chen, G. C.; Xu, L. D.; He, Y. P.; He, G. H.; Chen, Q. N.; Sun, D. H.; Hai, Z. Y., Temperature-insensitive conductive composites for noninterference strain sensing. *Chem Eng J.* **2023,** *457,* 141269.

54. Han, S. B.; Jiao, F.; Khan, Z. U.; Edberg, J.; Fabiano, S.; Crispin, X., Thermoelectric Polymer Aerogels for Pressure-Temperature Sensing Applications. *Adv Funct Mater.* **2017,** *27,* 1703549.

55. Lin, J.; Cai, X.; Liu, Z.; Liu, N.; Xie, M.; Zhou, B.; Wang, H.; Guo, Z., Anti-liquid-interfering and bacterially antiadhesive strategy for highly stretchable and ultrasensitive strain sensors based on Cassie-Baxter wetting state. *Adv Funct Mater.* **2020,** *30*, 2000398.

56. Liu, H.; Li, Q.; Bu, Y.; Zhang, N.; Wang, C.; Pan, C.; Mi, L.; Guo, Z.; Liu, C.; Shen, C., Stretchable conductive nonwoven fabrics with self-cleaning capability for tunable wearable strain sensor. *Nano Energy.* **2019,** *66*, 104143.

57. Lee, S.; Reuveny, A.; Reeder, J.; Lee, S.; Jin, H.; Liu, Q. H.; Yokota, T.; Sekitani, T.; Isoyama, T.; Abe, Y.; Suo, Z. G.; Someya, T., A transparent bending-insensitive pressure sensor. *Nat Nanotechnol.* **2016,** *11*, 472-478.

58. Wang, H.; Rao, Z. C.; Liu, Y. Q.; Shan, L. T.; Guo, T. L.; Chen, H. P.; Wang, R., A highly stretchable triboelectric nanogenerator with both stretch-insensitive sensing and stretch-sensitive sensing. *Nano Energy.* **2023,** *107,* 108170.

59. Liu, Z. K.; Zheng, Y.; Jin, L.; Chen, K. L.; Zhai, H.; Huang, Q. Y.; Chen, Z. D.; Yi, Y. P.; Umar, M.; Xu, L. L.; Li, G.; Song, Q. W.; Yue, P. F.; Li, Y.; Zheng, Z. J., Highly Breathable and Stretchable Strain Sensors with Insensitive Response to Pressure and Bending. *Adv Funct Mater.* **2021,** *31,* 2007622.

60. Park, T.; Woo, H. K.; Jung, B. K.; Park, B.; Bang, J.; Kim, W.; Jeon, S.; Ahn, J.; Lee, Y.; Lee, Y. M.; Kim, T. I.; Oh, S. J., Noninterference Wearable Strain Sensor: Near-Zero Temperature Coefficient of Resistance Nanoparticle Arrays with Thermal Expansion and Transport Engineering. *Acs Nano.* **2021,** *15*, 8120-8129.

61. Park, Y.-J.; Lee, S.; Kim, B.; Kim, J.-H.; So, J.-H.; Koo, H.-J., Impedance study on humidity dependent conductivity of polymer composites with conductive nanofillers. *Composites Part B: Engineering.* **2020,** *202*, 108412.

62. Popov, V.; Nikolaev, D.; Timofeev, V.; Smagulova, S.; Antonova, I., Graphene-based humidity sensors: The origin of alternating resistance change. *Nanotechnology.* **2017,** *28*, 355501.

63. Daoud, W. A.; Xin, J. H.; Szeto, Y. S., Polyethylenedioxythiophene coatings for humidity, temperature and strain sensing polyamide fibers. *Sensors and Actuators B: Chemical.* **2005,** *109*, 329-333.

64. Yao, Y.; Chen, X.; Zhu, J.; Zeng, B.; Wu, Z.; Li, X., The effect of ambient humidity on the electrical properties of graphene oxide films. *Nanoscale Res Lett.* **2012,** *7*, 1-7.

65. Niu, S. C.; Chang, X. T.; Zhu, Z. H.; Qin, Z. W.; Li, J. F.; Jiang, Y. C.; Wang, D. S.; Yang, C. X.; Gao, Y.; Sun, S. B., Low-Temperature Wearable Strain Sensor Based on a Silver Nanowires/Graphene Composite with a Near-Zero Temperature Coefficient of Resistance. *Acs Appl Mater Inter.* **2021,** *13*, 55307–55318.

66. Dong, Y.; Chang, J.; Zhao, J.; Hou, X.; Yuan, X. B., Wearable anti-temperature interference pressure sensor with ridge-like interlocking microstructures. *J Mater Sci-Mater El.* **2023,** *34,* 835.

67. Li, G. R.; Wong, T. W.; Shih, B.; Guo, C. Y.; Wang, L. W.; Liu, J. Q.; Wang, T.; Liu, X. B.; Yan, J. Y.; Wu, B. S.; Yu, F. J.; Chen, Y. S.; Liang, Y. M.; Xue, Y. T.; Wang, C. J.; He, S. P.; Wen, L.; Tolley, M. T.; Zhang, A. M.; Laschi, C., et al., Bioinspired soft robots for deep-sea exploration. *Nat Commun.* **2023,** *14,* 7097.

68. Gong, S.; Schwalb, W.; Wang, Y. W.; Chen, Y.; Tang, Y.; Si, J.; Shirinzadeh, B.; Cheng, W. L., A wearable and highly sensitive pressure sensor with ultrathin gold nanowires. *Nat Commun.* **2014,** *5,* 3132.

69. Lian, Y. L.; Yu, H.; Wang, M. Y.; Yang, X. N.; Zhang, H. F., Ultrasensitive Wearable Pressure Sensors Based on Silver Nanowire-Coated Fabrics. *Nanoscale Res Lett.* **2020,** *15,* 70.

70. He, J.; Xiao, P.; Lu, W.; Shi, J. W.; Zhang, L.; Liang, Y.; Pan, C. F.; Kuo, S. W.; Chen, T., A Universal high accuracy wearable pulse monitoring system via high sensitivity and large linearity graphene pressure sensor. *Nano Energy.* **2019,** *59*, 422-433.

71. Zhang, Z. M.; Zhang, Y. X.; Jiang, X.; Bukhari, H.; Zhang, Z. X.; Han, W. H.; Xie, E. Q., Simple and efficient pressure sensor based on PDMS wrapped CNT arrays. *Carbon.* **2019,** *155*, 71-76.

72. Gong, S.; Wu, D.; Li, Y. X.; Jin, M. Y.; Xiao, T.; Wang, Y.; Xiao, Z.; Zhu, Z. H.; Li, Z., Temperature-independent piezoresistive sensors based on carbon nanotube/polymer nanocomposite. *Carbon.* **2018,** *137*, 188-195.

73. Meng, X. Y.; Mo, L. X.; Han, S. B.; Zhao, J.; Pan, Y. Q.; Wang, F. D.; Fang, Y.; Li, L. H., Pressure-Temperature Dual-Parameter Flexible Sensors Based on Conformal Printing of Conducting Polymer PEDOT:PSS on Microstructured Substrate. *Adv Mater Interfaces.* **2023,** *10*.

74. Choi, Y. K.; Kim, T. H.; Song, J. H.; Jung, B. K.; Kim, W.; Bae, J. H.; Choi, H. J.; Kwak, J.; Shim, J. W.; Oh, S. J., Charge transport transition of PEDOT:PSS thin films for temperature-insensitive wearable strain sensors. *Nanoscale.* **2023,** *15*, 7980-7990.

75. Pan, L. J.; Chortos, A.; Yu, G. H.; Wang, Y. Q.; Isaacson, S.; Allen, R.; Shi, Y.; Dauskardt, R.; Bao, Z. N., An ultra-sensitive resistive pressure sensor based on hollow-sphere microstructure induced elasticity in conducting polymer film. *Nat Commun.* **2014,** *5*, 3002.

76. Shivaprasad, S.; Angadi, M.; Udachan, L., Temperature coefficient of resistance of thin manganese films. *Thin Solid Films.* **1980,** *71*, L1-L4.

77. Shivaprasad, S.; Angadi, M., Temperature coefficient of resistance of thin palladium films. *Journal of Physics D: Applied Physics.* **1980,** *13*, L171.

78. Marin, B. C.; Root, S. E.; Urbina, A. D.; Aklile, E.; Miller, R.; Zaretski, A. V.; Lipomi, D. J., Graphene-Metal Composite Sensors with Near-Zero Temperature Coefficient of Resistance. *Acs Omega.* **2017,** *2*, 626-630.

79. Dehghani, S.; Moravvej-Farshi, M. K.; Sheikhi, M. H., Temperature Dependence of Electrical Resistance of Individual Carbon Nanotubes and Carbon Nanotubes Network. *Mod Phys Lett B.* **2012,** *26,* 1250136.

80. Gong, S.; Zhu, Z. H.; Li, Z., Electron tunnelling and hopping effects on the temperature coefficient of resistance of carbon nanotube/polymer nanocomposites. *Phys Chem Chem Phys.* **2017,** *19*, 5113-5120.

81. Geim, A. K.; Novoselov, K. S., The rise of graphene. *Nat Mater.* **2007,** *6*, 183-191.

82. Bubnova, O.; Khan, Z. U.; Wang, H.; Braun, S.; Evans, D. R.; Fabretto, M.; Hojati-Talemi, P.; Dagnelund, D.; Arlin, J. B.; Geerts, Y. H.; Desbief, S.; Breiby, D. W.; Andreasen,

J. W.; Lazzaroni, R.; Chen, W. M. M.; Zozoulenko, I.; Fahlman, M.; Murphy, P. J.; Berggren, M.; Crispin, X., Semi-metallic polymers. *Nat Mater.* **2014,** *13*, 190-194.

83. Yee, S. K.; Coates, N. E.; Majumdar, A.; Urban, J. J.; Segalman, R. A., Thermoelectric power factor optimization in PEDOT:PSS tellurium nanowire hybrid composites. *Phys Chem Chem Phys.* **2013,** *15*, 4024-4032.

84. Gao, Z.; Jiang, K.; Lou, Z.; Han, W.; Shen, G., Water-proof and thermally inert flexible pressure sensors based on zero temperature coefficient of resistance hybrid films. *J Mater Chem C.* **2019,** *7*, 9648-9654.

85. Yao, H. C.; Li, P. J.; Cheng, W.; Yang, W. D.; Yang, Z. J.; Ali, H. P. A.; Guo, H. C.; Tee, B. C. K., Environment-Resilient Graphene Vibrotactile Sensitive Sensors for Machine Intelligence. *Acs Mater Lett.* **2020,** *2*, 986-992.

86. Wen, M.; Guan, X. C.; Li, H.; Ou, J. P., Temperature characteristics of thick-film resistors and its application as a strain sensor with low temperature-sensitivity. *Sensor Actuat a-Phys.* **2020,** *301,* 111779.

87. Kato, Y.; Fukuda, K.; Someya, T.; Yokota, T., An ultra-flexible temperature-insensitive strain sensor. *J Mater Chem C.* **2023,** *11*, 14070-14078.

88. Huo, P. P.; Cebe, P.; Capel, M., Real-Time X-Ray-Scattering Study of Thermal-Expansion of Poly(Butylene Terephthalate). *J Polym Sci Pol Phys.* **1992,** *30*, 1459-1468.

89. Numata, S.; Oohara, S.; Fujisaki, K.; Imaizumi, J.; Kinjo, N., Thermal-Expansion Behavior of Various Aromatic Polyimides. *J Appl Polym Sci.* **1986,** *31*, 101-110.

90. Hong, E. Y.; Lee, S. H.; Lee, D. K.; Choi, S. S.; Baek, K. Y.; Hwang, S. S.; Kwon, O. P., Polyaniline films doped with ladder-type sulfonated polyphenylsilsesquioxane and unusual dependence of their electrical conductivity on temperature. *J Mater Chem.* **2012,** *22*, 18151-18155.

91. Wang, Y. L.; Mao, H. Y.; Wang, Y.; Zhu, P. C.; Liu, C. H.; Deng, Y., 3D geometrically structured PANI/CNT-decorated polydimethylsiloxane active pressure and temperature dual-parameter sensors for man-machine interaction applications. *J Mater Chem A.* **2020,** *8*, 15167-15176.

92. Niu, S. C.; He, S. Y.; Chen, Y.; Zhu, Z. H.; Chang, X. T.; Yang, C. X.; Li, J. F.; Jiang, Y. C.; Wang, D. S.; Zhu, Y. Q.; Sun, S. B., 3D Printing Assisted-Fabrication of Low-Temperature Strain Sensors with Large Working Range and Outstanding Stability. *Adv Mater Technol.* **2023,** *8,* 2300867.

93. Wu, C.; He, Y. P.; Li, L. L.; Chen, G. C.; Fu, Y. Z.; Zeng, Y. J.; Xu, L. D.; Lin, F.; Pan, X. C.; Chen, Q. N.; Zhao, Y.; Sun, D. H.; Hai, Z. Y., Temperature-Independent Conductive Ceramic for High-Temperature Strain-Sensing Applications. *Adv Eng Mater.* **2023**, *25*, 2300516.

94. Yuan, T. K.; Yin, R. L.; Li, C. W.; Fan, Z.; Pan, L. J., $Ti_3C_2T_x$ MXene-based all-resistive dual-mode sensor with near-zero temperature coefficient of resistance for crosstalk-free pressure and temperature detections. *Chem Eng J.* **2024,** *487*, 150396.

95. Lei, S.; Su, N. N.; Li, M. W., Thermal-Resistance Effect of Graphene at High Temperatures in Nanoelectromechanical Temperature Sensors. *Micromachines.* **2022,** *13*, 2078.

96. Kula, P.; Szymanski, W.; Kolodziejczyk, L.; Atraszkiewicz, R.; Dybowski, K.; Grabarczyk, J.; Pietrasik, R.; Niedzielski, P.; Kaczmarek, L.; Clapa, M., High Strength Metallurgical Graphene - Mechanisms of Growth and Properties. *Arch Metall Mater.* **2015,** *60*, 2535-2541.

97. Yin, Y. M.; Wang, Y. L.; Li, H. Y.; Xu, J.; Zhang, C.; Li, X.; Cao, J. W.; Feng, H. F.; Zhu, G., A flexible dual parameter sensor with hierarchical porous structure for fully decoupled pressure-temperature sensing. *Chem Eng J.* **2022,** *430*, 133158.

98. Wang, Y.; Wu, H. T.; Xu, L.; Zhang, H. N.; Yang, Y.; Wang, Z. L., Hierarchically patterned self-powered sensors for multifunctional tactile sensing. *Sci Adv.* **2020,** *6*, eabb9083.

99. Zhang, F.; Zang, Y.; Huang, D.; Di, C.-a.; Zhu, D., Flexible and self-powered temperature–pressure dual-parameter sensors using microstructure-frame-supported organic thermoelectric materials. *Nat Commun.* **2015,** *6*, 8356.

100. Wang, N.; Xia, Z. P.; Yang, S. K.; Pan, J. J.; Lei, T. D.; Qiao, W.; Wu, L. W., Pressure-temperature dual-parameter sensors designed by wood-derived thermoelectric composites: Micro-pressure high sensitivity. *Compos Part B-Eng.* **2023,** *264*, 110928.

101. Li, R. Q.; Zhou, Q.; Bi, Y.; Cao, S. J.; Xia, X.; Yang, A. L.; Li, S. M.; Xiao, X. L., Research progress of flexible capacitive pressure sensor for sensitivity enhancement approaches. *Sensor Actuat a-Phys.* **2021,** *321*, 112425.

102. Guo, L. A.; Wu, G. T.; Wang, Q. Y.; Li, T.; Yao, B. H.; Zou, Y. J.; Xu, M. Y., Advances in triboelectric pressure sensors. *Sensor Actuat a-Phys.* **2023,** *355*, 114331.

103. Cheng, T.; Shao, J.; Wang, Z. L., Triboelectric nanogenerators. *Nature Reviews Methods Primers.* **2023,** *3*, 39.

104. Huang, Y. C.; Liu, Y.; Ma, C.; Cheng, H. C.; He, Q. Y.; Wu, H.; Wang, C.; Lin, C. Y.; Huang, Y.; Duan, X. F., Sensitive pressure sensors based on conductive microstructured air-gap gates and two-dimensional semiconductor transistors. *Nat Electron.* **2020,** *3*, 59-69.

105. Yang, J. C.; Kim, J. O.; Oh, J.; Kwon, S. Y.; Sim, J. Y.; Kim, D. W.; Choi, H. B.; Park, S., Microstructured Porous Pyramid-Based Ultrahigh Sensitive Pressure Sensor Insensitive to Strain and Temperature. *Acs Appl Mater Inter.* **2019,** *11*, 19472-19480.

106. Wu, R. H.; Ma, L. Y.; Hou, C.; Meng, Z. H.; Guo, W. X.; Yu, W. D.; Yu, R.; Hu, F.; Liu, X. Y., Silk Composite Electronic Textile Sensor for High Space Precision 2D Combo Temperature-Pressure Sensing. *Small.* **2019,** *15*, 1901558.

107. Wang, P.; Yu, W.; Li, G. X.; Meng, C. Z.; Guo, S. J., Printable, flexible, breathable and sweatproof bifunctional sensors based on an all-nanofiber platform for fully decoupled pressure-temperature sensing application. *Chem Eng J.* **2023,** *452*, 139174.

108. Mannsfeld, S. C. B.; Tee, B. C. K.; Stoltenberg, R. M.; Chen, C. V. H. H.; Barman, S.; Muir, B. V. O.; Sokolov, A. N.; Reese, C.; Bao, Z. N., Highly sensitive flexible pressure sensors with microstructured rubber dielectric layers. *Nat Mater.* **2010,** *9*, 859-864.

109. Bae, G. Y.; Han, J. T.; Lee, G.; Lee, S.; Kim, S. W.; Park, S.; Kwon, J.; Jung, S.; Cho, K., Pressure/Temperature Sensing Bimodal Electronic Skin with Stimulus Discriminability and Linear Sensitivity. *Adv Mater.* **2018,** *30*, 1803388.

110. Chen, L. Y., Temperature dependent dielectric properties of polycrystalline aluminum oxide substrates with various impurities. *Icept: 2007 8th International Conference on Electronics Packaging Technology, Proceedings.* **2007**, 421-421.

111. Fu, J., High and temperature-stable dielectric constants in PNb_9O_{25} ceramic. *J Am Ceram Soc.* **2022,** *105*, 3740-3745.

112. Luo, G. Q.; Zhang, G. R.; Zhang, Y.; Li, A.; Sun, Y.; Tu, R.; Shen, Q., Wide temperature range of stable dielectric properties in relaxor $BaTiO_3$-based ceramics by co-doping synergistic engineering. *Mater Chem Phys.* **2023,** *302*, 127629.

113. Deng, L. B.; Young, R. J.; Kinloch, I. A.; Sun, R.; Zhang, G. P.; Noé, L.; Monthioux, M., Coefficient of thermal expansion of carbon nanotubes measured by Raman spectroscopy. *Appl Phys Lett.* **2014,** *104*, 051907.

114. Jiang, H.; Liu, B.; Huang, Y.; Hwang, K. C., Thermal expansion of single wall carbon nanotubes. *J Eng Mater-T Asme.* **2004,** *126*, 265-270.

115. Müller, A.; Wapler, M. C.; Wallrabe, U., A quick and accurate method to determine the Poisson's ratio and the coefficient of thermal expansion of PDMS. *Soft Matter.* **2019,** *15*, 779-784.

116. Zulkifli, A., Polymer Dielectric Materials. In *Dielectric Material*, Marius Alexandru, S., Ed. IntechOpen: Rijeka, 2012; p Ch. 1.

117. Sheng, J. J.; Chen, H. L.; Li, B.; Wang, Y. Q., Influence of the temperature and deformation-dependent dielectric constant on the stability of dielectric elastomers. *J Appl Polym Sci.* **2013,** *128*, 2402-2407.

118. Xiao, Q.; Li, L.; Zhan, B. Q.; Chen, X. M., Polyvinylidene fluoride-modified $BaTiO_3$ composites with high dielectric constant and temperature stability. *Ceram Int.* **2013,** *39*, S3-S7.

119. Ai, D.; Chang, Y.; Liu, H. L.; Wu, C. L.; Zhou, Y.; Han, Y. T.; Yu, H.; Xiao, B.; Cheng, Y. H.; Wu, G. L.; Jia, Z. R., Dielectric nanocomposites with superb high-temperature capacitive performance based on high intrinsic dielectric constant polymer. *Nano Research.* **2024,** *17*, 8504-8512.

120. Li, X. T.; Zhang, P. Y.; Dong, J.; Gan, F.; Zhao, X.; Zhang, Q. H., Preparation of low-κ polyimide resin with outstanding stability of dielectric properties versus temperature by adding a reactive Cardo-containing diluent. *Compos Part B-Eng.* **2019,** *177*, 107401.

121. Pu, Z. J.; Xia, J. L.; Liu, X. Y.; Wang, Q.; Liu, J. Y.; He, X. H.; Zhong, J. C., Novel polyethersulfone dielectric films with high temperature resistance, intrinsic low dielectric constant and low dielectric loss. *J Mater Sci-Mater El.* **2021,** *32*, 967-976.

122. Xiao, Q.; Li, L.; Zhang, B. Q.; Chen, X. M., Polyvinylidene fluoride-modified BaTiO3 composites with high dielectric constant and temperature stability. *Ceram Int.* **2013,** *39*, S3-S7.

123. Thuau, D.; Kallitsis, K.; Ha, S.; Bargain, F.; Soulestin, T.; Pecastaings, G.; Tencé-Girault, S.; Dos Santos, F. D.; Hadziioannou, G., High and Temperature-Independent Dielectric Constant Dielectrics from PVDF-Based Terpolymer and Copolymer Blends. *Adv Electron Mater.* **2020,** *6*, 1901250.

124. Lu, C. X.; Han, C. B.; Gu, G. Q.; Chen, J.; Yang, Z. W.; Jiang, T.; He, C.; Wang, Z. L., Temperature Effect on Performance of Triboelectric Nanogenerator. *Adv Eng Mater.* **2017,** *19*, 1700275.

125. Xia, K. Q.; Zhu, Z. Y.; Zhang, H. Z.; Xu, Z. W., A triboelectric nanogenerator as self-powered temperature sensor based on PVDF and PTFE. *Appl Phys a-Mater.* **2018,** *124*, 520.

126. Shankaregowda, S. A.; Nanjegowda, C. B.; Guan, S. R.; Huang, J. Q.; Li, J. Y.; Ahmed, R. F. S. M.; Sannathammegowda, K.; Boregowda, A. M.; Wang, F.; Cheng, C., A Robust Triboelectric Nanogenerator Resistant to Humidity and Temperature in Ambient Environment. *Phys Status Solidi-R.* **2023,** *17*, 2200489.

127. Rao, J. H.; Chen, Z. T.; Zhao, D. N.; Ma, R.; Yi, W. Y.; Zhang, C. X.; Liu, D.; Chen, X.; Yang, Y. H.; Wang, X. F.; Wang, J.; Yin, Y. J.; Wang, X. F.; Yang, G. W.; Yi, F., Tactile electronic skin to simultaneously detect and distinguish between temperature and pressure based on a triboelectric nanogenerator. *Nano Energy.* **2020,** *75*, 105073.

128. Niu, S. M.; Wang, Z. L., Theoretical systems of triboelectric nanogenerators. *Nano Energy.* **2015,** *14*, 161-192.

129. Zhou, Y. S.; Wang, S. H.; Yang, Y.; Zhu, G.; Niu, S. M.; Lin, Z. H.; Liu, Y.; Wang, Z. L., Manipulating Nanoscale Contact Electrification by an Applied Electric Field. *Nano Lett.* **2014,** *14*, 1567-1572.

130. Lin, S. Q.; Xu, L.; Xu, C.; Chen, X. Y.; Wang, A. C.; Zhang, B. B.; Lin, P.; Yang, Y.; Zhao, H. B.; Wang, Z. L., Electron Transfer in Nanoscale Contact Electrification: Effect of Temperature in the Metal-Dielectric Case. *Adv Mater.* **2019,** *31*, 1808197.

131. Thirmal, C.; Nayek, C.; Murugavel, P.; Subramanian, V., Magnetic, dielectric and magnetodielectric properties of PVDF-$La_{0.7}Sr_{0.3}MnO_3$ polymer nanocomposite film. *Aip Adv.* **2013,** *3*, 112109.

132. Yadav, V. S.; Sahu, D. K.; Singh, Y.; Dhubkarya, D. C., The Effect of Frequency and Temperature on Dielectric Properties of Pure Poly Vinylidene Fluoride (PVDF) Thin Films. In *Lecture Notes in Engineering and Computer Science*, *Proceedings of The International MultiConference of Engineers and Computer Scientists 2010*, Kowloon, Hong Kong, March 17-19, 2010; Ao, S. I., Castillo, O., Douglas, C., Feng, D. D., Lee, J.A, Eds.; Publisher: Newswood Limited, 2010; Vol. III, pp 1593-1596.

133. Chen, Y. F.; Lei, H.; Gao, Z. Q.; Liu, J. Y.; Zhang, F. J.; Wen, Z.; Sun, X. H., Energy autonomous electronic skin with direct temperature-pressure perception. *Nano Energy.* **2022,** *98*, 107273.

134. Sharma, P. K.; Chung, J. Y., Evaluation of Polydimethylsiloxane (PDMS) as a Substrate for the Realization of Flexible/Wearable Antennas and Sensors. *Micromachines.* **2023,** *14*, 735.

135. Salmaz, U.; Islam, T.; Sohail, S., A Novel Linear Capacitive Temperature Sensor Using Polydimethylsiloxane. *Ieee T Instrum Meas.* **2020,** *69*, 7887-7894.

136. Xie, Y. M.; Cheng, Y. F.; Ma, Y. A.; Wang, J.; Zou, J. J.; Wu, H.; Yue, Y.; Li, B. W.; Gao, Y. H.; Zhang, X.; Nan, C. W., 3D MXene-Based Flexible Network for High-Performance Pressure Sensor with a Wide Temperature Range. *Adv Sci.* **2023,** *10*, 2205303.

137. Ma, J.; Liu, Q.; Yang, L.; Li, M.; Liu, Q.; Zhong, W.; Lu, Y.; Wang, Y.; Liu, X.; Wang, D., A Flexible, Highly Accurate, and Stable Pressure Sensor with Anti-Interference from Temperature, Sweat, and Humidity. *Adv Mater Interfaces.* **2023,** *10*, 2201528.

138. Zhu, T.; Ni, Y.; Zhao, K.; Huang, J.; Cheng, Y.; Ge, M.; Park, C.; Lai, Y., A breathable knitted fabric-based smart system with enhanced superhydrophobicity for drowning alarming. *Acs Nano.* **2022,** *16*, 18018-18026.

139. North, N. A.; MacLeod, I. D., Corrosion of metals. In *Conservation of marine archaeological objects*, Elsevier: 1987; pp 68-98.

140. Elechiguerra, J. L.; Larios-Lopez, L.; Liu, C.; Garcia-Gutierrez, D.; Camacho-Bragado, A.; Yacaman, M. J., Corrosion at the nanoscale: the case of silver nanowires and nanoparticles. *Chemistry of Materials.* **2005,** *17*, 6042-6052.

141. Jiu, J.; Wang, J.; Sugahara, T.; Nagao, S.; Nogi, M.; Koga, H.; Suganuma, K.; Hara, M.; Nakazawa, E.; Uchida, H., The effect of light and humidity on the stability of silver nanowire transparent electrodes. *Rsc Adv.* **2015,** *5*, 27657-27664.

142. Wehling, T.; Katsnelson, M.; Lichtenstein, A., Adsorbates on graphene: Impurity states and electron scattering. *Chemical Physics Letters.* **2009,** *476*, 125-134.

143. Yavari, F.; Kritzinger, C.; Gaire, C.; Song, L.; Gulapalli, H.; Borca-Tasciuc, T.; Ajayan, P. M.; Koratkar, N., Tunable bandgap in graphene by the controlled adsorption of water molecules. *Small.* **2010,** *6*, 2535-2538.

144. Smith, A. D.; Elgammal, K.; Niklaus, F.; Delin, A.; Fischer, A. C.; Vaziri, S.; Forsberg, F.; Råsander, M.; Hugosson, H.; Bergqvist, L.; Schröder, S.; Kataria, S.; Östling, M.; Lemme, M. C., Resistive graphene humidity sensors with rapid and direct electrical readout. *Nanoscale.* **2015,** *7*, 19099-19109.

145. Duan, S.; Wang, B.; Lin, Y.; Li, Y.; Zhu, D.; Wu, J.; Xia, J.; Lei, W.; Wang, B., Waterproof mechanically robust multifunctional conformal sensors for underwater interactive human–machine interfaces. *Advanced Intelligent Systems.* **2021,** *3*, 2100056.

146. Wu, S.; Peng, S.; Han, Z. J.; Zhu, H.; Wang, C. H., Ultrasensitive and stretchable strain sensors based on mazelike vertical graphene network. *Acs Appl Mater Inter.* **2018,** *10*, 36312-36322.

147. Heck, I.; Lu, W.; Wang, Z.; Zhang, X.; Adak, T.; Cu, T.; Crumley, C.; Zhang, Y.; Wang, X. S., Soft, Wireless Pressure-Sensor-Integrated Smart Bandage for the Management of Diabetic Foot Ulcers. *Adv Mater Technol.* **2022,** *8*, 2200821.

148. Yao, W.; Yan, Y.; Sun, J.; Zhang, Z.; Sun, W.; Huang, W.; Cheng, J.; Zhao, H.; Xie, M.; Sun, Q.; Huang, G.; Lin, X., Mechanically Durable Superhydrophobic Strain Sensors with

High Biocompatibility and Sensing Performance for Underwater Motion Monitoring. *Acs Appl Mater Inter.* **2024**, *16,* 6548–6561.

149. Li, Q.; Liu, H.; Zhang, S.; Zhang, D.; Liu, X.; He, Y.; Mi, L.; Zhang, J.; Liu, C.; Shen, C.; Guo, Z., Superhydrophobic electrically conductive paper for ultrasensitive strain sensor with excellent anticorrosion and self-cleaning property. *Acs Appl Mater Inter.* **2019,** *11*, 21904-21914.

150. Liu, K.; Yang, C.; Zhang, S. Y.; Wang, Y.; Zou, R.; Alamusi; Deng, Q. B.; Hu, N., Laser direct writing of a multifunctional superhydrophobic composite strain sensor with excellent corrosion resistance and Anti-Icing/Deicing performance. *Materials & Design.* **2022,** *218*, 110689.

151. Jia, S.; Deng, S.; Qing, Y.; He, G.; Deng, X.; Luo, S.; Wu, Y.; Guo, J.; Carmalt, C. J.; Lu, Y.; Parkin, I. P., A coating-free superhydrophobic sensing material for full-range human motion and microliter droplet impact detection. *Chem Eng J.* **2021,** *410*, 128418.

152. Zhang, L.; He, J.; Liao, Y.; Zeng, X.; Qiu, N.; Liang, Y.; Xiao, P.; Chen, T., A self-protective, reproducible textile sensor with high performance towards human–machine interactions. *J Mater Chem A.* **2019,** *7*, 26631-26640.

153. Li, J.; Yao, Z.; Zhang, X.; Wang, Z.; Liu, L.; Yang, X.; Zhang, J.; Niu, S.; Han, Z.; Ren, L., Bionic multifunctional ultra-linear strain sensor, achieving underwater motion monitoring and weather condition monitoring. *Chem Eng J.* **2023,** *464*, 142539.

154. Li, L.; Bai, Y.; Li, L.; Wang, S.; Zhang, T., A superhydrophobic smart coating for flexible and wearable sensing electronics. *Adv Mater.* **2017,** *29*, 1702517.

155. Su, X.; Li, H.; Lai, X.; Chen, Z.; Zeng, X., Highly stretchable and conductive superhydrophobic coating for flexible electronics. *Acs Appl Mater Inter.* **2018,** *10*, 10587-10597.

156. Wang, L.; Chen, Y.; Lin, L.; Wang, H.; Huang, X.; Xue, H.; Gao, J., Highly stretchable, anti-corrosive and wearable strain sensors based on the PDMS/CNTs decorated elastomer nanofiber composite. *Chem Eng J.* **2019,** *362*, 89-98.

157. Lu, D.; Chu, Y.; Liao, S.; Li, W.; Cai, Y.; Wei, Q.; Wang, Q., Highly sensitive fabric strain sensor with double-layer conductive networks for joint rehabilitation therapy. *Composites Science and Technology.* **2022,** *230*, 109778.

158. Jeevahan, J.; Chandrasekaran, M.; Britto Joseph, G.; Durairaj, R.; Mageshwaran, G., Superhydrophobic surfaces: a review on fundamentals, applications, and challenges. *Journal of Coatings Technology and Research.* **2018,** *15*, 231-250.

159. Butt, H.-J.; Liu, J.; Koynov, K.; Straub, B.; Hinduja, C.; Roismann, I.; Berger, R.; Li, X.; Vollmer, D.; Steffen, W.; Kappl M., Contact angle hysteresis. *Current Opinion in Colloid & Interface Science.* **2022,** *59*, 101574.

160. Chieng, B. W.; Ibrahim, N. A.; Daud, N. A.; Talib, Z. A., Functionalization of graphene oxide via gamma-ray irradiation for hydrophobic materials. In *Synthesis, technology and applications of carbon nanomaterials*, Elsevier: 2019; pp 177-203.

161. Teisala, H.; Butt, H.-J. r., Hierarchical structures for superhydrophobic and superoleophobic surfaces. *Langmuir.* **2018,** *35*, 10689-10703.

162. Shirtcliffe, N. J.; McHale, G.; Atherton, S.; Newton, M. I., An introduction to superhydrophobicity. *Advances in colloid and interface science.* **2010,** *161*, 124-138.

163. Ding, Y.-R.; Xue, C.-H.; Guo, X.-J.; Wang, X.; Jia, S.-T.; An, Q.-F., Flexible superamphiphobic film with a 3D conductive network for wearable strain sensors in humid conditions. *ACS Applied Electronic Materials.* **2022,** *4*, 345-355.

164. Chen, Y.; Wang, L.; Wu, Z. F.; Luo, J. C.; Li, B.; Huang, X. W.; Xue, H. G.; Gao, J. F., Super-hydrophobic, durable and cost-effective carbon black/rubber composites for high performance strain sensors. *Compos Part B-Eng.* **2019,** *176*, 107358.

165. Gao, J. F.; Li, B.; Huang, X. W.; Wang, L.; Lin, L. W.; Wang, H.; Xue, H. G., Electrically conductive and fluorine free superhydrophobic strain sensors based on SiO_2/graphene-decorated electrospun nanofibers for human motion monitoring. *Chem Eng J.* **2019,** *373*, 298-306.

166. Niu, B.; Yang, S.; Hua, T.; Tian, X.; Koo, M., Facile fabrication of highly conductive, waterproof, and washable e-textiles for wearable applications. *Nano Research.* **2021,** *14*, 1043-1052.

167. Wang, P.; Sun, B.; Liang, Y.; Han, H.; Fan, X.; Wang, W.; Yang, Z., A stretchable and super-robust graphene superhydrophobic composite for electromechanical sensor application. *J Mater Chem A.* **2018,** *6*, 10404-10410.

168. Li, B.; Luo, J.; Huang, X.; Lin, L.; Wang, L.; Hu, M.; Tang, L.; Xue, H.; Gao, J.; Mai, Y.-W., A highly stretchable, super-hydrophobic strain sensor based on polydopamine and graphene reinforced nanofiber composite for human motion monitoring. *Composites Part B: Engineering.* **2020,** *181*, 107580.

169. Dai, Z.; Ding, S.; Lei, M.; Li, S.; Xu, Y.; Zhou, Y.; Zhou, B., A superhydrophobic and anti-corrosion strain sensor for robust underwater applications. *J Mater Chem A.* **2021,** *9*, 15282-15293.

170. Shi, H.; Shi, D.; Yin, L.; Yang, Z.; Luan, S.; Gao, J.; Zha, J.; Yin, J.; Li, R. K., Ultrasonication assisted preparation of carbonaceous nanoparticles modified polyurethane foam with good conductivity and high oil absorption properties. *Nanoscale.* **2014,** *6*, 13748-13753.

171. Gao, W.-C.; Wu, W.; Chen, C.-Z.; Zhao, H.; Liu, Y.; Li, Q.; Huang, C.-X.; Hu, G.-h.; Wang, S.-F.; Shi, D.; Zhang, Q.-C., Design of a superhydrophobic strain sensor with a multilayer structure for human motion monitoring. *Acs Appl Mater Inter.* **2021,** *14*, 1874-1884.

172. Liu, L.; Jiao, Z.; Zhang, J.; Wang, Y.; Zhang, C.; Meng, X.; Jiang, X.; Niu, S.; Han, Z.; Ren, L., Bioinspired, superhydrophobic, and paper-based strain sensors for wearable and underwater applications. *Acs Appl Mater Inter.* **2020,** *13*, 1967-1978.

173. Yang, L.; Ma, J.; Zhong, W.; Liu, Q.; Li, M.; Wang, W.; Wu, Y.; Wang, Y.; Liu, X.; Wang, D., Highly accurate fabric piezoresistive sensor with anti-interference from both high humidity and sweat based on hydrophobic non-fluoride titanium dioxide nanoparticles. *J Mater Chem C.* **2021,** *9*, 5217-5226.

174. Ni, Y.; Huang, J.; Li, S.; Dong, X.; Zhu, T.; Cai, W.; Chen, Z.; Lai, Y., Robust superhydrophobic rGO/PPy/PDMS coatings on a polyurethane sponge for underwater pressure and temperature sensing. *Acs Appl Mater Inter.* **2021,** *13*, 53271-53281.

175. Wu, J.; Li, H.; Lai, X.; Chen, Z.; Zeng, X., Conductive and superhydrophobic F-rGO@ CNTs/chitosan aerogel for piezoresistive pressure sensor. *Chem Eng J.* **2020,** *386*, 123998.

176. Xu, Z.; Zhang, D.; Li, Z.; Du, C.; Yang, Y.; Zhang, B.; Zhao, W., Waterproof flexible pressure sensors based on electrostatic self-assembled MXene/NH2-CNTs for motion monitoring and electronic skin. *Acs Appl Mater Inter.* **2023,** *15*, 32569-32579.

177. Liu, C.; Zhu, W.; Li, M.; Sun, X.; Guo, X.; Liu, J.; Liu, P.; Zhang, Y.; Huang, Y., Highly stable pressure sensor based on carbonized melamine sponge using fully wrapped conductive path for flexible electronic skin. *Organic Electronics.* **2020,** *76*, 105447.

178. Huang, Z. W.; Gurney, R. S.; Wang, T.; Liu, D., Environmentally durable superhydrophobic surfaces with robust photocatalytic self-cleaning and self-healing properties prepared via versatile film deposition methods. *J Colloid Interf Sci.* **2018,** *527*, 107-116.

179. Homayounfar, S. Z.; Kiaghadi, A.; Ganesan, D.; Andrew, T. L., Humidity-Resistant, Broad-Range Pressure Sensors for Garment-Integrated Health, Motion, and Grip Strength Monitoring in Natural Environments. *Adv Mater Technol.* **2023,** *8*, 2201313.

180. Li, S.; Chen, S.; Zhou, H.; Zhang, Q.; Lv, Y.; Sun, W.; Zhang, Q.; Guo, X., Achieving humidity-insensitive ammonia sensor based on Poly (3, 4-ethylene dioxythiophene): Poly (styrenesulfonate). *Organic Electronics.* **2018,** *62*, 234-240.

181. Dong, S.; Guo, D.; Wang, Q.; Yu, H.; Xu, Q.; Sung, H.-K.; Yao, Z.; Li, Y.; Li, Y., Fabrication of high-resolution, wide-range and low-crosstalk capacitive pressure sensing array for medical diagnosis. *Materials & Design.* **2023,** *235*, 112439.

182. Farahani, H.; Wagiran, R.; Hamidon, M. N., Humidity sensors principle, mechanism, and fabrication technologies: a comprehensive review. *Sensors.* **2014,** *14*, 7881-7939.

183. Wang, H. B.; Xiang, Z. H.; Zhao, P. C.; Wan, J.; Miao, L. M.; Guo, H.; Xu, C.; Zhao, W.; Han, M. D.; Zhang, H. X., Double-Sided Wearable Multifunctional Sensing System with Anti-interference Design for Human-Ambience Interface. *Acs Nano.* **2022,** *16*, 14679-14692.

184. Guo, H.; Chen, J.; Tian, L.; Leng, Q.; Xi, Y.; Hu, C., Airflow-induced triboelectric nanogenerator as a self-powered sensor for detecting humidity and airflow rate. *Acs Appl Mater Inter.* **2014,** *6*, 17184-17189.

185. Zheng, N.; Xue, J.; Jie, Y.; Cao, X.; Wang, Z. L., Wearable and humidity-resistant biomaterials-based triboelectric nanogenerator for high entropy energy harvesting and self-powered sensing. *Nano Research.* **2022,** *15*, 6213-6219.

186. Liu, D.; Liu, J.; Yang, M.; Cui, N.; Wang, H.; Gu, L.; Wang, L.; Qin, Y., Performance enhanced triboelectric nanogenerator by taking advantage of water in humid environments. *Nano Energy.* **2021,** *88*, 106303.

187. Wang, N.; Zheng, Y.; Feng, Y.; Zhou, F.; Wang, D., Biofilm material based triboelectric nanogenerator with high output performance in 95% humidity environment. *Nano Energy.* **2020,** *77*, 105088.

188. Sun, Y.; Zheng, Y.; Wang, R.; Lei, T.; Liu, J.; Fan, J.; Shou, W.; Liu, Y., 3D micro-nanostructure based waterproof triboelectric nanogenerator as an outdoor adventure power source. *Nano Energy.* **2022,** *100*, 107506.

189. Das, N. K.; Ravipati, M.; Badhulika, S., Nickel Metal-Organic Framework/PVDF Composite Nanofibers based Self-Powered Wireless Sensor for Pulse Monitoring of Underwater Divers via Triboelectrically Generated Maxwell-Displacement Current. *Adv Funct Mater.* **2023**, *33*, 2303288.

190. Chandrasekhar, A.; Vivekananthan, V.; Khandelwal, G.; Kim, S. J., A fully packed water-proof, humidity resistant triboelectric nanogenerator for transmitting Morse code. *Nano Energy.* **2019,** *60*, 850-856.

191. Rana, S. S.; Rahman, M. T.; Zahed, M. A.; Lee, S. H.; Do Shin, Y.; Seonu, S.; Kim, D.; Salauddin, M.; Bhatta, T.; Sharstha, K.; Park, J. Y., Zirconium metal-organic framework and hybridized Co-NPC@ MXene nanocomposite-coated fabric for stretchable, humidity-resistant triboelectric nanogenerators and self-powered tactile sensors. *Nano Energy.* **2022,** *104*, 107931.

192. Yan, S.; Lu, J.; Song, W.; Xiao, R., Flexible triboelectric nanogenerator based on cost-effective thermoplastic polymeric nanofiber membranes for body-motion energy harvesting with high humidity-resistance. *Nano Energy.* **2018,** *48*, 248-255.

193. Wen, R.; Guo, J.; Yu, A.; Zhai, J.; Wang, Z. l., Humidity-resistive triboelectric nanogenerator fabricated using metal organic framework composite. *Adv Funct Mater.* **2019,** *29*, 1807655.

194. Jao, Y.-T.; Yang, P.-K.; Chiu, C.-M.; Lin, Y.-J.; Chen, S.-W.; Choi, D.; Lin, Z.-H., A textile-based triboelectric nanogenerator with humidity-resistant output characteristic and its applications in self-powered healthcare sensors. *Nano Energy.* **2018,** *50*, 513-520.

195. He, J.; Zhou, R. H.; Zhang, Y. F.; Gao, W. C.; Chen, T.; Mai, W. J.; Pan, C. F., Strain-Insensitive Self-Powered Tactile Sensor Arrays Based on Intrinsically Stretchable and Patternable Ultrathin Conformal Wrinkled Graphene-Elastomer Composite. *Adv Funct Mater.* **2021,** *32*, 2107281.

196. Mousavi, S.; Howard, D.; Zhang, F.; Leng, J.; Wang, C. H., Direct 3D printing of highly anisotropic, flexible, constriction-resistive sensors for multidirectional proprioception in soft robots. *Acs Appl Mater Inter.* **2020,** *12*, 15631-15643.

197. Seong, M. H.; Hwang, I.; Lee, J.; Jeong, H. E., A Pressure-Insensitive Self-Attachable Flexible Strain Sensor with Bioinspired Adhesive and Active CNT Layers. *Sensors.* **2020,** *20*, 6965.

198. Xu, H.; Zheng, W.; Wang, Y.; Xu, D.; Zhao, N.; Qin, Y.; Yuan, Y.; Fan, Z.; Nan, X.; Duan, Q.; Wang, W.; Lu, Y.; Gao, L., Flexible tensile strain-pressure sensor with an off-axis deformation-insensitivity. *Nano Energy.* **2022,** *99*, 107384.

199. Zhang, H.; Chen, H.; Lee, J. H.; Kim, E.; Chan, K. Y.; Venkatesan, H.; Adegun, M. H.; Agbabiaka, O. G.; Shen, X.; Zheng, Q.; Yang, J; Kim, J.-K.,Bioinspired Chromotropic Ionic Skin with In-Plane Strain/Temperature/Pressure Multimodal Sensing and Ultrahigh Stimuli Discriminability. *Adv Funct Mater.* **2022,** *32*, 2208362.

200. Kim, S.; Amjadi, M.; Lee, T. I.; Jeong, Y.; Kwon, D.; Kim, M. S.; Kim, K.; Kim, T. S.; Oh, Y. S.; Park, I., Wearable, Ultrawide-Range, and Bending-Insensitive Pressure Sensor Based on Carbon Nanotube Network-Coated Porous Elastomer Sponges for Human Interface and Healthcare Devices. *Acs Appl Mater Inter.* **2019,** *11*, 23639-23648.

201. Feng, X. Y.; Hu, S. X.; Yu, J. J.; Guo, Z. P.; Wang, R.; Zhu, W.; Deng, Y., Synergistic creation of highly stable strain-insensitive pressure sensors by in-plane strain modulation and quasi-homogenous interfacial design. *J Mater Sci Technol.* **2023,** *159*, 72-80.

202. Liu, M. M.; Pu, X.; Jiang, C. Y.; Liu, T.; Huang, X.; Chen, L. B.; Du, C. H.; Sun, J. M.; Hu, W. G.; Wang, Z. L., Large-Area All-Textile Pressure Sensors for Monitoring Human Motion and Physiological Signals. *Adv Mater.* **2017,** *29*, 1703700.

203. Nayeem, M. O. G.; Lee, S.; Jin, H.; Matsuhisa, N.; Jinno, H.; Miyamoto, A.; Yokota, T.; Someya, T., All-nanofiber-based, ultrasensitive, gas-permeable mechanoacoustic sensors for continuous long-term heart monitoring. *P Natl Acad Sci USA.* **2020,** *117*, 7063-7070.

204. O'Neill, S. J. K.; Gong, H. X.; Matsuhisa, N.; Chen, S. C.; Moon, H.; Wu, H. C.; Chen, X. F.; Chen, X. D.; Bao, Z. N., A Carbon Flower Based Flexible Pressure Sensor Made from Large-Area Coating. *Adv Mater Interfaces.* **2020,** *7*, 2000875.

205. Gao, F. F.; Zhao, X.; Zhang, Z.; An, L. L.; Xu, L. X.; Xun, X. C.; Zhao, B.; Ouyang, T.; Zhang, Y.; Liao, Q. L.; Wang, L., A stretching-insensitive, self-powered and wearable pressure sensor. *Nano Energy.* **2022,** *91*, 106695.

206. Li, K.; Shuai, Y. M.; Cheng, X.; Luan, H. W.; Liu, S. Y.; Yang, C.; Xue, Z. G.; Huang, Y. G.; Zhang, Y. H., Island Effect in Stretchable Inorganic Electronics. *Small.* **2022,** *18*, 2107879.

207. Tolvanen, J.; Kilpijärvi, J.; Pitkänen, O.; Hannu, J.; Jantunen, H., Stretchable sensors with tunability and single stimuli-responsiveness through resistivity switching under compressive stress. *Acs Appl Mater Inter.* **2020,** *12*, 14433-14442.

208. Veeramuthu, L.; Cho, C.-J.; Liang, F.-C.; Venkatesan, M.; Kumar G, R.; Hsu, H.-Y.; Chung, R.-J.; Lee, C.-H.; Lee, W.-Y.; Kuo, C.-C., Human skin-inspired electrospun patterned robust strain-insensitive pressure sensors and wearable flexible light-emitting diodes. *Acs Appl Mater Inter.* **2022,** *14*, 30160-30173.

209. Zhou, S.; Li, Y. H.; Wang, Q. Q.; Lyu, Z., Integrated Actuation and Sensing: Toward Intelligent Soft Robots. *Cyborg Bionic Syst.* **2024,** *5*, 0105.

210. Yang, Y. P.; Wang, H. J.; Hou, Y. Y.; Nan, S. Q.; Di, Y. Y.; Dai, Y.; Li, F.; Zhang, J., MWCNTs/PDMS composite enabled printed flexible omnidirectional strain sensors for wearable electronics. *Composites Science and Technology.* **2022,** *226*, 109518.

211. Zhao, L.; Qiao, J. Y.; Li, F. M.; Yuan, D. D.; Huang, J. X.; Wang, M.; Xu, S. L., Laser-Patterned Hierarchical Aligned Micro-/Nanowire Network for Highly Sensitive Multidimensional Strain Sensor. *Acs Appl Mater Inter.* **2022,** *14*, 48276-48284.

212. Xu, F.; Jin, X. M.; Lan, C. T.; Gu, Z. H.; Zhou, R. H.; Sun, H.; Shao, Y. S.; Meng, J.; Liu, Y. P.; Pu, X., 3D arch-structured and machine-knitted triboelectric fabrics as self-powered strain sensors of smart textiles. *Nano Energy.* **2023,** *109*, 108312.

213. Wu, F.; Lan, B. X.; Cheng, Y.; Zhou, Y.; Hossain, G.; Grabher, G.; Shi, L. J.; Wang, R. R.; Sun, J., A stretchable and helically structured fiber nanogenerator for multifunctional electronic textiles. *Nano Energy.* **2022,** *101*, 107588.

214. Ning, C.; Cheng, R.; Jiang, Y.; Sheng, F.; Yi, J.; Shen, S.; Zhang, Y.; Peng, X.; Dong, K.; Wang, Z. L., Helical fiber strain sensors based on triboelectric nanogenerators for self-powered human respiratory monitoring. *Acs Nano.* **2022,** *16*, 2811-2821.

215. Nur, R.; Matsuhisa, N.; Jiang, Z.; Nayeem, M. O. G.; Yokota, T.; Someya, T., A highly sensitive capacitive-type strain sensor using wrinkled ultrathin gold films. *Nano Lett.* **2018,** *18*, 5610-5617.

216. Sun, F.; Liu, L.; Liu, T.; Wang, X.; Qi, Q.; Hang, Z.; Chen, K.; Xu, J.; Fu, J., Vascular smooth muscle-inspired architecture enables soft yet tough self-healing materials for durable capacitive strain-sensor. *Nat Commun.* **2023,** *14*, 130.

217. Wang, X.; Deng, Y.; Jiang, P.; Chen, X.; Yu, H., Low-hysteresis, pressure-insensitive, and transparent capacitive strain sensor for human activity monitoring. *Microsystems & Nanoengineering.* **2022,** *8*, 113.

218. Zhang, D.; Zhang, J.; Wu, Y.; Xiong, X.; Yang, J.; Dickey, M. D., Liquid metal interdigitated capacitive strain sensor with normal stress insensitivity. *Advanced Intelligent Systems.* **2022,** *4*, 2100201.

219. Goh, G. L.; Agarwala, S.; Yeong, W. Y., Directed and On-Demand Alignment of Carbon Nanotube: A Review toward 3D Printing of Electronics. *Adv Mater Interfaces.* **2019,** *6*, 1801318.

220. Zhang, M.; Fang, S. L.; Zakhidov, A. A.; Lee, S. B.; Aliev, A. E.; Williams, C. D.; Atkinson, K. R.; Baughman, R. H., Strong, transparent, multifunctional, carbon nanotube sheets. *Science.* **2005,** *309*, 1215-1219.

221. Tran, C. D.; Khoa, L. C.; Bui, T. T.; Dau, V. T., Dielectrophoresis can control the density of CNT membranes as confirmed by experiment and dissipative particle simulation. *Carbon.* **2019,** *155*, 279-286.

222. Ma, L. F.; Yang, W.; Wang, Y. S.; Chen, H.; Xing, Y. F.; Wang, J. C., Multi-dimensional strain sensor based on carbon nanotube film with aligned conductive networks. *Composites Science and Technology.* **2018,** *165*, 190-197.

223. Ma, L. F.; Lu, W. B., Carbon nanotube film based flexible bi-directional strain sensor for large deformation. *Mater Lett.* **2020,** *260*, 126959.

224. Chen, S.; Song, Y. J.; Ding, D. Y.; Ling, Z.; Xu, F., Flexible and Anisotropic Strain Sensor Based on Carbonized Crepe Paper with Aligned Cellulose Fibers. *Adv Funct Mater.* **2018,** *28*, 1802547.

225. Barlian, A. A.; Park, W. T.; Mallon, J. R.; Rastegar, A. J.; Pruitt, B. L., Review: Semiconductor Piezoresistance for Microsystems. *P Ieee.* **2009,** *97*, 513-552.

226. Phan, H. P.; Dao, D. V.; Tanner, P.; Wang, L.; Nguyen, N. T.; Zhu, Y.; Dimitrijev, S., Fundamental piezoresistive coefficients of p-type single crystalline 3C-SiC. *Appl Phys Lett.* **2014,** *104*, 111905.

227. Shor, J. S.; Goldstein, D.; Kurtz, A. D., Characterization of n-type beta-SiC as a piezoresistor. *IEEE transactions on electron devices.* **1993,** *40*, 1093-1099.

228. Choi, G.; Jang, H.; Oh, S.; Cho, H.; Yoo, H.; Kang, H. I.; Choi, Y.; Kim, S. H.; Lee, H. S., A highly sensitive and stress-direction-recognizing asterisk-shaped carbon nanotube strain sensor. *J Mater Chem C.* **2019,** *7*, 9504-9512.

229. Jang, H.; Baek, S.; Choi, G.; Oh, S.; Lim, H. S.; Jang, Y.; Lee, H. S., Crisscross-designed piezoresistive strain sensors with a cracked microtectonic architecture for direction-selective tensile perception. *J Mater Chem C.* **2018,** *6*, 11170-11177.

230. Ha, S. H.; Ha, S. H.; Jeon, M. B.; Cho, J. H.; Kim, J. M., Highly sensitive and selective multidimensional resistive strain sensors based on a stiffness-variant stretchable substrate. *Nanoscale.* **2018,** *10*, 5105-5113.

231. Lee, J. H.; Kim, S. H.; Heo, J. S.; Kwak, J. Y.; Park, C. W.; Kim, I.; Lee, M.; Park, H. H.; Kim, Y. H.; Lee, S. J.; Park, S. K., Heterogeneous Structure Omnidirectional Strain Sensor Arrays With Cognitively Learned Neural Networks. *Adv Mater.* **2023,** *35*, 2208184.

232. Oh, J.; Yang, J. C.; Kim, J. O.; Park, H.; Kwon, S. Y.; Lee, S.; Sim, J. Y.; Oh, H. W.; Kim, J.; Park, S., Pressure Insensitive Strain Sensor with Facile Solution-Based Process for Tactile Sensing Applications. *Acs Nano.* **2018,** *12*, 7546-7553.

233. Pang, Y.; Tian, H.; Tao, L. Q.; Li, Y. X.; Wang, X. F.; Deng, N. Q.; Yang, Y.; Ren, T. L., Flexible, Highly Sensitive, and Wearable Pressure and Strain Sensors with Graphene Porous Network Structure. *Acs Appl Mater Inter.* **2016,** *8*, 26458-26462.

234. Ge, J.; Sun, L.; Zhang, F. R.; Zhang, Y.; Shi, L. A.; Zhao, H. Y.; Zhu, H. W.; Jiang, H. L.; Yu, S. H., A stretchable electronic fabric artificial skin with pressure-, lateral strain-, and flexion-sensitive properties. *Adv Mater.* **2016,** *28*, 722-728.

235. Wang, Z. H.; Zhang, L.; Liu, J.; Li, C. Z., Highly Stretchable, Sensitive, and Transparent Strain Sensors with a Controllable In-Plane Mesh Structure. *Acs Appl Mater Inter.* **2019,** *11*, 5316-5324.

236. Kim, T.; Hong, I. S.; Roh, Y.; Kim, D.; Kim, S.; Im, S.; Kim, C.; Jang, K.; Kim, S.; Kim, M.; Park, J.; Gong, D. H. Y.; Ahn, K.; Lee, J. G.; Lee, G. H.; Lee, H. S.; Kang, J. H.; Hong, J. M.; Lee, S. C.; Seo, S., et al., Spider-inspired tunable mechanosensor for biomedical applications. *Npj Flex Electron.* **2023,** *7*, 12.

237. Widlund, T.; Yang, S. X.; Hsu, Y. Y.; Lu, N. S., Stretchability and compliance of freestanding serpentine-shaped ribbons. *Int J Solids Struct.* **2014,** *51*, 4026-4037.

238. Kwon, S.; Kim, H. S.; Kwon, K.; Kim, H.; Kim, Y. S.; Lee, S. H.; Kwon, Y. T.; Jeong, J. W.; Trotti, L. M.; Duarte, A.; Yeo, W. H., At-home wireless sleep monitoring patches for the clinical assessment of sleep quality and sleep apnea. *Sci Adv.* **2023,** *9*, eadg9671.

239. Yin, J.; Wang, S.; Tat, T.; Chen, J., Motion artefact management for soft bioelectronics. *Nature Reviews Bioengineering.* **2024**, *2,* 541-558.

240. Li, Y.; Feng, J. Y.; Wang, L. L.; Li, T. Y.; Pang, Y. C.; Liu, B. G.; Liu, S. J.; Zhao, Q., Strain-insensitive bioelectronics. *Chem Eng J.* **2024,** *482*, 148758.

241. Wu, H.; Yang, G. G.; Zhu, K. H.; Liu, S. Y.; Guo, W.; Jiang, Z.; Li, Z., Materials, Devices, and Systems of On-Skin Electrodes for Electrophysiological Monitoring and Human-Machine Interfaces. *Adv Sci.* **2020,** *8*, 2001938.

242. Park, E. S., Resistivity and thermal reproducibility of the carbon black and SnO_2/Sb coated titanium dioxide filled silicone rubber heaters. *Macromol Mater Eng.* **2005,** *290*, 1213-1219.

243. Sau, K. P.; Chaki, T. K.; Khastgir, D., Carbon fibre filled conductive composites based on nitrile rubber (NBR), ethylene propylene diene rubber (EPDM) and their blend. *Polymer.* **1998,** *39*, 6461-6471.

244. Wu, F. Y.; Cheng, H. M., Structure and thermal expansion of multi-walled carbon nanotubes before and after high temperature treatment. *J Phys D Appl Phys.* **2005,** *38*, 4302-4307.

245. Filatov, O.; Soldatenko, O., Size dependence of thermal expansion of silver nanowires. *Appl Nanosci.* **2020,** *10*, 4827-4830.

246. Zhao, L.; Tang, J.; Zhou, M.; Shen, K., A review of the coefficient of thermal expansion and thermal conductivity of graphite. *New Carbon Mater.* **2022,** *37*, 544-555.

247. Huh, S. H.; Choi, S. H.; Ju, H. M.; Kim, D. H., Properties of interlayer thermal expansion of 6-layered reduced graphene oxide. *J Korean Phys Soc.* **2014,** *64*, 615-618.

248. Yoon, D.; Son, Y. W.; Cheong, H., Negative Thermal Expansion Coefficient of Graphene Measured by Raman Spectroscopy. *Nano Lett.* **2011,** *11*, 3227-3231.

249. Music, D.; Elalfy, L., Tuneable thermal expansion of poly (3,4-ethylenedioxythiophene) polystyrene sulfonate. *J Phys-Condens Mat.* **2019,** *31*, 125101.

250. Pishvar, M.; Amirkhosravi, M.; Manas-Zloczower, I., Thermomechanical Performance of Thermoplastic Polyurethane–Poly (tetrafluoroethylene) Fibril Nanocomposites. *ACS Applied Polymer Materials.* **2023,** *5*, 5342-5348.

251. Gu, J.; Kwon, D.; Ahn, J.; Park, I., Wearable Strain Sensors Using Light Transmittance Change of Carbon Nanotube-Embedded Elastomers with Microcracks. *Acs Appl Mater Inter.* **2020,** *12*, 10908-10917.

252. Gunes, I. S.; Cao, F.; Jana, S. C., Effect of thermal expansion on shape memory behavior of polyurethane and its nanocomposites. *Journal of Polymer Science Part B: Polymer Physics.* **2008,** *46*, 1437-1449.

253. Uday, M. B.; Ahmad-Fauzi, M. N.; Alias Mohd, N.; Srithar, R. Current Issues and Problems in the Joining of Ceramic to Metal. In *Joining Technologies*, Mahadzir, I., Ed.; IntechOpen, 2016; p Ch. 8.

254. Qiao, H.; Sun, S.; Wu, P., Non-equilibrium-Growing Aesthetic Ionic Skin for Fingertip-Like Strain-Undisturbed Tactile Sensation and Texture Recognition. *Adv Mater.* **2023**, 35, 2300593.

Table 1. Comparison of near-zero TCR and corresponding temperature range for materials used in temperature-insensitive pressure and strain sensors.

Sensor type	Materials	Temperature	TCR (K^{-1} or $°C^{-1}$)
Pressure sensors	CNT-PDMS (-) / CB-PDMS (+)	T = 30 – 200 °C	$\Delta R < 2\%$ [25]
	PPy (-) / Ag NWs(+) (83.3 wt%)	T = 17 – 50 °C	-0.86×10^{-3} [49]
	MWCNTs (-) / CSA-doped PANI (+) (1:45)	ΔT = -40 K to 40 K	No Data [91]
	MWCNTs (-) / GPs (+) (1:30) / NR	T = 30 to 65 °C	No Data [84]
	rGO (-) / Ag Nws (+) (40:1)	T = 25 to 60 °C	-3.24×10^{-4} [66]
	PEDOT:PSS / DMSO (Exposed 10 min)	T = 20 to 45 °Cs	No Data [54]
	PEDOT:PSS / DMSO (5 vol%)	T = up to 100 °C	No Data [50, 73]
	PEDOT:PSS / EG (5 vol%)	ΔT = 1 to 30 K	No Data [99]
	PPy / Phytic acid	T = -10 to 100 °C	No Data [75]
	Graphene / Pyramid PDMS	T = 25 to 60 °C [85]	Order of 10^{-3} or 10^{-4} [95, 96]
	Graphene / Porous structure	ΔT = up to 30 K [97, 98]	
	PET/MXene/PDMS	T = 25 and 50 °C	2.1 x 10^{-5} [94]
Strain sensors	Graphene (-) / Gold (Palladium) (+)	T = 30 to 65 °C	-2×10^{-3} to 10^{-3} [78]
	RuO_2 paste – Al_2O_3	T = 25 to 125 °C	$\sim -2 \times 10^{-5}$ [86]
	SWCNT (-) / GNP (+) – PET (0.0033)	T = 30 to 85 °C	$\Delta R < 0.6\%$ [52]
	P3HT/BCF (-) / AgNPs (+) / PI/Parylene	T = -12 to 50 °C	1.1×10^{-3} [87]
	Graphene (-) / Ag Nws (+) / PDMS	T = -40 to 20 °C	-0.7×10^{-4} [65]
	CNTs (-) / AgNPs (+) / DS	T = -40 to 20 °C	1.16×10^{-5} [92]
	GNP (+) – SiCNO or polysilanzane	T = 30 to 200 °C	$\sim 10^{-6}$ [53]
	TiB_2 (+) / SiCN – Al_2O_3/SiCN	T = 300 to 700 °C	1.16×10^{-6} [93]
	Au/ITO (+) / PDMS/PET	T = 25 to 45 °C	-0.8×10^{-6} [60]
	(2 or 3%) CNTs (-) / Epoxy resin	T = -40 °C to 100 °C	No Data [72]
	PEDOT:PSS / DMSO (3 vol%)	T = 293 to 373 K	-3.24×10^{-5} [74]

Table 2. CTE of conductive fillers and substrates used in literature.

	Materials	CTE	Ref
Conductive fillers	CB	1.19×10^{-6} K^{-1}	242
	Carbon fibers	-1.45×10^{-6} K^{-1}	243
	SWCNTs	$-1\ to\ 4 \times 10^{-6}$ K^{-1}	114
	MWCNTs	$\sim 20 \times 10^{-6}$ K^{-1}	113, 244
	Ag NWs	~ 6 to 22×10^{-6} K^{-1}	245
	Graphite	-1.5 to 2×10^{-6} K^{-1} (in-plane) (+) < 40×10^{-6} K^{-1} (out-of-plane)	246
	rGO	(+) < 35×10^{-6} K^{-1}	247
	Graphene	-8×10^{-6} K^{-1}	248
	PEDOT:PSS	16 to 62×10^{-6} K^{-1}	249
Substrates	Rubber	$190\ to\ 220 \times 10^{-6}$ K^{-1}	243
	PDMS	$\sim 300 \times 10^{-6}$ K^{-1}	115
	TPU	$\sim 350 \times 10^{-6}$ K^{-1}	250
	Ecoflex (0030)	284.2×10^{-6} $°C^{-1}$	251
	PU	70 to 160×10^{-6} K^{-1}	252
	Epoxy resin	35 to 55×10^{-6} K^{-1}	72
	PI	30 to 60×10^{-6} K^{-1}	89
	PET	75×10^{-6} K^{-1}	88
	Ceramics (such as Al_2O_3 or TiO_2)	(+) < 20×10^{-6} K^{-1}	253

Table 3. Summary of pressure sensors insensitive to ambient conditions (temperature and liquid/humidity) and off-axis deformation (bending and strain).

Ref	Type	Materials/Design	Sensitivity	Range	Insensitive to	Mechanism
66	Piezoresistive	Ridge-like microstructure coated by Ag NWs/rGO	1.58 kPa^{-1}	0-400 Pa	Temperature 25 - 60 °C	Opposite TCR
84	Piezoresistive	Mixed MWCNTs/GPs in rubber	6.975 kPa^{-1}	< 25 kPa	Temperature 25 - 65 °C	Opposite TCR
			2.509 kPa^{-1}	25-50 kPa		
49	Piezoresistive	Ppy-coated Ag NWs aero-sponge	0.33 kPa^{-1}	< 2 kPa	Temperature 17 - 50 °C	Opposite TCR
73	Piezoresistive	PEDOT:PSS/DMSO	134.25 kPa^{-1}	< 50 kPa	Temperature	Alternating electrical properties
			37.65 kPa^{-1}	< 300 kPa		
100	Piezoresistive	Wood sponge /PEDOT:PSS/GOPS/DMSO	67.2 kPa^{-1}	0-1 kPa	Temperature ΔT = 23.5 °C	Alternating electrical properties
85	Piezoresistive	Microstructure PDMS coated Graphene / interdigital electrodes	10^6 Ohm kPa^{-1}	3 Pa - 140 kPa	Temperature 25 - 60 °C Humidity 30 - 90 %	Small TCR of graphene
97	Piezoresistive	Graphene-coated TPU/CNFs	0.14 kPa^{-1}	0-60 kPa	Temperature ΔT = 20 K	Small TCR of graphene
			0.51 kPa^{-1}	60-120 kPa		
109	Capacitive	SWCNT-embedded microstructured PDMS/Al2O3/(Ni/Ti)	0.7 kPa^{-1}	25 kPa	Temperature 22 - 70 °C	Temperature-independent dielectric layer.
133	Triboelectric	Microstructured PDMS – PET.	1.394 V kPa^{-1} 0.379 V kPa^{-1}	1 Pa – 2 kPa 2-100 kPa	Temperature ΔT = 30 K	No information
127	Triboelectric	Microstructure PDMS (Single mode)	5.07 mV/ Pa 1.89 mV/Pa	200-1720 Pa (720 – 3650 Pa	Temperature 25 - 80 °C	Much higher internal resistance
35	Piezoresistive	H_3PO_4-PVA Cu/Ni/Al	1.0/N	0.1 – 0.4 N	Normal saline	Encapsulation

		(Ecoflex)			Artificial blood	
173	Piezoresistive	Cotton fabric/ PEDOT:PSS/TiO_2-ODI	0.83 kPa^{-1}	50 kPa	Humidity 50% - 95% Different droplets	Superhydrophobic porous materials
152	Piezoresistive	PET textile/CNT/PPy-PDA-PFDS	147.4 kPa^{-1} 101.k kPa^{-1}	0 – 20 kPa 20 – 50 kPa	Sweat 1M saline	Superhydrophobic porous materials
37	Piezoresistive	Cellulose/Ag Nws/PEDOT:PSS	23.35 kPa^{-1}	0 – 400 Pa	Humidity 50% – 90%	Chemical bonds
107	Capacitance	PEDOT:PSS/PVA/Co_3O_4 interdigital electrode IL/TPU nanofiber electrolyte	147.19 kPa^{-1} 4.41 kPa^{-1}	0-7 kPa 25 - 85 kPa	Humidity 30% - 90 %	Encapsulation
191	Triboelectric	Ecoflex@MOF525/Ecoflex@Co-NPC@Mxene (single mode)	149 V/ kPa 9 V/kPa	14 kPa 14-60 kPa	Humidity Water	Encapsulation
193	Triboelectric	Cu – PDMS/HKUST-1	No information	No information	Humidity 10% – 95%	Material selection
194	Triboelectric	Chitosan-glycerol PTFE	No information	No information	Humidity 20% - 80%	Material selection
57	Piezoresistive	CNT/Graphene/Fluorinated copolymer	~ 2.86 kPa^{-1}	0 - 350 Pa	Bending (80 um)	Ultrathin
204	Piezoresistive	Carbon flowers embedded in SBS	$2x10^5$ kPa^{-1} $5.8x10^4$ kPa^{-1}	0-10 kPa 10-40 kPa	Bending (5.5 mm)	Ultrathin
200	Piezoresistive	CNT/sponge PDMS	0.02 kPa^{-1} 0.01 kPa^{-1}	0-100 kPa 100 kPa - 1.2 MPa	Bending (7.5 mm)	Porous structure
105	Capacitive	Porous pyramid PDMS	44.5 kPa^{-1}	100 Pa	Strain (60%)	Large island
58	Triboelectric	PDMS-Mxene-IPN (UV)	0.514 N-1	0-2 N	Strain (120%)	Large island

201	Piezoresistive	Microstructure CNT/PDMS - microstructure Ti/Ag electrodes	0.0339 kPa^{-1} 0.0098 kPa^{-1}	< 5kPa < 40 kPa	Strain (20%)	- Large island - Stretchable electrodes - Quasi-homogenous interlink
39	Capacitive (EDL))	Stiff supporting pyramid microstructure	4.2 kPA^{-1} 2.0 kPa^{-1}	0-1 kPa 1-10 kPa	Strain (50%)	Small island
199	Triboelectric	Ionic hydrogel / wrinkle PDMS / CNT/PDMS	528 V kPa^{-1} 63.7 V kPa^{-1}	0-2 kPa 2-9 kPa	Strain (80%)	Small ridges
254	Triboelectric	Fluoroelastomer-coated hydrogel	1.5 V kPa^{-1}	32.5 kPa	Strain (70%)	Small ridge
208	Piezoresistive	- Pre-strained patterned Ag/PDMS electrodes - SBS dielectric layer	83.46 kPa^{-1}	~ 70 -110 Pa	Strain (20%)	- No island - Stretchable electrodes - Stretchable SBS layer

Table 4. Summary of piezoresistive strain sensors insensitive to ambient conditions (temperature and liquid/humidity) and off-axis deformation (pressure, torsion, bending, and in-plane strain).

Ref	Materials/design	Sensitivity (GF)	Strain range	Insensitive to	Mechanism
52	SWCNT/GNP/PET	~ 5	0.2 %	Temperature 30 °C to 80 °C (Dynamic response)	Opposite TCR
87	Parylene/P3HT/BCF/ AgNPs/PI	64	7%	Temperature -12 °C to 50 °C	Opposite TCR
72	CNTs/Epoxy resin	11.2	1%	Temperature -40 °C to 100 °C	Conductive material and supporting matrix
60	Au/ITO/PDMS/PET	7039 17785	< 0.4% > 0.4% (2% work)	Temperature 25 °C to 45 °C	Conductive material and supporting matrix
53	GNP/polysilazane (paper substrate)	191 335 2362	0.5%	Temperature 30 °C to 200 °C (Static and dynamic response)	Conductive material and supporting matrix
47	rGO/Calotropis gigantea yarn/ Elastic yarn	~ 3	50%	Temperature 22.8 °C to 47.3 °C (Dynamic response)	Altering electrical properties
74	PEDOT:PSS/DMSO	3.3	5%	Temperature 293 K to 373 K	Altering electrical properties
51	Wrinkled VBH/rGO/PDMS	1.84 22.26 116.01 1199.1	400%	Different droplets (Dynamic response)	Single microstructure (Coating in order)
48	TPE/MWCNTs/PDMS	3.76 13.57 69.48	80%	Immersed in liquids (Initial resistance) Different droplets (Dynamic response)	Single microstructure (Coating in order)
154	MWCNTs/TPE	15.6 8.3 5.5	80%	Water droplet (Dynamic response)	Single microstructure (Post-treatment)
148	CBNPs/PDMS	101.75	0.015−460%	Water impact (Initial resistance)	Single microstructure (Post-treatment)

151	Rubbed MWCNTs/vulcanized silicone rubber	2.1 to 214	450%	Water pouring High humidity (91%) (Initial resistance) (Dynamic response)	Hierarchical surface
55	Wrinkled PDMS/APTES/MWCNT/G/Ag/FAS	42 210 1989	170%	Different droplets (Dynamic response) (Gauge factor)	Hierarchical surface
138	PET fabric/rGO/PDMS micro-nano particles	2.5	40%	Underwater (Static response)	Superhydrophobic fibers
56	TPU fibers/PDA/CNC/G/Hf-SiO_2	up to 23600	98%	Underwater (Dynamic response)	Superhydrophobic fibers
232	Porous MWCNTs/PDMS	~ 56	70%	Pressure (140 kPa) (Initial resistance)	Fillers well embedded within the matrix
59	Cu deposited yarns	49.5	100%	Pressure (100 kPa) Bending (Initial resistance)	Insulating supports
198	Ecoflex/Ag Microsphere/HCC/Au-foil	1.23 8.67 1.75	150%	Pressure (60 kPa) Bending (8 mm) Torsion (180°)	Serpentine structure
33	TPU hybrid gel	4.26	400%	Pressure (30 kPa) Torsion Bending (180°)	Meander structure
44	Pre-strained TPU/Silicone adhesive/CBF-epoxy/Silicone adhesive/Pre-strained TPU	9400	< 5%	Pressure (car, hammer, > 500 kPa) Torsion (30°) Bending (80°)	Stiff sensing material with low piezoresistive response Contacted mender structure
222	Aligned CNTs/PDMS	36.2 and 1198 (parallel) Up to 3.28 (perpendicular)	250% 400%	Other in-plane direction (Perpendicular to the alignment direction)	Intrinsic anisotropic properties
43	Aligned CNF/PDMS	Up to 180 (parallel) 0.3 (perpendicular)	30%	Other in-plane direction (Perpendicular to the alignment direction)	Intrinsic anisotropic properties

196	TPU/PLA-CNT/TPU	1342 (working direction) 0.9 (perpendicular)	2%	Other in-plane direction	Contacted meander structure
211	PET/Ag-Cr/PDMS	65.53 (parallel to length) 7.32 (perpendicular)	2.5%	Other in-plane direction	Micro/nano meter width
224	Crepe cellulose paper/PDMS	3.69 (working direction) 0.14 (perpendicular)	5%	Other in-plane direction	Wrinkled surface structure
231	CNT/CB/PDMS	8 (working direction)	35%	Other in-plane direction	Mechanical mismatch – Rigid electrodes

For Table of Contents Only

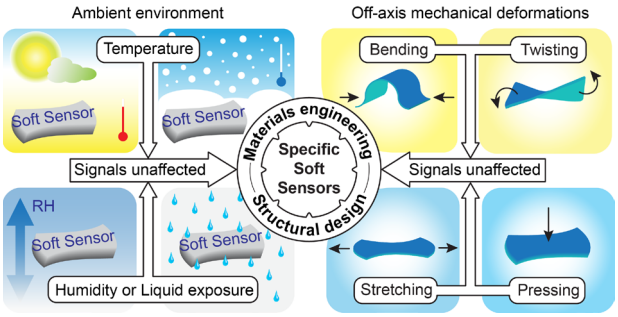

We would like to confirm that the TOC was created entirely by one author, Duy Van Nguyen.